NATIONAL ENERGY TECHNOLOGY LABORATORY
OIL & GAS

DOE Award No.: DE-FE-0028967

Final Scientific/Technical Report

Project Period (10/1/2016-9/30/2019)

A multi-scale experimental investigation of flow properties in coarse-grained hydrate reservoirs during production

Submitted by:
Peter B. Flemings

DocuSigned by:
Peter B. Flemings
36634B8D9FFC496...
Signature

The University of Texas at Austin
DUNS #: 170230239
101 East 27th Street, Suite 4.300
Austin, TX 78712-1500
Email: pflemings@jsg.utexas.edu
Phone number: (512) 475-8738

Prepared for:
United States Department of Energy
National Energy Technology Laboratory

December 17, 2019

U.S. DEPARTMENT OF ENERGY | NATIONAL ENERGY TECHNOLOGY LABORATORY

Office of Fossil Energy

DISCLAIMER

Abstract

In this project, “A multi-scale experimental investigation of flow properties in coarse-grained hydrate reservoirs during production” we explored the relative permeability and dissipation behavior of hydrate-bearing coarse-grained sediment at the core scale and we observed the formation and dissociation of these materials at the pore scale with micro-CT and Raman experiments. The 3-year project results inform reservoir simulation efforts, critical to determining the viability of the coarse-grained hydrate reservoir as an energy resource.

We performed the first 3 phase relative permeability experiments in a hydrate-bearing medium using the steady state method (gas and water flow in the presence of hydrate). Results support a model where water is the most wetting phase, hydrate is the intermediate wetting phase, and gas is the least wetting phase. This model can be used to predict relative permeability of gas and water in the presence of hydrate.

We showed that when hydrate dissociates, it does so at a pressure and temperature predicted for fresh water (no salinity) conditions. At the scale of a grid block, reservoir simulation models should assume that hydrate dissociates at the freshwater phase boundary.

We observed that the chemistry and the pore habit of methane hydrates change dramatically over the timescales of experiments (hours to weeks). It takes weeks to months for hydrates to evolve from a non-stoichiometric to stoichiometric compound with 3:1 large cage vs small cage occupancy. We documented hydrates forming initially in small clayey silt surfaces but gradually concentrated in large pores in sand-sized sediment.

Table of Contents

Table of Figures

Table of Tables

Executive Summary and Project Impact

The goal of this project was to develop a systematic understanding of both relative permeability and hydrate dissociation in hydrate-bearing coarse-grained porous media. We wanted to first measure these core-scale flow properties and then observe hydrate habit at the pore scale using micro-CT and micro-Raman to understand the flow behavior.

At the core scale, we built apparatuses to measure relative permeability and hydrate formation and dissociation. At the pore scale, we developed equipment and methods to 1) observe the habit of the hydrate, gas, and water phases within the pore space at a range of initial saturations with micro-CT; and 2) imaged phases and molecules/salinity present both at initial saturations and at stages of dissociation with optical micro-Raman spectroscopy.

We performed our initial experiments by manufacturing hydrate in sediments provided by industrial vendors. We achieved hydrate saturations of 10-60%; however, it was difficult to obtain repeatable hydrate saturations. After developing our techniques on synthetic sediments, we moved to experiments on sediments as similar as possible to those acquired by the University of Texas hydrate pressure coring expedition (UT-GOM2-1) in the Gulf of Mexico Green Canyon 955 (GC 955). We either ran experiments with intact and depressurized sediment from GC 955 or we used industrially processed sediments that were as similar as possible in grain size.

Our key results are as follows.

1) Relative permeability is used to describe how gas & water flow in the presence of hydrate. It is a primary control on how efficiently gas moves to the wellbore and the fraction of gas vs. water that is produced. We measured two-phase permeability of brine or gas in the presence of hydrate and demonstrated that the relative permeability of brine in the presence of hydrate (no gas) behaves just like the relative permeability of brine in the presence of gas (no hydrate). We also measured relative permeability of natural hydrate-bearing samples from GC 955 and compared results to the relative permeability of water at different hydrate saturations in Berea cores. We found similar behavior.
   We also made the first ever measurements of three-phase permeability in a hydrate-bearing medium using the steady state method (gas and water flow in the presence of hydrate). Our results support a model where water is the most wetting phase, hydrate is the intermediate wetting phase, and gas is the least wetting phase. This model can be used to predict relative permeability of gas and water in the presence of hydrate (See Section 1.0 Macro-Scale: Relative Permeability of Methane Hydrate Sand Packs and Appendix A Revise Milestone Report 2A.) This relative permeability model will provide a rigorous foundation for reservoir simulation to more accurately forecast water and gas production.

2) Depressurization (production) behavior: We demonstrated that the in situ pore water salinity can be determined from the pressure and temperature observed at the onset of dissociation. We also showed that as dissociation proceeds, it does so at a pressure and temperature predicted for fresh water (no salinity) conditions. This occurs even though the average salinity of

the system is much higher than fresh water. We interpret that when hydrate dissociates, fresh water surrounds the dissociating hydrate, resulting in locally fresh water conditions. We suggest that at the scale of a grid block, reservoir simulation models should assume that hydrate dissociates at the freshwater phase boundary. (See Section 2.0 Macro-Scale: Depressurization of Methane Hydrate Sand Packs, and Appendix C Milestone Report 2C.). We also observed simultaneous dissociation of hydrate in some pores and reformation of hydrate in nearby pores. Thus, local temperature and salinity vary significantly at the pore scale during dissociation.

3) Pore Habit and Evolution: With Micro-Raman and micro-CT, we observed that the chemistry and the pore habit of methane hydrates change dramatically over the timescales of experiments (hours to weeks). The micro-CT Chamber revealed highly heterogeneous hydrate saturation and porous hydrate that varied from “grain-attaching” (at low saturation) to “pore-filling and interconnected” at high saturation. At high hydrate saturations, hydrate dissociation starting at the periphery of hydrate clumps and proceeded inward. In Micro-Raman experiments where two grain sizes were placed adjacent to each other, we observed that hydrate nucleated in the smaller grain size material, but evolved to higher concentrations within the coarse-grained material. Specifically hydrate preferentially forming in finer grain sediments with a non-stoichiometric ration of sI to sII hydrate but migrating to courser grains and eventually reaching stoichiometric equilibrium (See Section 3.0 Micro-Scale: CT Observation of Methane Hydrate Sand Packs and Appendix D Revised Milestone Report 2D and Section 4.0 Micro-Scale: Raman Observation of Methane-Gas-Water Systems.) (Section 4.0 Micro-Scale: Raman Observation of Methane-Gas-Water Systems.)

Introduction

The project “A multi-scale experimental investigation of flow properties in coarse-grained hydrate reservoirs during production” was funded from the Department of Energy from October 1, 2016 through September 30, 2019. This report provides a summary of the project background, methods, results, and conclusions.

Project Schedule and Structure

Phase 1, Synthetics (Oct 1, 2016 – March 31, 2018):

- Build essential equipment
- Generate synthetic hydrates in porous media in a consistent and geologically realistic way
- Begin characterization at micro- and macro-scale
- Perturb and study behavior

Phase 2, Natural (April 1, 2018 – Sept 30, 2019):

- Analyze recovered pressure cores as possible

- Characterize synthetic and natural samples at micro- and macro-scale
- Perturb and study behavior

Milestones

All milestones and revised milestones were met. The Milestones are listed in Table 1.

Table 1. Milestones

Milestone Description	Planned Completion	Actual Completion	Verification Method	Comments
Milestone 1.A: Project Kick-off Meeting	11/22/16 (Y1Q1)	11/22/16	Presentation	Complete
Milestone 1.B: Achieve hydrate formation in sand-pack (Subtask 2.1)	6/27/17 (Y1Q3)	8/11/17	Documentation of milestone achievement (Deliverable 2.1)	Complete, See Attachment A. Milestone 1.B Report in the Phase 1 Report at https://netl.doe.gov/files/oil-gas/fe0028967-Phase-1-Technical-Report.pdf
Milestone 1.C: Controlled and measured hydrate saturation using different methods (Subtask 2.2)	3/27/18 (Y2Q2)	3/27/18	Documentation of milestone achievement (Deliverable 2.1)	Complete, See Attachment B. Milestone 1.C Report in the Phase 1 Report at https://netl.doe.gov/files/oil-gas/fe0028967-Phase-1-Technical-Report.pdf
3 Milestone 1.D: Achieved depressurization and demonstrated mass balance (Subtask 3.1)	3/27/18 (Y2Q2)	12/18/17	Documentation of milestone achievement (Deliverable 3.1)	Complete, See Attachment C. Milestone 1.D Report in the Phase 1 Report at https://netl.doe.gov/files/oil-gas/fe0028967-Phase-1-Technical-Report.pdf
Milestone 1.E: Built and tested micro-consolidation device (Subtask 4.1)	6/27/17 (Y1Q3)	6/27/17	Documentation of milestone achievement (Deliverable 4.1)	Complete, See Attachment D. Milestone 1.E Report in the Phase 1 Report at https://netl.doe.gov/files/oil-gas/fe0028967-Phase-1-Technical-Report.pdf

Milestone 1.F: Achieved Hydrate formation and measurements in Micro-CT consolidation device (Subtask 4.2)	3/27/18 (Y2Q2)	2/15/18	Documentation of milestone achievement (Deliverable 4.1)	Complete, See Attachment E. Milestone 1.F Report in the Phase 1 Report at https://netl.doe.gov/files/oil-gas/fe0028967-Phase-1-Technical-Report.pdf
Milestone 1.G: Built and integrated high-pressure gas mixing chamber (Subtask 5.1)	3/27/18 (Y2Q2)	6/27/17	Documentation of milestone achievement (Deliverable 5.1)	Complete, See Attachment F. Milestone 1.G Report in the Phase 1 Report at https://netl.doe.gov/files/oil-gas/fe0028967-Phase-1-Technical-Report.pdf
Milestone 1.H: Micro-Raman analysis of synthetic complex methane hydrate (Subtask 5.2 and 5.3)	3/28/2018 (Y2Q2)	3/27/2018	Documentation of milestone achievement (Deliverable 5.1)	Complete, See Attachment G. Milestone 1.H Report in the Phase 1 Report at https://netl.doe.gov/files/oil-gas/fe0028967-Phase-1-Technical-Report.pdf
Milestone 2.A - Measurement of relative permeability in sand-pack cores (Subtask 6.1)	1/17/2019 (Y3Q2)	9/30/2019	Documentation of milestone achievement (Deliverable 6.1)	Revised Milestone Complete, See modification to approach below and Appendix A Milestone 2.A Report.
Milestone 2.B - Measurement of relative permeability in intact pressure cores (Subtask 6.1)	9/30/2019 (Y3Q4)	9/30/19	Documentation of milestone achievement (Deliverable 6.1)	Complete, See Appendix B Milestone 2.B Report.
Milestone 2.C - Depressurization of intact hydrate samples and documentation of thermodynamic behavior (Subtask 7.1 and 7.2)	9/30/2019 (Y3Q4)	9/30/2019	Documentation of milestone achievement (Deliverable 7.1)	Complete, See Appendix C Milestone 2.C Report

Milestone 2.D - Achieved gas production from GOM^2 samples monitored by micro-CT (Subtask 8.1 and 8.2)	9/30/2019 (Y3Q4)	9/30/2019	Documentation of milestone achievement (Deliverable 8.1)	Revised Milestone Complete, See modification to approach below and Appendix D Milestone 2.D Report.
Milestone 2.E - Building a chamber to prepare natural samples for 2D-3D micro-Raman analysis (Subtask 9.1 and 9.2)	1/17/2019 (Y3Q2)	3/31/19	Documentation of milestone achievement (Deliverable 9.1)	Complete, See Appendix E Milestone 2.E Report.
Milestone 2.F - 2D micro-Raman analysis of natural methane hydrate samples at depressurization (Subtask 9.1 and 9.2)	9/30/2019 (Y3Q4)	9/30/2019	Documentation of milestone achievement (Deliverable 9.1)	Complete, See Appendix F Milestone 2.F Report.

Project Data

All project raw data and spreadsheets are posted and available until at least September 30, 2024 at http://www-udc.ig.utexas.edu/hp3/.

Approach

We approached our analysis at two scales (Table 2). The 'Macro -scale' analysis considered the aggregate behavior of the porous medium. It included the measurement of relative permeability and the analysis of controlled depressurization of hydrate-bearing samples. The 'Micro-scale' explored the pore scale behavior. We used two approaches: micro-CT analysis and micro-Raman analysis.

At the onset of the experiment our approach was perform our experiments on synthetic hydrate samples. By synthetic, we mean that we formed the hydrate in the porous medium in the laboratory. Our intention was to extend the analysis to intact samples, if possible, in the later stages of the project.

Our intention was to use sand packs (samples formed from granular sediment) for initial experiments at both the macro and micro scales. We then planned to apply the developed experimental approaches to intact and depressurized sediment from the UT-GOM2-1 GC 955 Pressure Coring Expedition (reference). Sand was chosen to match the expected grain size and nature of the GC 955 sediment where possible.

Table 2. Summary of Approach

Macro-Scale	Micro-Scale
Relative Permeability : 1. Creation of sand packs with tunable hydrate saturation. 2. Perform co-injection of brine and gas to obtain gas/brine relative permeabilities in the presence of hydrate. 3. Analyze sand-packs and intact pressure cores.	**Micro-CT experiments** 1. Develop micro-scale Ko consolidation device 2. Image hydrate habit (pore filling, cementing) 3. Image hydrate habit evolution 4. Perform on sand-packs and depressurized cores from the field.
Depressurization Tests 1. Creation of sand packs with tunable hydrate saturation. 2. Performed controlled depressurization at range of hydrate saturations 3. Analyze sand-packs and intact pressure cores	**Micro-Raman experiments** 1. Observe hydrate formation and dissociation 2. Micro-scale phase distribution, and local diffusion associated with perturbation. 3. Perform on sand-packs and depressurized cores from the field.

Results and Discussion

1.0 Overview of Experimental Approach and Modifications to Initial Plan

Our overall goal was to perform experiments at conditions more or less reflective of in-situ marine hydrate conditions of GC-955 as described by (Flemings et al., 2018). The estimated pressure and temperature for GC 955 is shown in Figure 1A. However, we ran our experiments at lower pressures than are present at GC 955 because of limitations of our equipment. To stay within the methane hydrate stable zone, we ran the experiments at lower temperatures (Figure 1A). The relative permeability and micro-CT measurements were run relatively near the methane hydrate phase boundary to reflect the GC-955 conditions.

Our intention was to perform our experiments at a similar grain size to that present at GC-955. However, at the time we wrote the proposal we had not acquired those samples. The grain size from GC 955 turned out to be a sandy silt (Figure 1B, solid black triangles, previously called lithofacies 2), significantly finer than anticipated. All of our initial experiments (started before the grain size of the material was known) were run with materials at a larger grain size than that present at GC-955. In addition, we found that finer grained materials (silt and smaller) stretched the limits of our experimental capability. The first problem was that fines migrated in our relative permeability experiments. This resulted in a decision to switch to Berea sandstone for 3 phase relative permeability. The second problem is that we could not resolve at the pore scale and smaller in silt sized material in either the micro-CT or the Raman devices. As a result, we worked with coarser material. None the less, depressurized sediment or intact material from GC 955 was used where possible including some relative permeability measurements using the Pressure Core Center Permeameter and some micro-Raman studies. Our dissociation experiments run on synthetic material that was sand-sized (solid circles, Figure 1B). Our relative permeability experiments were all ultimately run with Berea sandstone (open triangles).

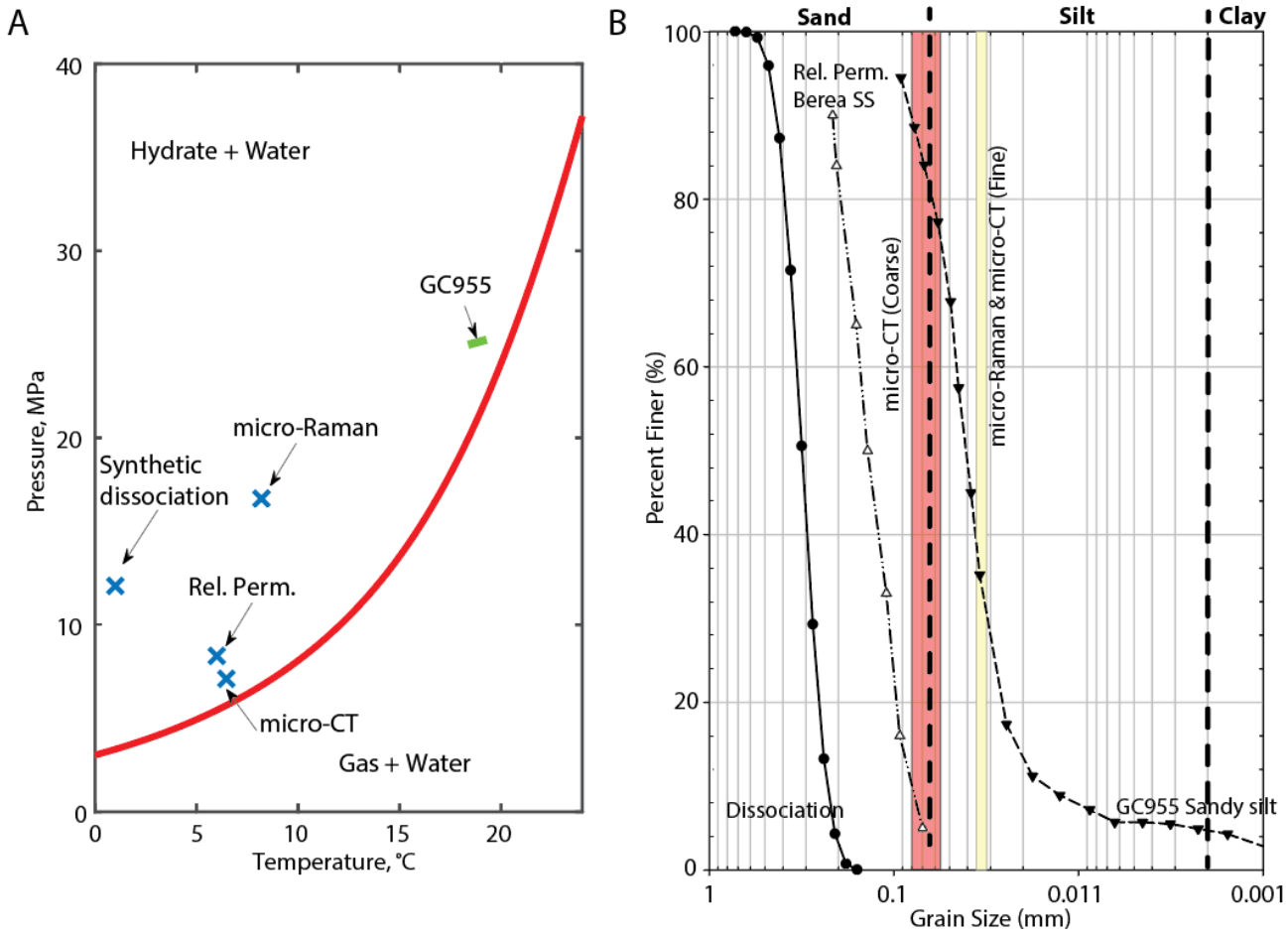

Figure 1. Summary of experimental conditions. A. Pressure and temperature of the GC 955 sandy silt material obtained from UT-GOM2-1 (green line) and the experiments conducted during this project (blue X's) compared to the methane hydrate stability boundary (red line). Conditions above and to the left of the red line are within the hydrate stability zone. X's represent the point of hydrate formation and the starting point for depressurization. B. Grain size distribution of the GC 955 sandy silt obtained during UT-GOM2-1 (dashed line with arrows) and quartz sand used in the experiments conducted during this project.

2.0 Hydrate Formation

One of the significant challenges of our project was how to manufacture porous media with a consistent methane hydrate saturation that was similar to natural intact samples. Generally, natural coarse-grained material containing gas hydrates are found at high saturation with only liquid and hydrate present (no vapor). In these systems it is commonly interpreted that the hydrates are present in the pore throats or form an inter-connected lattice, but they do not form a grain-coating cement. However, most manufacturing techniques involve the presence of free gas in some manner in order to get sufficient methane into the system to form high saturation hydrates.

We summarize our hydrate manufacturing techniques in Table 3. In our relative permeability experiments we saturated the system first with water. We then injected gas into the system and withdrew water at the opposite end under high pressure. We monitored the methane injected and the water removed and calculated the resultant gas saturation. Having established an interconnected gas phase, we then cooled the system at the constant elevated pressure until we entered the hydrate stability zone. We calculated the amount of hydrate formation (the hydrate saturation) by mass balance.

We manufactured hydrate bearing porous media in a different manner for our depressurization experiments. In these experiments, we cooled and pressurized the system into the hydrate stability zone. We then injected methane vapor while withdrawing water at the downstream end. We calculated the hydrate saturation by mass balance. We found that we could increase the hydrate saturation by lowering the gas injection rate.

In our micro-Raman experiments, we initially had methane vapor in the sample holder. We then injected brine at high pressure, compressing the initial gas volume significantly. We then cooled the system and formed hydrate. Finally, in our micro-CT experiments we utilized two methods. First, we did excess-gas formation experiments by packing sand and brine at near residual water saturation and then pressurizing the system with methane gas and cooling it to take it to the hydrate stability zone (we also tried cooling first and then pressurization). Second, we did excess-water experiments by saturating the sandpack.

Table 3. Summary of the hydrate formation conditions for each pressure chamber.

Focus	Media	Formation Conditions	S_h Limitations	Bulk S_h achieved
Relative Permeability	Berea Sandstone Φ=20-30% k=~250 md	Sample saturated with water. Gas then injected to achieve gas saturation. Chamber pressurized with methane then cooled to HSZ. Constant pressure maintained with methane.	Limited by initial water saturation and pore-water salinity	10-60%
Depressurization	Quartz sand packed with air pluviation d50=315 µm Φ=35-40%	Sand saturated with water ranging from freshwater to 2x seawater. Gas injected (under hydrate-stable conditions) from one end by withdrawing brine from the other end of the sample.	Formation method results in blockages from hydrate formation and pressure drawdowns on the downstream end. Eventually gas breaks through to outlet.	13 to 27%
Micro-CT	710 microns 100% sand	Sample saturated with water. Methane then injected, then cooled to HSZ. Constant pressure maintained with gas (Xenon or methane).	Limited by water in the system, hydrate ages and saturation increases, high degree of heterogeneity	10 to 60% (Xenon and methane)
Micro Raman	149-297 micron 100% sand	Sample originally saturated with gas. Water then pushed into sample and then cooled to HSZ. Constant pressure maintained with water.	Limited by initial gas content in the system	10-30%

3.0 Macro-Scale: Relative Permeability of Methane Hydrate Sand Packs

3.1 Permeability Summary

We have successfully built a laboratory apparatus for the measurement of relative permeability at the core scale, creating a sand pack, and forming hydrate in that sand pack. We then optimized our method of sand packing to directly control the mass of water added. We generated hydrate, obtaining final hydrate saturations of up to 43%, and began looking at pressure profiles within the sand pack. In Phase 2 we made the first ever measurements of three-phase permeability of gas and water flowing simultaneously in the presence of hydrate. We also measured two-phase permeability of brine or gas in the presence of hydrate and demonstrated that the relative permeability of brine in the presence of hydrate (no gas) behaves just like the relative permeability of brine in the presence of gas (no hydrate). We showed that the three-phase relative permeability of gas and water in the presence of hydrate may also be understood using simple wettability arguments and existing models where gas and hydrate act like non-wetting phases. We also measured relative permeability of a couple natural hydrate-bearing samples from GC 955 and compared results to the relative permeability of water at different hydrate saturations in Berea cores noting similar, predicted behavior. Our results support a model where water is the most wetting phase, hydrate is the intermediate wetting phase, and gas is the least wetting phase. This model can be used to predict relative permeability of gas and water in the presence of hydrate. This relative permeability model will provide a rigorous foundation for reservoir simulation to more accurately forecast water and gas production.

3.2 Hydrate Formation (Permeability)

We have developed two methods of hydrate formation: low saturation and high saturation. The low saturation method produces hydrate saturations between 5-25%. The high saturation method produces hydrate saturation between 30-60%. The same equipment and setup is used for both experiments (Figure 2).

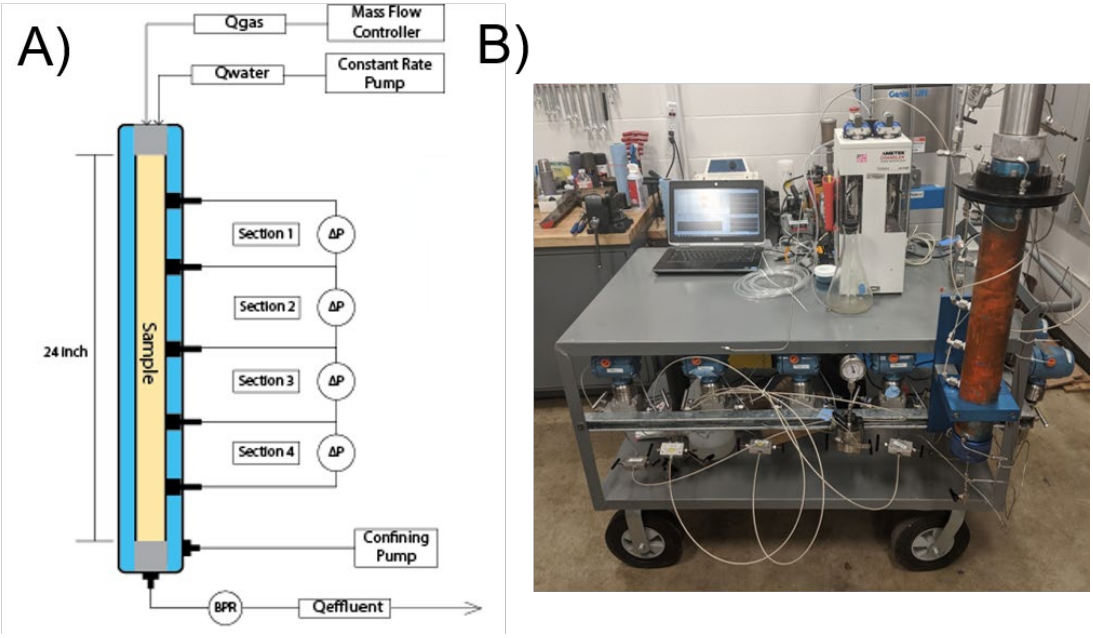

Figure 2. Permeability Experimental setup. A) Diagram of pressure vessel with 24" inch core, 5 incremental pressure taps, 4 differential pressure transducers, gas pump, water pump, and back pressure regulator. B) Photo of vessel attached to cart which is moved into cold storage room.

3.2.1 Low saturation method

To achieve a low hydrate saturation (5-25%), the core begins fully brine saturated. A mass flow controller is attached to the upstream end of the core. Methane gas is injected into the core at a constant flow rate (<0.5 ml/min) to displace brine. The effluent is captured and weighed to determine phase saturation using mass balance. Gas is injected until no more brine is removed from the system. From this saturation method, the initial gas saturation will range from 15-25%.

3.2.2 High saturation method

To achieve a high hydrate saturation (25-40%), the core begins fully dry. The sample is placed in an oven for at least 2 days to allow all water to evaporate. Once dry, the sample is placed in the pressure vessel and an effective stress of 2.76 MPa (400 psi) is applied. Methane gas is flowed through the core to replace the air in the system. The outlet is then shut, and brine is injected into the core until the desired bulk brine saturation is reached. For the high saturation method, the initial water saturation will range from 40-60%.

3.2.3 Hydrate Formation

Once the initial saturation is achieved, there is a known mass of water, gas, and salt in the core. Mass balance is used to calculate the phase saturation of gas, brine, and hydrate throughout the experiment. After the initial saturation is determined, the same procedure and pressure-temperature path is followed for all samples (Figure 3).

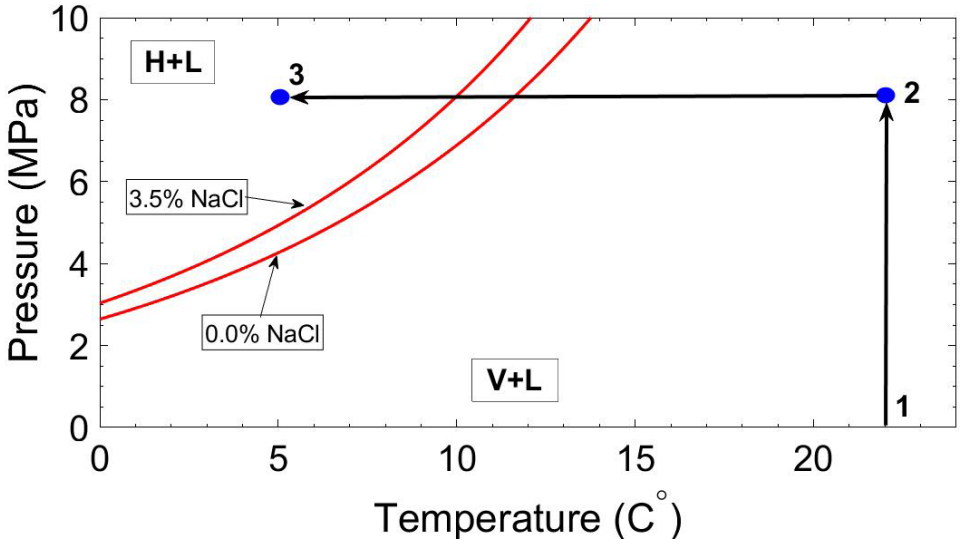

Figure 3. Pressure-Temperature diagram for hydrate for hydrate with permeability hydrate formation conditions. Arrows indicate experimental path for hydrate formation. 1 to 2) Initial pressurization from 0 to ~8 MPa with methane gas. 2-3) Samples is cooled from 22°C to 6°C and sample enters hydrate stability zone. 3) Pressure and temperature are held constant as hydrate formation begins.

The upstream end of the sample is connected to a Teledyne ISCO syringe pump that is completely filled with methane gas. The ISCO pump has a cylinder volume of 265 ml. Next, the downstream end of the sample is shut-in, and the pore pressure and confining are increased simultaneously to maintain a constant effective stress (2 MPa). Once experimental conditions are reached (8 MPa, Figure 3), the ISCO pump is set to maintain a constant pressure.

The sample is left at room temperature to ensure no leaks are present. If the leak rate is <0.5 ml/hour, the entire system is transported into the cold storage room where the temperature is a constant 6°C. Since the pump is set to constant pressure, gas will be injected to maintain pressure as the gas compresses due to temperature effects.

The sample is kept at constant pressure and temperature until hydrate formation occurs. Hydrate nucleation will usually occur between 2-45 hours after reaching experimental conditions. Since the density of hydrate is less than the density of brine, the pore pressure will decrease as hydrate forms. To maintain experimental conditions and a constant pressure, additional gas is injected as hydrate forms.

The pore-water salinity will increase as hydrate forms and salt is excluded (You et al., 2015). For the low saturation method, the high initial brine saturation and low initial salinity will prevent the sample from

nearing three-phase stability conditions. For the high saturation method, depending on the conversion rate of water into hydrate, the sample may approach three-phase stability. Hydrate formation will continue until all water is converted to hydrate or the system reaches three-phase stability. However, after the initial nucleation event, the formation rate slows significantly, and little additional hydrate will form. Once the formation stalls (no additional gas is injected from the pump), the hydrate, gas, and water saturation, and salinity are calculated using mass balance.

3.2.4 Determining the hydrate saturation

The resulting hydrate saturation, $S_{h,}$ is calculated as follows:

$$S_h = \frac{V_{CH4}\rho_{CH4}M_H}{M_{CH4}\rho_H V_p}, \quad \text{(Eq. 1)}$$

where V_{CH4} is the volume of methane injected into the core during hydrate formation, ρ_{CH4} is the density of methane gas at experimental conditions (0.07225 g/cm^3), M_H is the molar mass of sI hydrate (119.5 g/mol), M_{CH4} is the molar mass of methane (16 g/mol), ρ_H is the density of sI hydrate (0.925 g/cm^3), and V_p is the pore volume of the sandpack. The conversion rate R, which is the ratio of the number of moles of water taken up in hydrate to the total number of moles of water initially present, is calculated as

$$R = \frac{V_W\rho_W M_{CH4}}{5.75 M_W V_{CH4}\rho_{CH4}M_H}, \quad \text{(Eq. 2)}$$

where V_W is the initial volume of water present, ρ_w is the density of water, and M_w is the molar mass of water. Since the initial conditions are known and the input and output are monitored throughout the experiment, the phase saturations and salinity can be calculated at any time (e.g. Figure 4).

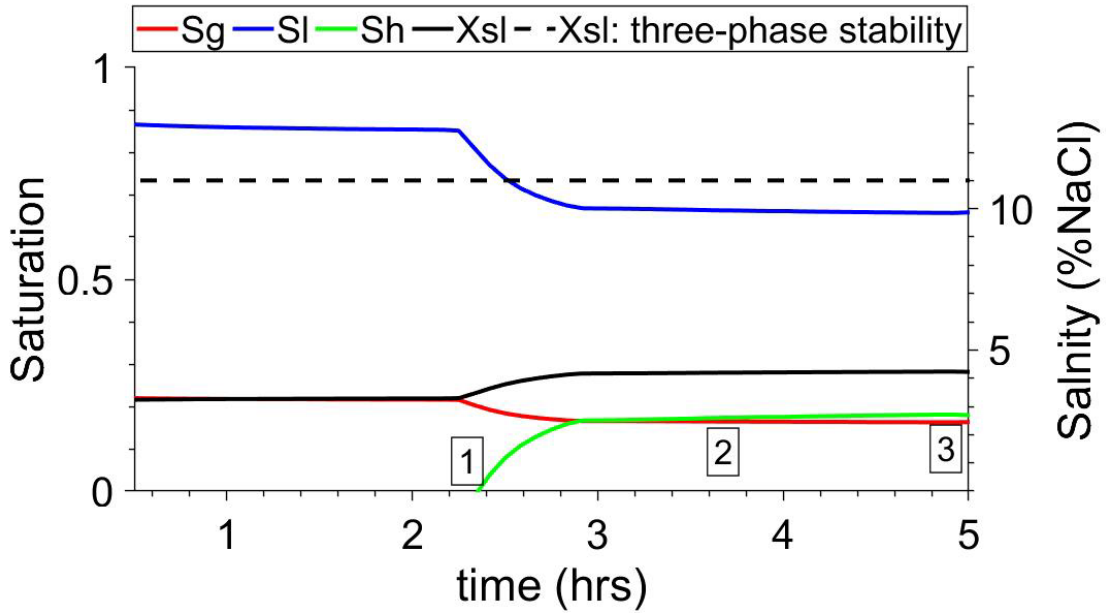

Figure 4 Example of mass balance analysis for hydrate formation procedure. Phase saturations and salinity can be tracked throughout experiment. 1. Initial hydrate nucleation event. 2. Hydrate formation rate slows. 3. Hydrate formation experiment stops.

3.3 Relative permeability measurements

3.3.1 Steady-state relative permeability

The saturation, and therefore the connectedness, of each phase will impact the ability of each phase to flow through the pore space. Permeability is the measured parameter that determines how well a fluid will flow in a system. When only one phase is present, the absolute (intrinsic) permeability of the porous media is measured. As multiple phases enter the pore space, each phase will have its own effective permeability. Due to the saturation path, which is controlled by pore size distribution and capillary pressure, the relative permeability will not follow a linear path (e.g. Figure 5). Relative permeability will be concave up, and the concavity of the relative permeability will determine the flow behavior of the system.

The absolute permeability (k_{abs}) is described by Darcy's Law (Equation 3) and is valid for porous media saturated with only one phase (e.g. water):

$$k_{abs} = \frac{Q \cdot \mu}{A}\left(\frac{L}{\Delta P}\right) \quad \text{(Eq. 3)}$$

Where k is the absolute permeability (m^2), Q is the flow rate (m^3/s), μ is the viscosity (Pa-s), L is length (m), A is area (m^2), and ΔP is pressure drop (Pa).

The effective permeability (k_{eff}) (Equation 4) is valid for porous media saturated with more than one phase. Each phase will have a different effective permeability. The effective permeability of phase (i) is described by:

$$k_{eff(i)} = \frac{Q_i \cdot \mu_i}{A}\left(\frac{L}{\Delta P_i}\right) \quad \text{(Eq. 4)}$$

Where $k_{eff,i}$ is the effective permeability (m^2) of phase i, Q_i is the flow rate (m^3/sec) of phase i, μ_i is the viscosity (Pa-s) of phase i, L is length (m), A is area (m^2), and ΔP_i is pressure drop (Pa) of phase i.

The unitless ratio of the effective permeability to the absolute permeability is the relative permeability (Equation 5).

$$k_{r(i)} = \frac{k_{eff(i)}}{k_{abs}} \quad \text{(Eq. 5)}$$

Relative permeability is found to scale with the saturation of the relevant phase. For example, as more of the non-wetting phase is added, the effective permeability of the wetting phase will decrease, and the effective permeability of the non-wetting phase will increase.

3.3.2 Current understanding of relative permeability in a hydrate-liquid system

The Brooks-Corey model is the most commonly used model for relative permeability as a function of wetting and non-wetting saturation (S_w and S_n) (Brooks and Corey, 1964). The Brooks-Corey model is frequently used in hydrate simulations:

$$k_{rw} = \left(\frac{S_w - S_{rw}}{1 - S_{rw}}\right)^{n_w} \quad \text{(Eq. 6)}$$

$$k_{rn} = \left(\frac{S_n - S_{rn}}{1 - S_{rn}}\right)^{n_n} \quad \text{(Eq. 7)}$$

where S_{rw} is the residual water saturation, S_{rn} is the residual non-wetting phase saturation, and n_w and n_n are fitting parameters for wetting and non-wetting phases. Brooks-Corey models are commonly used due to their simplicity (Figure 5).

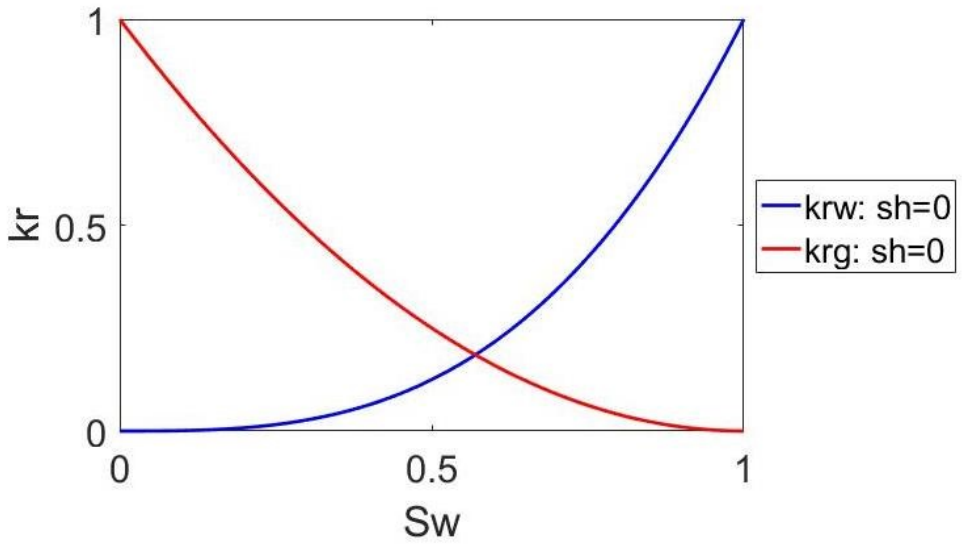

Figure 5. Brooks-Corey relative permeability for gas and water with n_w = 4 and n_n = 2. Red line is from eq. 6, and blue line is from eq. 7.

Multiple studies have attempted to apply the principles of Brooks and Corey (1964) to hydrate systems by adding additional fitting terms and making assumptions about the pore habit of hydrate. For example, Kleinberg et al. (2003) developed a method to determine the reduction in permeability (relative permeability) of water due to hydrate saturation. A model was developed to determine the porosity and permeability reduction caused by either pore coating (Equation 8) or pore filling (Equation 9) hydrate:

$$k_{r,w} = k_{abs}\left[1 - S_h^2 + \frac{2\left(1-S_h^2\right)^2}{\log S_h}\right] \quad \text{(Eq. 8)}$$

$$k_{r,w} = k_{abs}(1 - S_h)^2 \quad \text{(Eq. 9)}$$

These models give an expected drop in permeability caused by a certain hydrate saturation (Figure 6).

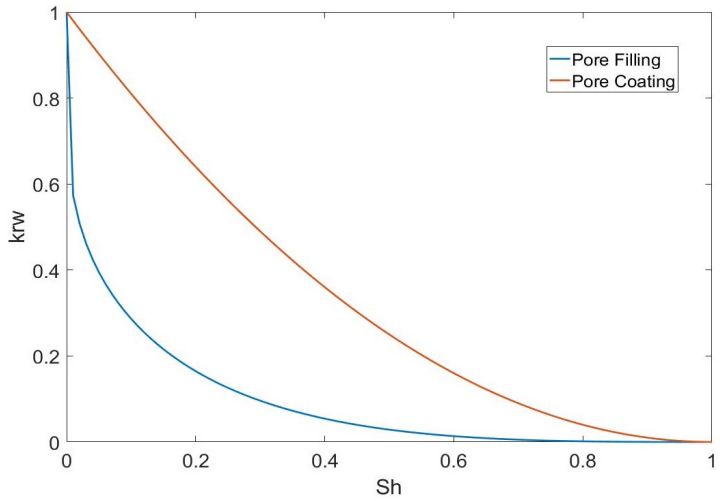

Figure 6. Modeled reduction in permeability (relative permeability) due to the presence of hydrate as a pore filling or pore coating phase (Kleinberg et al., 2003). Red line is from eq. 8, and blue line is from eq. 9.

This approach has many shortcomings, including an unrealistic representation of hydrate growth in the pore network and a wide range of possible relative permeabilities at a particular hydrate saturation. Despite its shortcomings, the Kleinberg method is still the primary method used to model relative permeability in a hydrate system.

3.3.3 Two-phase relative permeability

A Berea sandstone core was selected since the permeability (~220 mD) is comparable to that of marine sediment that is of interest to the hydrate community. Before hydrates were formed, the complete drainage gas-water relative permeability curve was measured, a key step that no other hydrate relative permeability experiments have conducted. Gas-water relative permeability for Berea Sandstone has been well studied and provides a good database to confirm and compare results.

First, relative permeability experiments are run in a hydrate free sample (Figure 7A). A Brooks-Corey model can be fit to this data (Figure 7B). The results from this test were compared to published data for a Berea Sandstone gas-water relative permeability and a good fit was found (Chen et al., 2017).

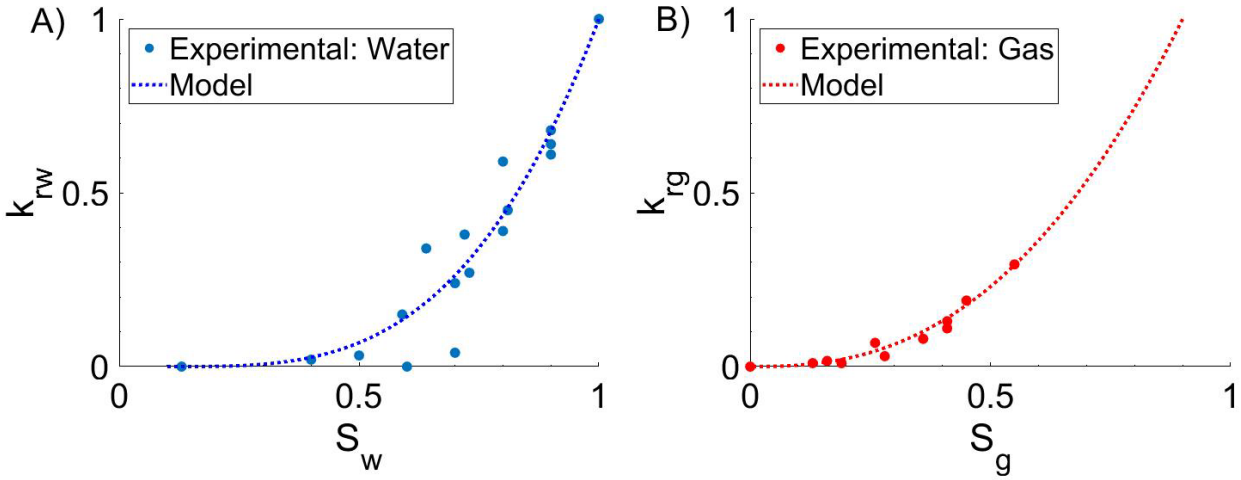

Figure 7 A) Two-phase water relative permeability data for a Berea Sandstone core. A Brooks-Corey model is fit to the experimental data (nw=3.5, Srw=0.15). B) Two-phase gas relative permeability data for a Berea Sandstone core. A Brooks-Corey model is fit to the experimental data (ng=2.5, Srg=0.0).

After running the experiments in the hydrate free sample, hydrate was formed at four different saturations (0.6, 0.45, 0.25, 0.12). The remaining free gas was purged from the system until a two-phase system is achieved. Water was then injected at three different flow rates for each saturation (0.1, 0.05, 0.01 ml/min). The effective permeability of water was measured at each saturation and flow rate. The results were then compared to the gas, water system (Figure 8).

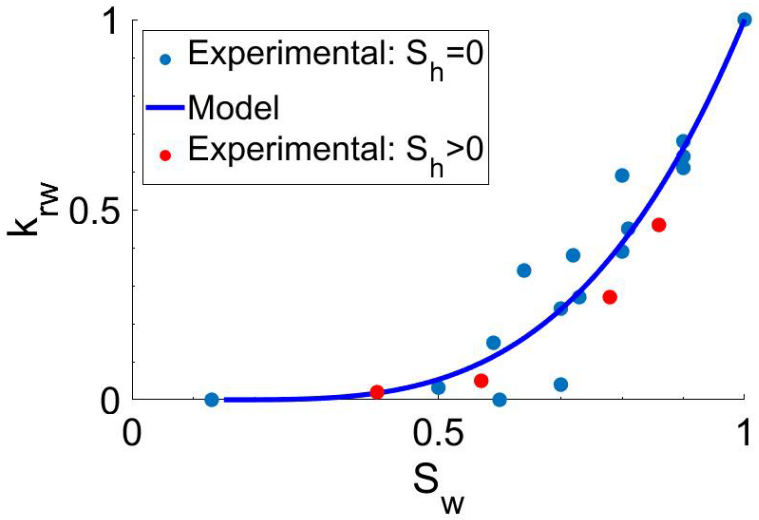

Figure 8 Comparison of relative permeability of water in presence of hydrate (red) and in presence of gas (blue). Relative permeability behavior is same for both systems, suggesting that gas and hydrate both act as a non-wetting phase.

At any hydrate saturation, the water relative permeability was found to act similarly to water relative permeability at equivalent gas saturation. Therefore, hydrate was interpreted to act as the non-wetting phase and k_{rw} can be modeled as a two-phase wetting/non-wetting system using a Brooks-Corey type model.

In a two-phase system with hydrate and water, water is the wetting phase and therefore occupies the smallest pores in a water wet media. A two-phase hydrate/water scenario should behave similarly to a gas/water or water/oil relative permeability and can therefore be modeled with Brooks-Corey. Early experiments have shown that hydrate/water behavior is consistent with gas/water. Hydrate or gas will occupy the largest pores and water will occupy the smaller pores. This behavior should not change if hydrate replaces gas as the non-wetting phase. Therefore, by measuring the two-phase gas/water relative permeability of a porous media, the water/hydrate relative permeability of the rock can be modeled. At any hydrate saturation, the water relative permeability will fall along the two-phase gas/water relative permeability (Figure 9). This fundamental understanding has been missing from the current hydrate literature.

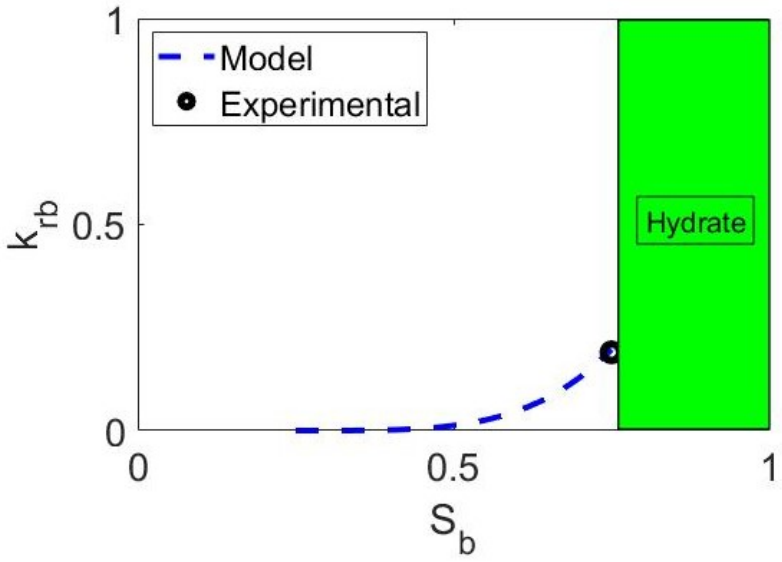

Figure 9. Brine relative permeability with hydrate filling the largest 25% of pores. Blue dashed line is the model prediction. The black circle represents the measured value.

3.3.4 Three-phase relative permeability

Our proposed approach for modeling three-phase (hydrate, gas, and water) relative permeability is to use the Saturation Weighted Interpolation (SWI) method. For the intermediate phase, the SWI method uses the two endmember relative permeability curves and weights them depending on the other two-phase saturations (e.g. brine and hydrate).

For example, if $S_h = 0.25$, then $k_{r,w} \approx 0.13$. A scaled Brooks-Corey model (Brooks and Corey, 1964) can be determined by combining the two-phase Brooks-Corey equation with the pore-filling hydrate relative permeability model of Kleinberg et al. (2003):

$$k_{r,w} = \left(\frac{S_w - S_{r,w}}{1 - S_{r,w}}\right)^{n_w} \left(k_{abs}\left[1 - S_h^2 + \frac{2\left(1 - S_h^2\right)^2}{\log S_h}\right]\right), \quad \text{(Eq. 10)}$$

$$k_{r,g} = \left(\frac{S_g - S_{r,g}}{1 - S_{r,g}}\right)^{n_g} \left(k_{abs}\left[1 - S_h^2 + \frac{2\left(1 - S_h^2\right)^2}{\log S_h}\right]\right), \quad \text{(Eq. 11)}$$

where S_w is water saturation, $S_{r,w}$ is the residual water saturation, n_w is the water exponent, S_h is hydrate saturation, S_g is gas saturation, $S_{r,g}$ is the residual gas saturation, and n_g is the gas exponent. Figure 10 shows some example relative permeability predictions with (10) and (11).

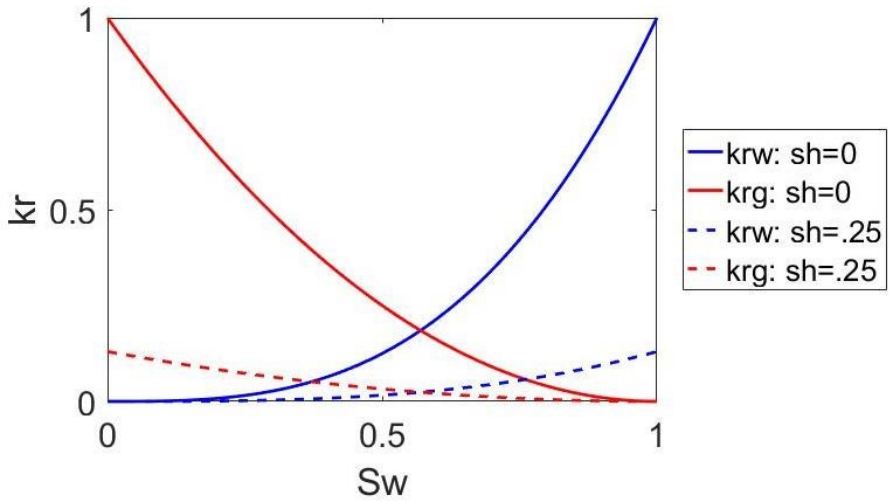

F*igure 10. Brooks-Corey relative permeability model without hydrate, and scaled for 25% hydrate saturation. The hydrate-free Brooks-Corey model is scaled with* $k_{r,w} = 0.13$.

Relative permeability is traditionally plotted as a function of water saturation. However, due to equipment limitations and difficulty in measuring three-phase saturation, the relative permeability data is plotted against the fraction flow rate of water f_w:

$$f_w = \frac{Q_w}{Q_w + Q_g}, \quad \text{(Eq. 12)}$$

where Q_w is the water volumetric flow rate and Q_g is the gas volumetric flow rate. For experimental data, the flow rates are set throughout the experiment. Therefore, f_w is an experimental parameter that is known at all points during each experiment. However, flow rate is not a parameter in modeled relative permeability. S_w must be converted into f_w by assuming plug flow and assuming that:

$$V_{eff} = V_{pore}(1 - S_h), \quad \text{(Eq. 13)}$$

$$f_w = \frac{S_w}{V_{eff}} \quad \text{(Eq. 14)}$$

where V_{eff} is the effective (fluid-filled) pore volume and V_{pore} is the total pore volume. Since the experimental data will be plotted against f_w, all models must be converted in order to be directly compared. If the plug flow assumption is not valid, f_w can also be solved for using the Darcy-Buckingham equation (9). Combining (9) and (12):

$$f_w = \frac{\frac{k_{r,w}}{\mu_w}}{\frac{k_{r,w}}{\mu_w} + \frac{k_{r,g}}{\mu_g}}. \quad \text{(Eq. 15)}$$

The viscosities and relative permeabilities are known. Therefore, the fraction flow of water (f_w) can be solved for each model. This conversion allows comparison of preliminary experimental results, but saturations must still be determined.

Experimentally measured three-phase relative permeability data was collected using the method described in Murphy (2018). Before hydrate formation, a two-phase (gas/water) drainage relative permeability curve was measured for the sample (Fig. 7). Hydrates were then formed using the excess gas method. The hydrate saturation was estimated to be 25%. Initially, only brine was flowed through the core. The resulting values are simply endpoint relative permeability points (f_w = 1). Gas is then co-injected into the core to decrease the f_w value. Steady-state ($\partial P/\partial t = 0$) is reached at each value of f_w. The gas and water relative permeability values are measured at each f_w until f_w = 0 (Figure 11).

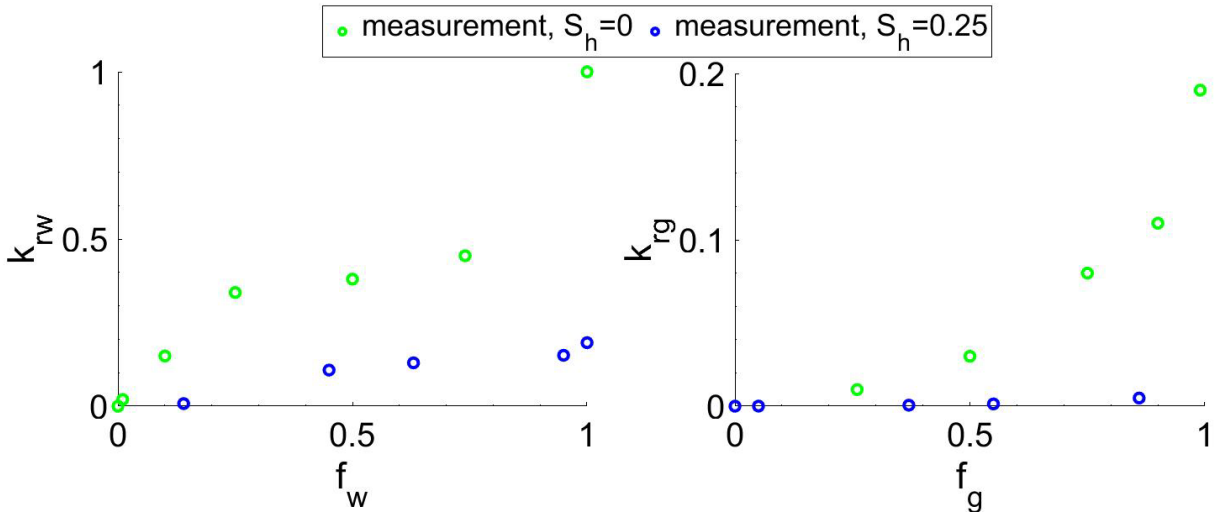

Figure 11. Experimentally measured gas and water relative permeability in the presence of hydrate (S_h = 0.25).

The experimentally derived relative permeability curves can be used to compare to the models discussed previously. Using the Kleinberg et al. (2003) scaling approach for S_h = 0.25 and $k_{r,w}$ = 0.13. The experimentally measured relative permeability with no hydrate is then scaled by 0.13 (Figure 11).

The observed behavior may be predicted by considering which portion of the pore size distribution will be occupied by each phase. Since the gas-water interfacial tension is larger than the hydrate-water interfacial tension (72 N/m versus 27 N/m; Clennell et al., 1999), it is expected that gas will occupy the largest pores while hydrate will occupy the intermediate pores. Water, being the wetting phase, will occupy the smallest pores. This arrangement is illustrated in Figure 12.

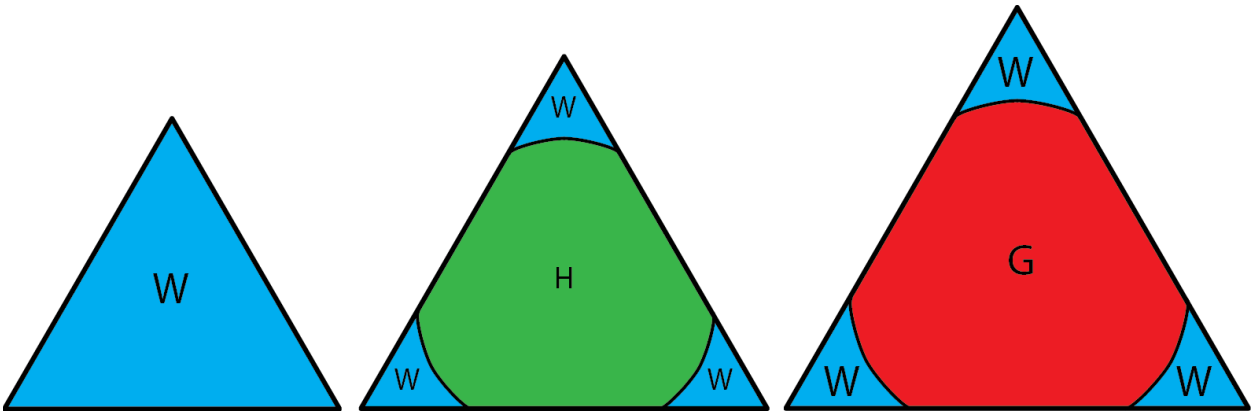

Figure 12. Illustration of configuration of phases in pores of different sizes.The pores are assumed to extend into the page.

Based on this assumption, the relative permeability of the gas phase should depend only on the gas saturation and will follow the behavior observed in the two-phase case. The relative permeability of the water phase will depend only on the water saturation and will also follow the behavior observed in the two-phase case. Figure 13 shows predicted relative permeabilities versus fractional flow of water and gas under these assumptions. The fit to the measured data is good.

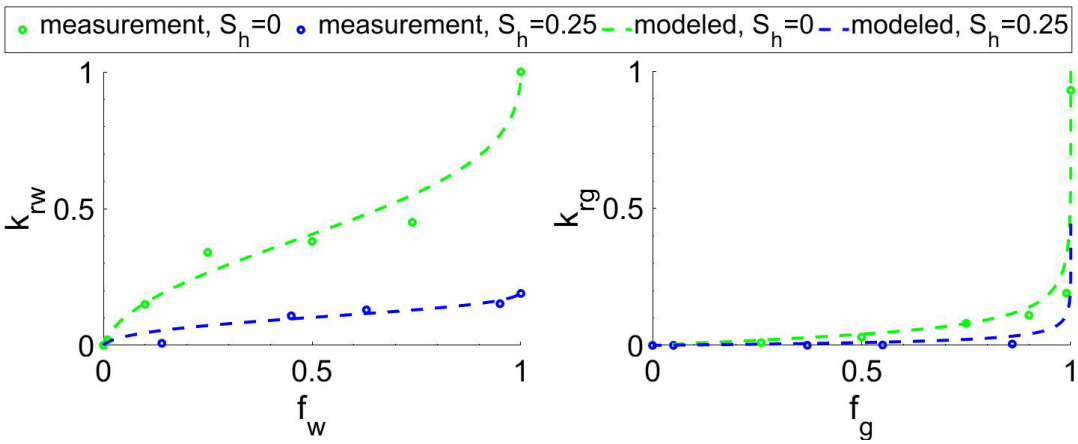

Figure 13. Model comparison with three-phase relative permeability data.

3.4 Relative permeability of intact pressure cores

To compare our laboratory results with measurements on real material, we measured the relative permeability of brine in the presence of hydrates in intact pressure cores from Green Canyon 955 in the Gulf of Mexico. Two samples of hydrate-bearing sandy silt were selected based on x-ray images, bulk density measurements, and acoustic velocity measurements made with the Geotek pressure core analysis and transfer system (PCATS). The two samples had hydrate saturations of 83% and 90%.

The pressure cores were first subsampled and transferred to the permeameter chamber using the Geotek mini-PCATS, Figure 14. The cores were maintained at a pressure of 25 MPa and a temperature of 6-7°C throughout the process.

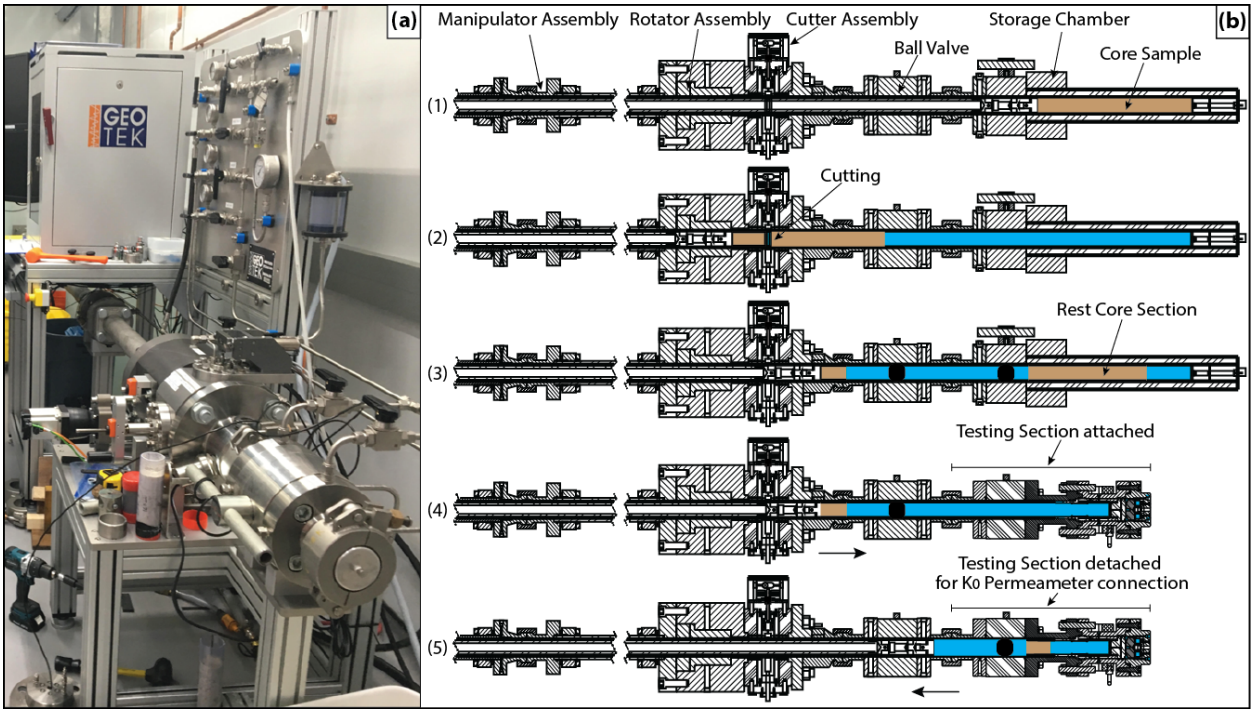

Figure 14. Mini-PCATS cutting and transfer (a) Photograph of mini-PCATS in use. (b) Cutting and transfer process to place intact pressure core material in the permeameter.

In the cutting and transfer process, the main storage chamber is connected to the cutter assembly with a ball valve (Figure 14, 1). The sample is then pulled into the cutter using the manipulator and the desired section is cut (Figure 14, 2). The remaining portion of the original core is then pushed back into the storage chamber (Figure 14, 3). The storage chamber is removed and the permeameter is then connected to the ball valve (Figure 14, 4). Once the permeameter is connected, the cut sample is pushed into the permeameter (Figure 14, 5). The permeameter can then be disconnected and moved to the analysis room.

Once in the permeameter cell, the sample is reconsolidated to the estimated in situ effective stresses. During this process, several measurements of effective permeability were made. These measurements were done using steady-state flow of brine through the core. Results are shown in Figure 15a. Once the target effective stresses were reached and the effective permeability measured, the sample was degassed at constant horizontal effective stress. After degassing, the sample was vacuumed and re-saturated with brine to measure the intrinsic permeability, which was assumed to be the permeability of the sediment in the absence of hydrate. As Figure 15b shows, for some samples the intrinsic permeability was lower than the effective permeability with hydrate in the pore space, which is counterintuitive. This phenomenon was attributed to the migration of fine particles during the test.

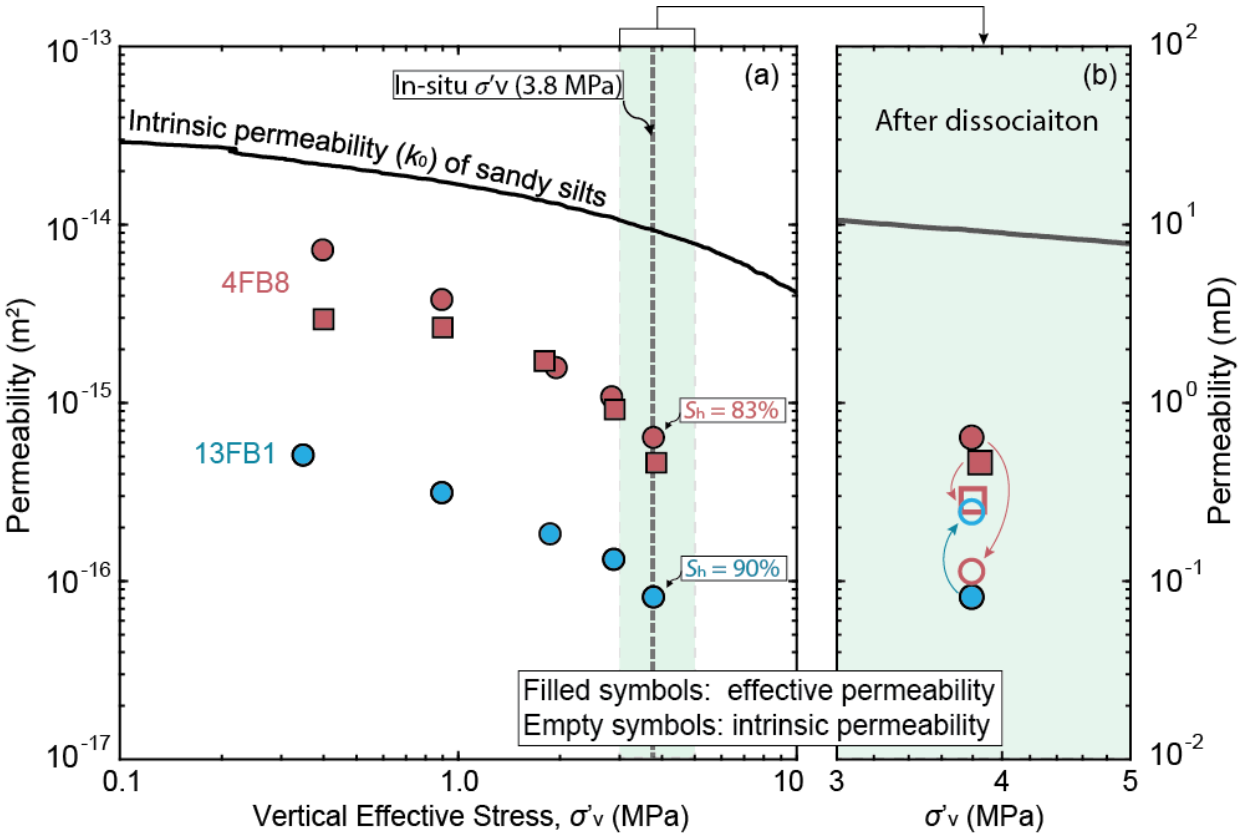

Figure 15. GC 955 sandy silt effective and intrinsic permeability (a) Effective permeabilities measured during reconsolidation to in situ conditions. (b) Change in permeability after degassing. Note that sample 4FB8 experienced a decrease in permeability after degassing, which was unexpected.

To obtain a better estimate of the intrinsic permeability, the samples were dried and resedimented to the in situ vertical effective stress in a consolidation cell. The resedimentation process allowed us to remove the effects of fines migration and any fabric disturbance that would have occurred as a result of degassing. Permeability was then measured during a consolidation test. Using the resulting intrinsic permeability values, we were able to determine the in situ relative permeabilities of the samples. The resulting values fit with the trend of the synthetic samples and help define the portion of the data at high hydrate saturations that we did not achieve in the laboratory. The results are shown in Figure 16.

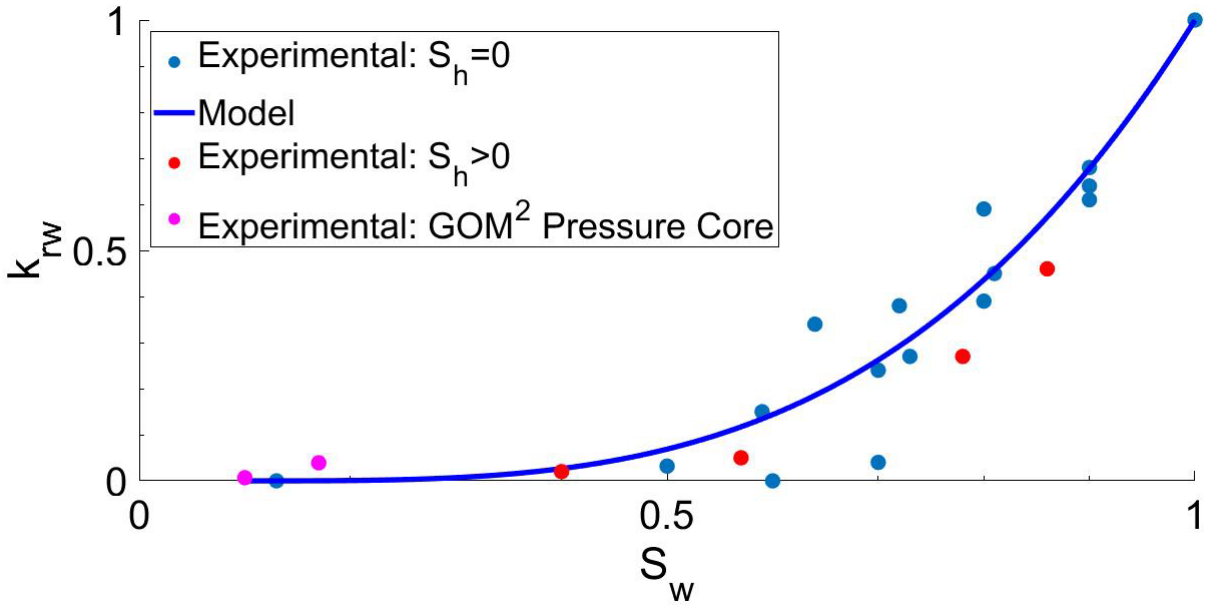

Figure 16. Wetting-phase relative permeability values for all samples tested. Blue dots: water-phase relative permeability in the presence of methane gas in synthetic samples. Red dots: water-phase relative permeability in the presence of hydrate (no gas) in synthetic samples. Magenta dots: water-phase relative permeability in the presence of hydrate (no gas) in intact pressure core samples.

4.0 Macro-Scale: Depressurization of Methane Hydrate Sand Packs

4.1 Depressurization Summary

We have successfully formed and dissociated hydrates in sand packs, some while scanning with a CT, and achieved a mass balance in the total amount of methane through consumed during formation and recovered during dissociation. We have dissociated methane hydrate in both synthetic sand packs and sandy silt sediments from the northern Gulf of Mexico. In these experiments we monitor the pressure response and compare to what would be expected if the sample had homogenous salinity and temperature (bulk equilibrium). We show that the in situ salinity of a hydrate-bearing sample can be estimated during slow depressurization by observing the first pressure rebounds that occur at the onset of hydrate dissociation. We also show that as dissociation continues the local freshwater produced surrounding the dissociating hydrate causes the sample to follow the freshwater phase boundary even though the average salinity in the sample is much higher. This local equilibrium effect suggests that models of hydrate production should use the freshwater boundary in simulations as the grid scale, and the pressure drawdown for hydrate production could be 2-4 MPa greater in deepwater hydrate reservoirs.

4.2 Hydrate Formation in the depressurization chamber

4.2.1 The Pressure Vessel and Experimental Setup

Figure 17 shows a schematic diagram of the hydrate chamber. We created a sand pack by filling a Viton rubber sleeve with industrial sand with steel end caps on each end. The synthetic sand core is housed within an aluminum vessel filled with a confining fluid. Inlet and outlet ports at each end of the sample allow the flow of gas and water into and out of the sample. Pressure was measured at the inlet/outlet valves and in the confining fluid. Temperature was measured in the confining fluid.

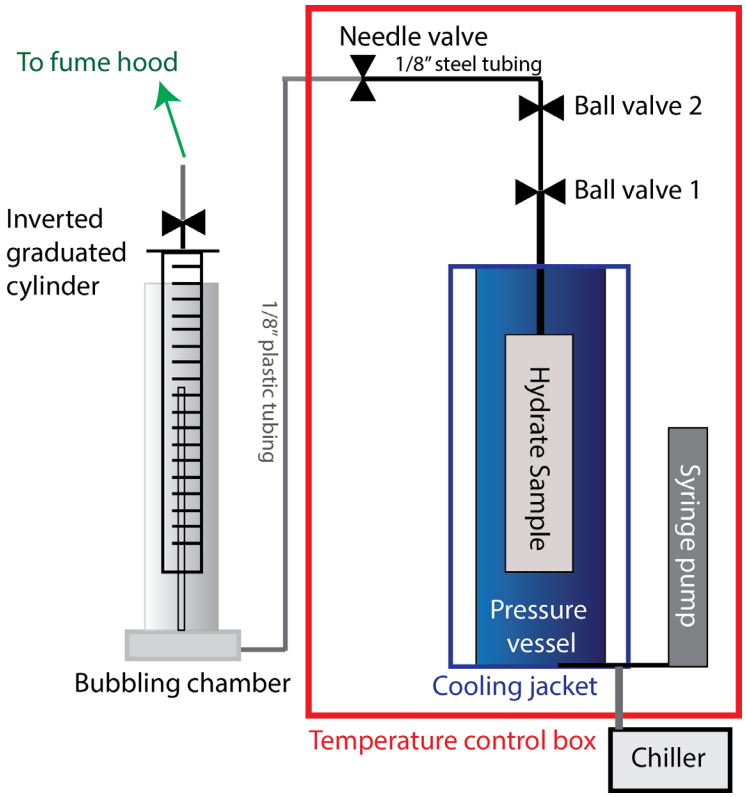

Figure 17. Diagram showing the setup of the hydrate formation / depressurization chamber. From (Phillips et al., 2019)

4.2.2 Hydrate formation method

Methane was injected into the sand pack saturated with NaCl brine or freshwater while the system was within the hydrate stability zone. Methane gas at the upstream end was held at constant pressure while brine was removed at a constant rate. The volume of the upstream gas pump and downstream brine pump were monitored continuously as well as the pressure at the inlet and outlet valves. The methane hydrate saturation was calculated by the mass balance of gas and water consumed. This approach is outlined in more detail in (Meyer et al., 2018). Hydrate formation with the gas injection method yielded hydrate saturations ranging from 13% to 32%.

4.3 Depressurization Results

We depressurized the sample by releasing a constant volume of gas from the top of the sample into a constant volume of tubing. This gas was then expanded into an inverted graduated cylinder and the volume at atmospheric pressure was recorded. We monitored the pressure in the sample at each step and the pressure rebound that occurred between each step.

The depressurization of each sample yielded a consistent pressure vs. volume curve in which free gas was released, followed by hydrate dissociation, then release of residual gas (Figure 18). During hydrate

dissociation, there is a decrease in the slope in the pressure vs. methane released curve, and pressure rebounds occur between gas releases during dissociation while the sample is shut-in.

Overall, we observed an excellent mass balance between total methane consumed during formation to methane recovered during depressurization (Figure 19). The methane mass balance matched to within 6% (within the uncertainty of our experimental set up) due to the temperature gradient in the gas at the top of the sample. We show that there are no significant leaks and the pressure rebound behavior we observe is a result of dissociation of the specimen.

We estimated salinity of the sample based on the pressure and temperature of the sample at the onset of dissociation and using the phase boundary of methane hydrate. This salinity estimate matches closely to the known salinity of the sample and we suggest that slow depressurization of pressure cores can be used to estimate the in situ salinity of the pore fluids.

Once dissociation begins, the decrease in pressure during dissociation is larger than predicted by an equilibrium model assuming well-mixed salinity and temperature conditions (Figure 20). Even a very slow stepwise depressurization over several weeks will not follow conditions expected for a homogenous sample. During dissociation we also observe pressure rebounds that occur over several days with the slowest pressure recover occurring the highest salinity samples (Figure 21). The shape of the pressure rebound evolves over the course of dissociation becoming more concave-up later during dissociation (Figure 22). Overall, we show that local equilibrium due to pore water freshening dominates during sustained (even slow) dissociation (Figure 23). We suggest that hydrate production scenarios should be modeled using the freshwater phase boundary at the scale of the grid block. In deepwater settings, maintaining dissociation at the freshwater as opposed to the seawater phase boundary can require 2 to 4 MPa larger pressure drawdown.

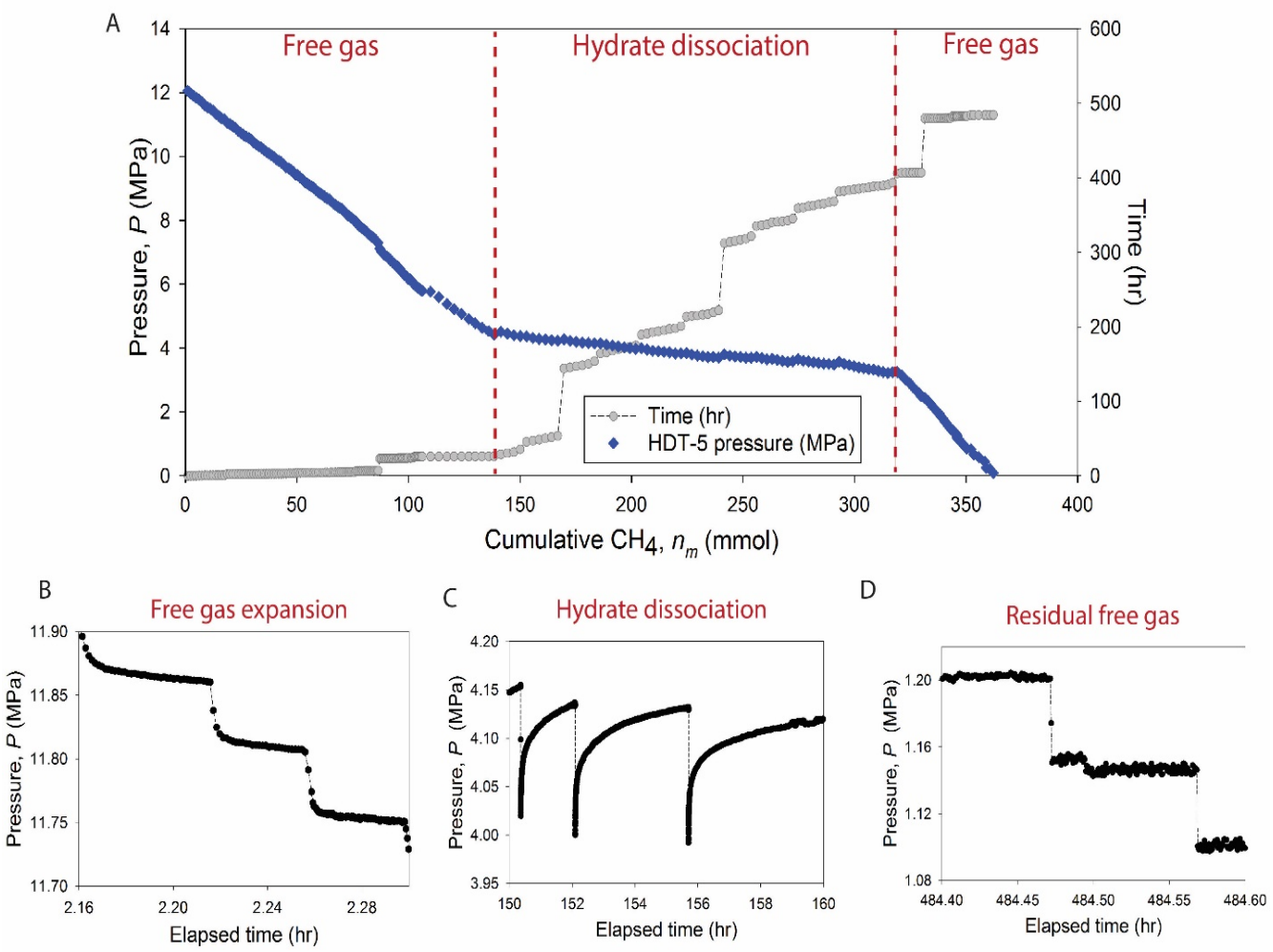

Figure 18. Three stages of depressurization: initial free gas release, hydrate dissociation, and residual free gas release. When hydrate dissociation occurs, there is a break in slope in the pressure vs. cumulative methane curve (A), and pressure rebounds occur (C). Free gas release results in a drop to a new stable pressure at each strep (B and D). From (Phillips et al., 2019)

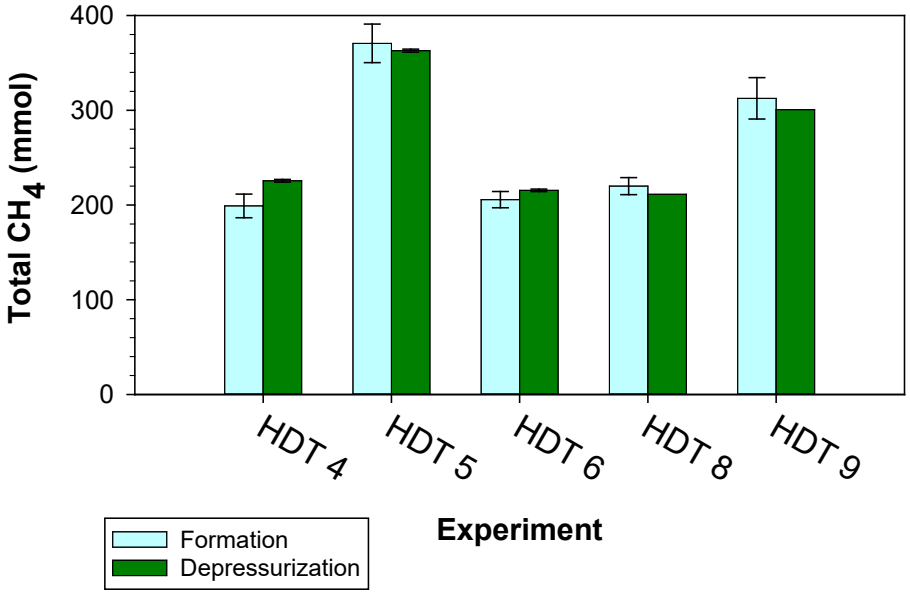

Figure 19. Mass balance of methane consumed during formation (light blue) and recovered during depressurization. The average difference is 6% and within the analytical uncertainty of our experimental setup.

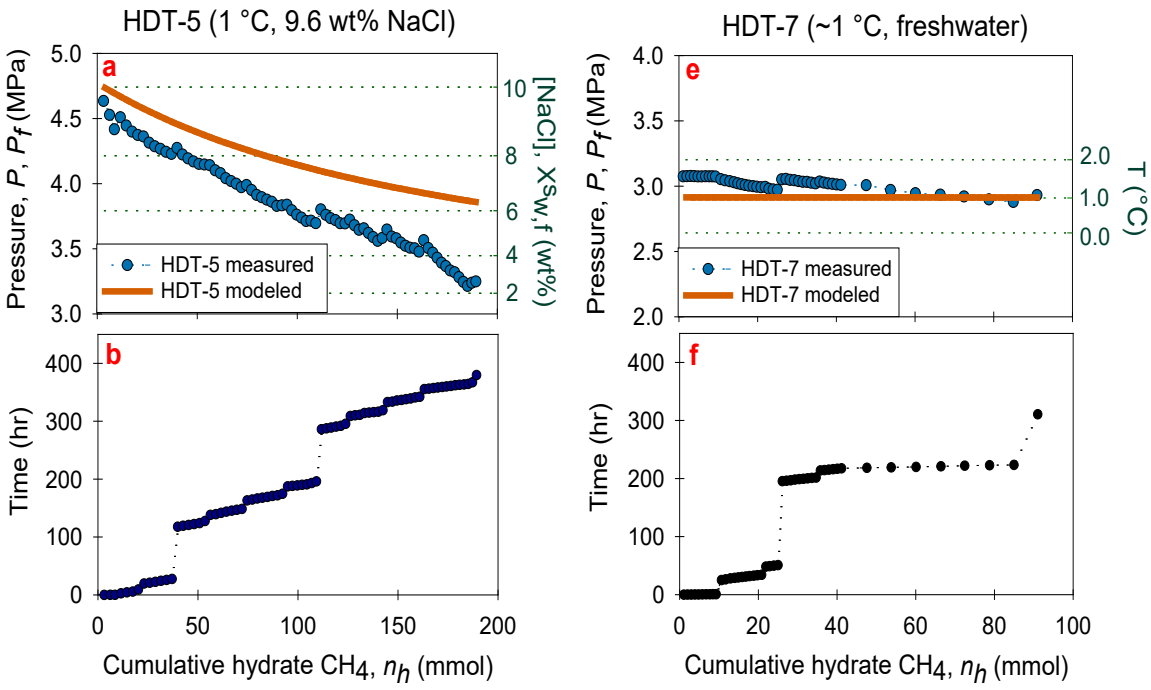

Figure 20. Results of slow depressurization compared to an equilibrium model based on homogenous salinity and temperature. The actual pressures, even with recovery of hours to days between each gas release step, decrease more rapidly than predicted, especially for a high salinity sample. Modified from (Phillips et al., 2019)

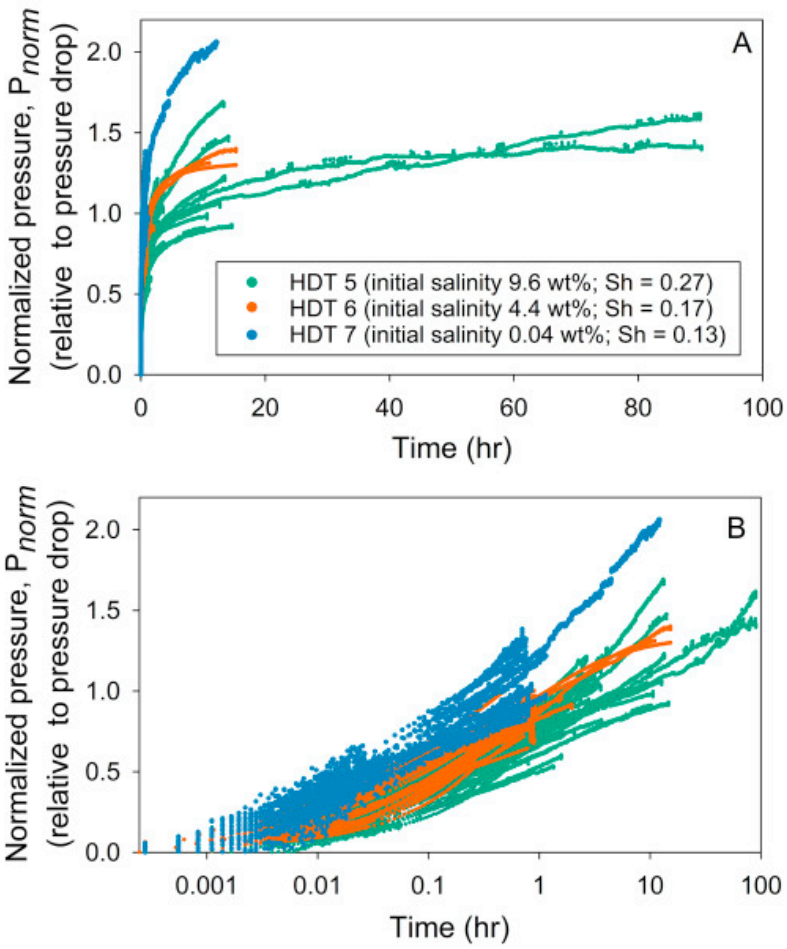

Figure 21. Pressure rebounds between each gas release step, normalized to the magnitude of initial pressure drop. Pressure rebounds shown on both a linear (A) and logarithmic (B) scale. Rebounds return towards bulk equilibrium conditions more rapidly in higher salinity experiments than in fresh water. From (Phillips et al., 2019)

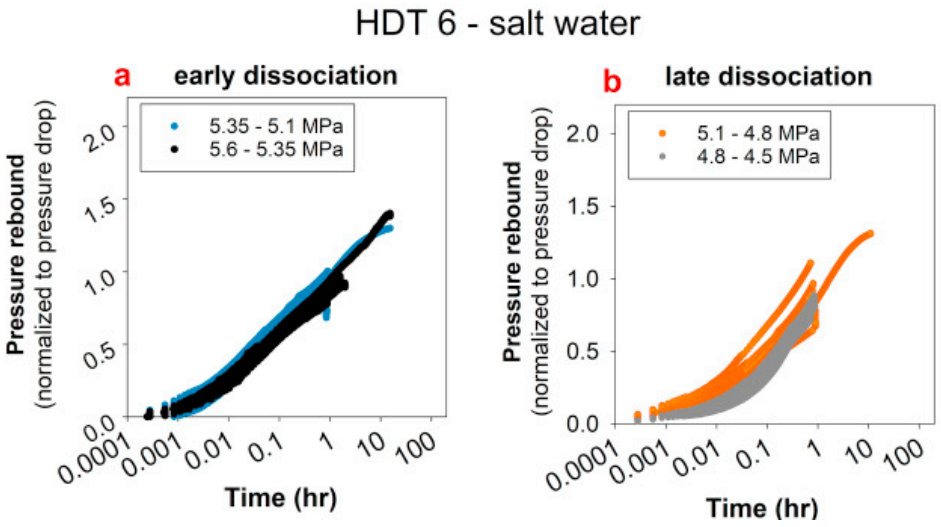

Figure 22. Pressure rebounds in early (a) and late (b) stages of dissociation. Modified from (Phillips et al., 2019)

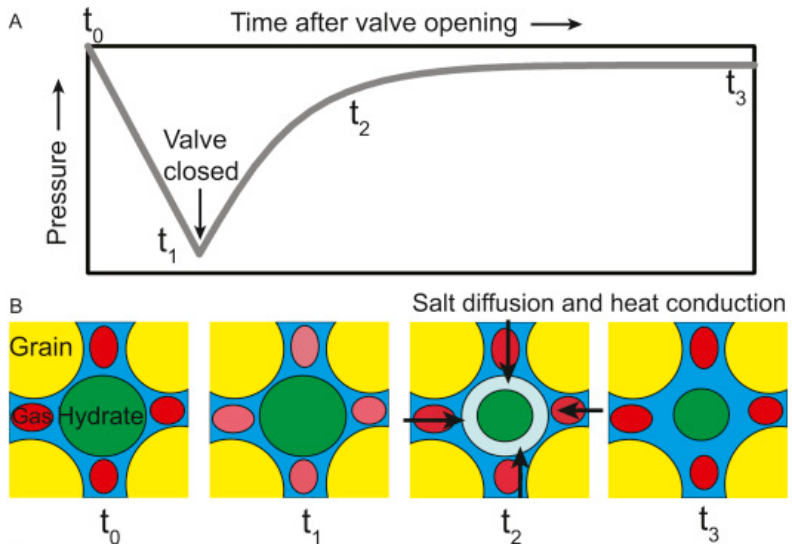

Figure 23. Conceptual model illustrating the role of freshening and cooling at the pore scale followed by increase in salinity and temperature during shut-in. a) Pressure rebound over time during shut-in period: t0 is the initial condition prior to pressure drop; t1 is the point in time at the minimum of the pressure drop just before dissociation begins; t2 is during the pressure rebound; and at t3 the sample has returned to bulk equilibrium. b) Methane hydrate and brine are present in the pore space prior to dissociation (t0 and t1); hydrate dissociation creates a cooled and low-salinity layer surrounding the hydrate (t2). During the shut-in period, salt diffuses towards the dissociation front as dissociation continues at a diminishing rate as the system returns to bulk equilibrium conditions (t3). Lighter blue colors indicate lower salinity. Lighter red colors indicate lower density of gas. From (Phillips et al., 2019)

4.4 Depressurization with CT Scanning

One experiment was formed and dissociated within a medical X-ray computed tomography (CT) scanner (Figure 24). The scans were collected as slices every 3 mm with a 0.23 mm pixel resolution using an X-ray tube energy of 130 kV and 100 Ma.

CT scans during pressure rebounds show a decrease in bulk density several cm into the sample and an increase in bulk density at the top of the sample (Figure 25). These results suggest the possibility of water movement and/or hydrate reformation during dissociation in these samples.

More information about all the depressurization experiments can be found in the Milestone Report 1.D in Appendix C

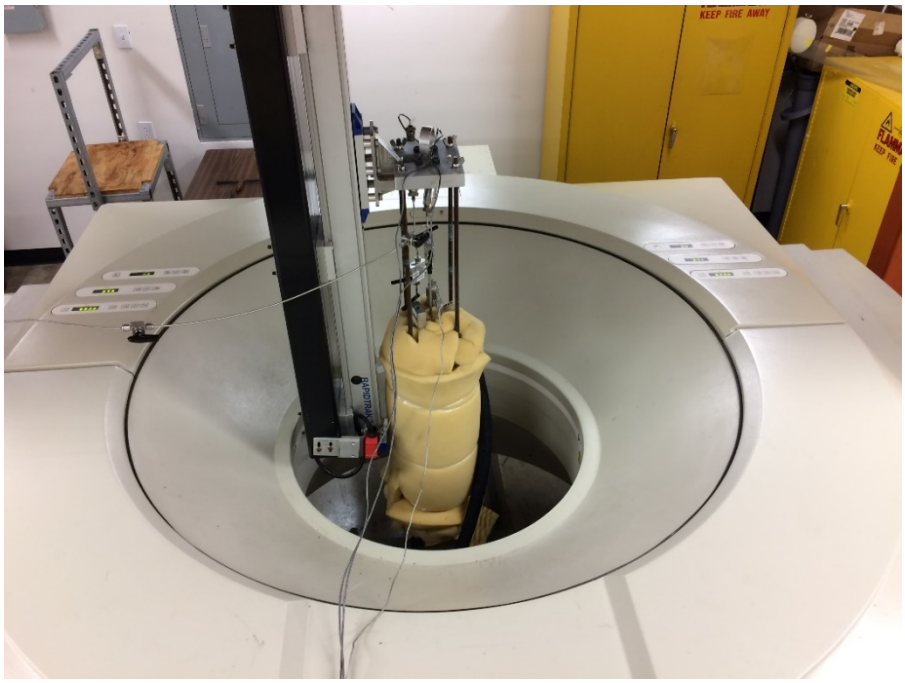

Figure 24. The hydrate vessel within the medical CT scanner.

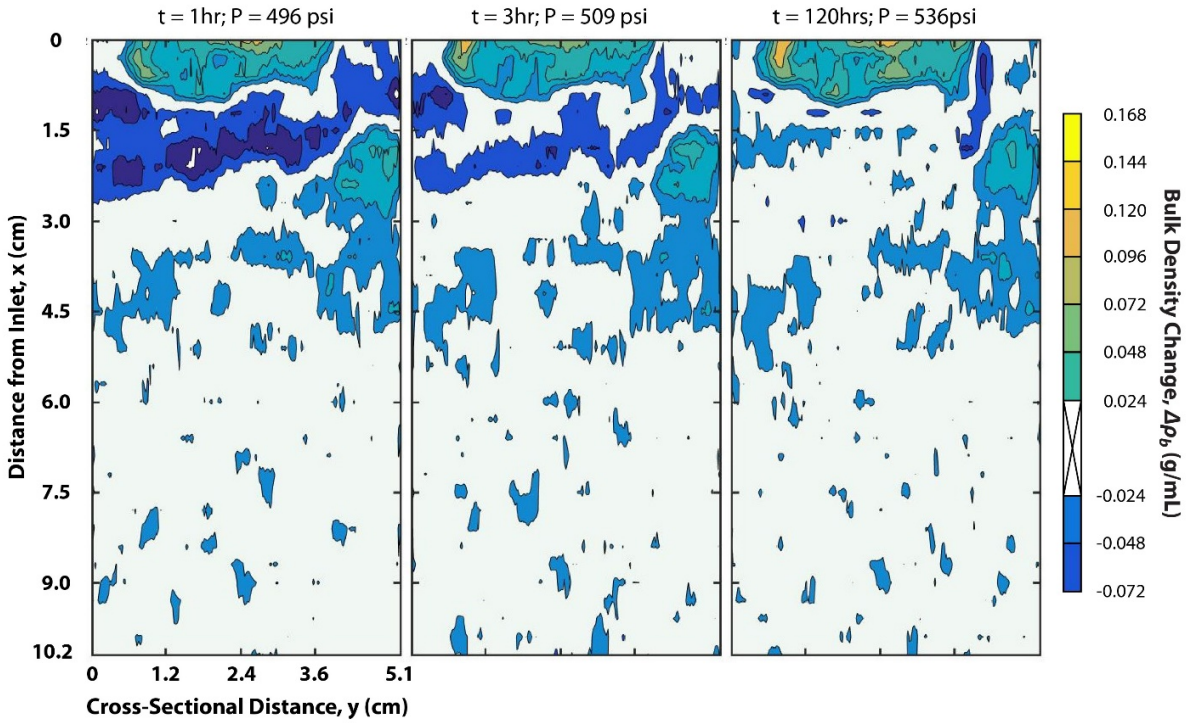

Figure 25. Changes in bulk density derived from CT-scanning at 1 hour, 3 hours, and 120 hours after a pressure drop and release of gas. Blue shades represent a decrease in bulk density and green-yellow shades represent an increase in bulk density.

4.5 Depressurization of natural hydrate-bearing sediments

We depressurized natural hydrate-bearing sediments from the Gulf of Mexico in a similar stepwise approach as our hydrates in synthetic sand packs. We recovered pressure cores from a reservoir 410-450 m below the seafoor in the northern Gulf of Mexico (Green Canyon 955). Analysis of these cores revealed interbedded sandy silt (> 80% hydrate saturation, high-P-wave velocity) and clayey silt (< 30% hydrate saturation, low P-wave velocity) (Flemings et al., 2018; Meazell et al., in review; Phillips et al., accepted). We dissociated examples of both lithofacies within the reservoir. During depressurization we characterized the volume and composition of gases accumulated in a bubbling chamber at each step (Figure 26). We measured the pressure and temperature within the core storage chamber with a data storage tag (Star Oddi) within a spacer at the top of the core sample. From these sets of measurements, we can observe a time-series of pressure and temperature within the sample and the cumulative methane released (Figure 27). Once hydrate dissociation begins we observe pressure rebounds as gas continues evolved from the sample. By measuring the pressure and temperature in the sample just before the rebound (hydrates still stable) and when the first pressure rebound begins to level off (minimal hydrate dissociation), we can calculate the salinity of the phase boundary of methane hydrate at these points to bracket the in situ pore water salinity (Figure 28). In all samples that we estimated salinity with this approach, the estimated salinity ranges overlap with the average salinity of seawater (35 parts per thousand) (Figure 29).

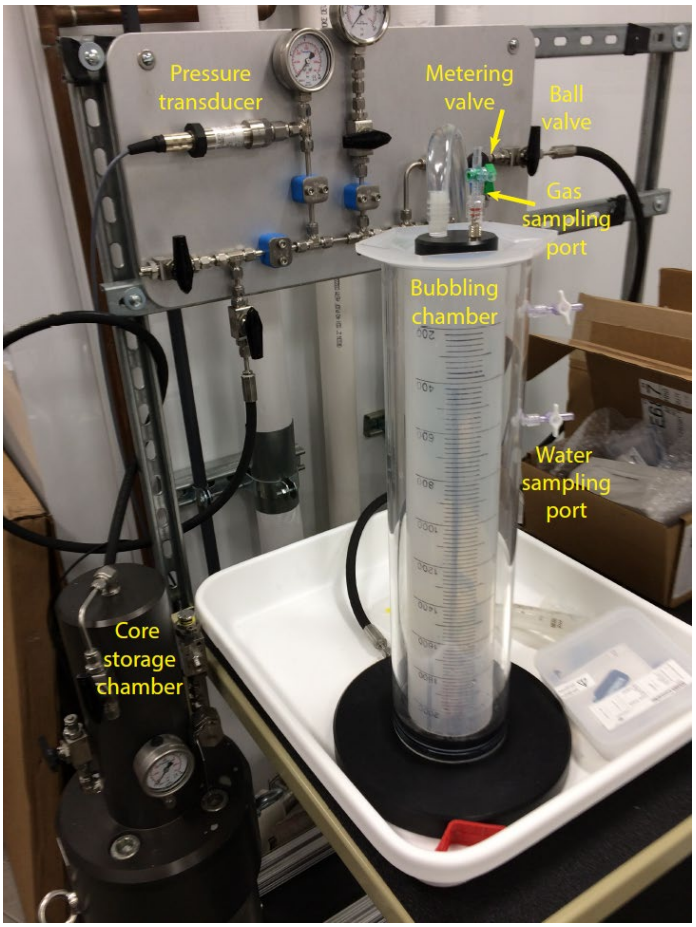

Figure 26. Depressurization apparatus for pressure core samples. From (Phillips et al., accepted)

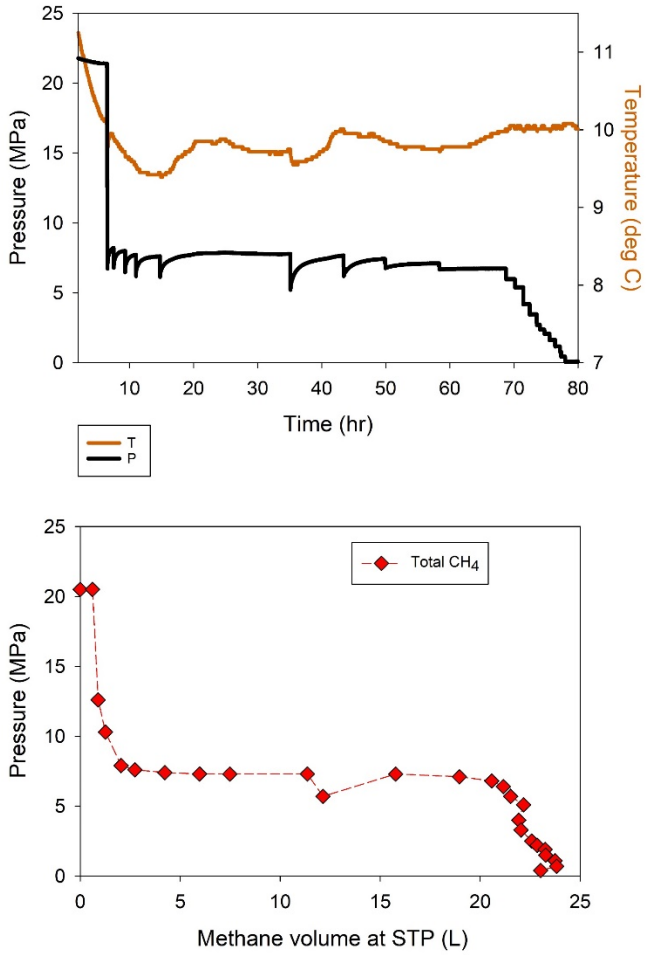

Figure 27. Example results from a quantitative degassing experiment from core H002-04CS. Top: pressure and temperature within the core storage chamber during the course of depressurization. Bottom: Pressure versus volume of methane released.

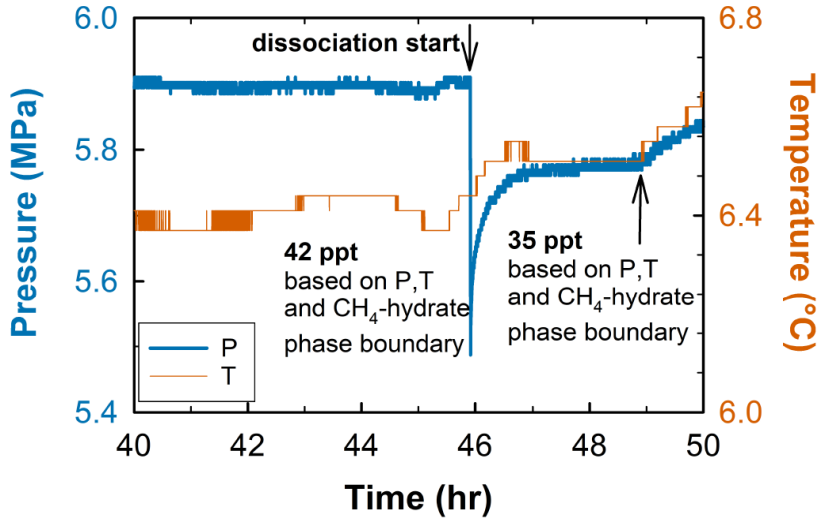

Figure 28. Detailed pressure (blue line) and temperature (red line) response at the start of hydrate dissociation. Not the distinct pressure rebound behavior after the sample pressure drops outside of the hydrate stability field. From (Phillips et al., accepted)

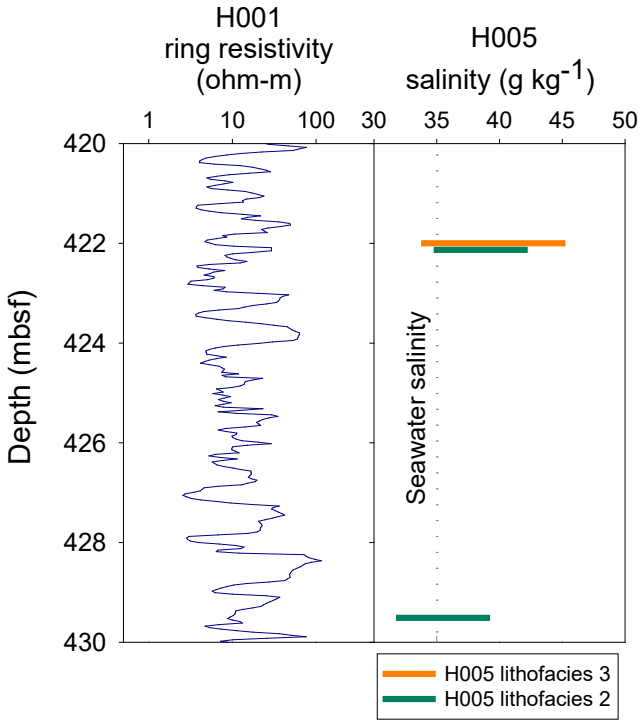

Figure 29. Estimated salinity of pressure core samples from Green Canyon 955 in the northern Gulf of Mexico. Salinity ranges overlap with the average concentration of seawater. Modified from (Phillips et al., accepted)

We observe a deviation of the pressure versus methane released where after hydrate dissociation the observed pressure is lower than that predicted by bulk equilibrium. In an example of core H002-04CS-1, a dissociation that occurred over 2 days, the pressure drops to near the freshwater phase boundary (Figure 30). Overall, this is similar to the behavior we observe in the synthetic samples. The deviation from bulk equilibrium is accompanied by pressure rebounds that evolve over the course of dissociation (Figure 31). These rebounds are similar in shape to those observed in the synthetic experiments with a more pronounced shift to concave-up in shape (versus log time) in the natural samples. The placement of data storage tags adjacent in the sample allow us to look at these pressure rebounds in pressure-temperature space (Figure 32). We see sustained cooling in the sample for several hours after the valve is opened and closed, followed by warming. During these warming trends, the slope of the P-T path is gradually approaching higher salinity phase boundaries, suggesting that salt diffusion occurs on the time scale of days during a pressure rebound.

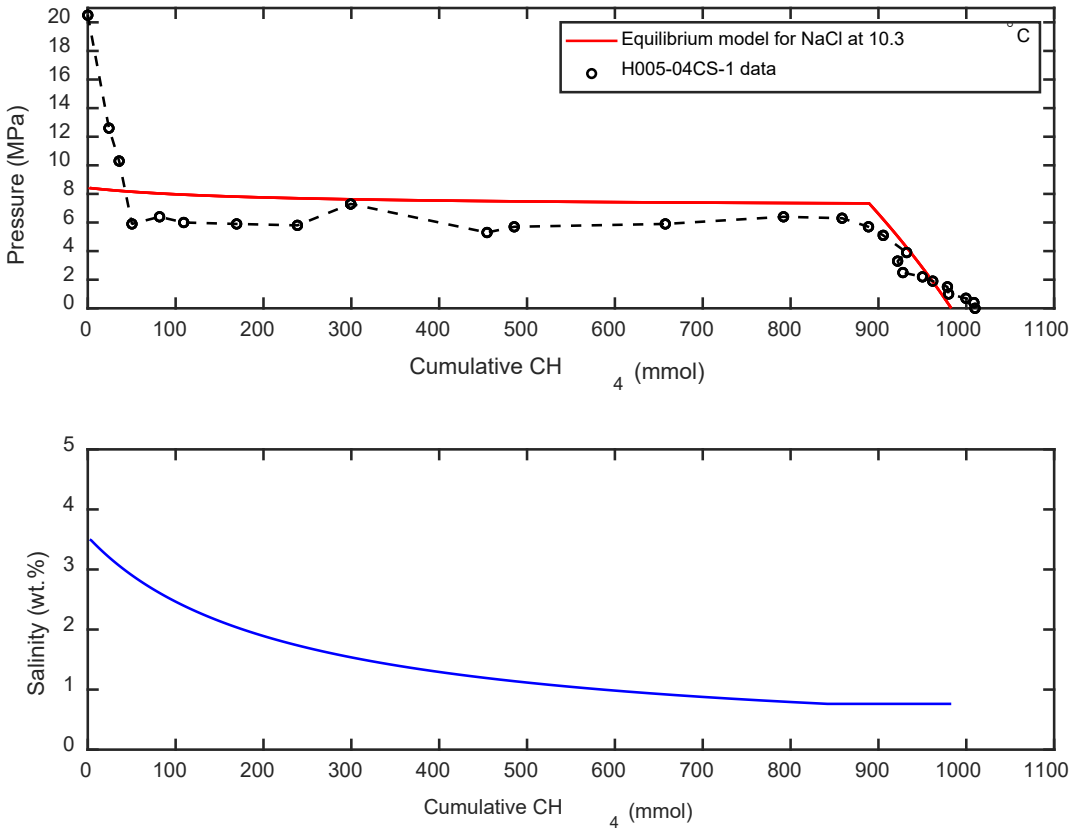

Figure 30. Top: pressure versus cumulative methane for sample H002-04CS-1 compared to the pressure decline predicted for bulk equilibrium conditions. Bottom: Predicted salinity decline during hydrate dissociation.

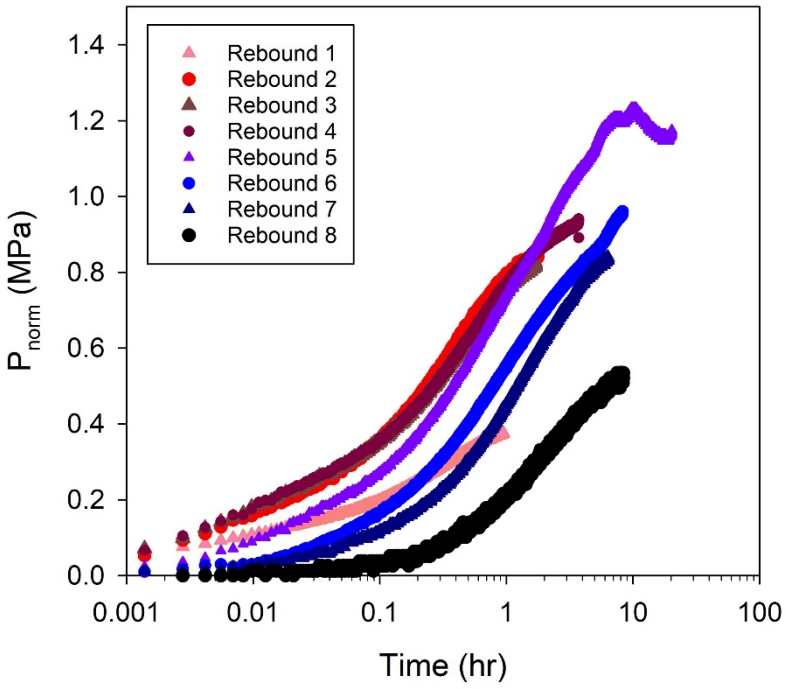

Figure 31. Pressure rebounds during hydrate dissociation in sample H002-04CS-1.

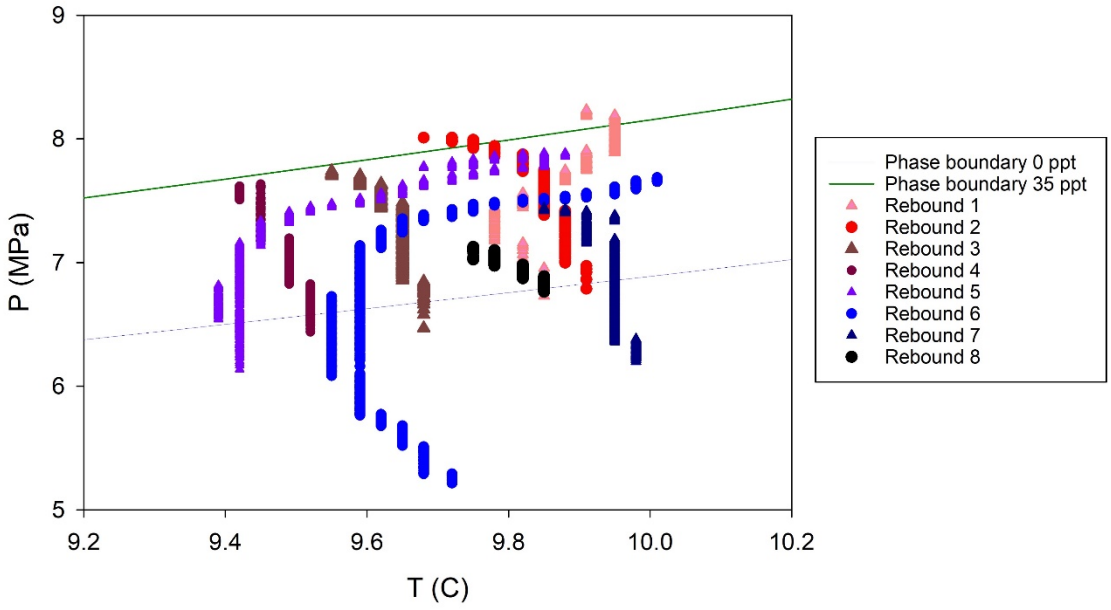

Figure 32. Pressure rebounds plotted as pressure versus temperature for sample H005-04CS-1.

5.0 Micro-Scale: CT Observation of Methane Hydrate Sand Packs

5.1 Micro-CT Summary

We have successfully built and tested a micro-consolidation device for forming and imaging gas hydrate in sediments and successfully used that device to create and image methane hydrate. The following results summarize our achievement of monitoring gas hydrate formation and dissociation through micro-computed X-ray tomography (micro-CT). The grains of GC 955 natural samples were too small to observe the pore space and monitor produced gas. For this reason, we concentrated our micro-CT efforts on coarse sediments in which we can distinguish CH_4 hydrate clearly. The experiments show coexistence of gas, brine and hydrate at the pore-scale and their evolution of hydrate pore-habit towards three-phase equilibrium. The experiments and data analysis reveal that (1) hydrate forms as a porous medium mixed with inclusions of brine and gas, where hydrate and brine evolve gradually into separate phases as hydrate cages exclude salt ions, (2) hydrate growth mobilizes water over fairly long distances resulting in heterogeneous hydrate distribution, and (3) hydrate can exhibit interconnected pore-habit at local hydrate saturations higher than ~50%, even if grown under excess-gas condition. The results show that hydrate preferentially dissociates at the boundaries of hydrate lumps. Inner hydrate may remain stable in large hydrate lumps.

5.2 Building and Testing the Micro-CT Device

Figure 33 shows a schematic of the device and experimental workflow. The micro consolidation device consists of a hard-walled pressure vessel semi-transparent to X-rays that permits applying a constant vertical effective stress to the sediment. The vessel is small enough to obtain high scanning magnification and observe hydrate pore habit. The vessel accounts with a permeable endcap for fluid injection. The vessel was machined from aluminum and resists a working pressure up to 13.79 MPa (2,000 psi). The micro-consolidation device and has a (internal) dimensions of 0.79-cm-diameter and 3.1-cm-length. A spring applies an effective stress to the sand pack. The two sieves prevent sand going into the spacers. The sample vessel has one end connected to a constant-volume methane gas accumulator (volume 5.84 cm^3). The other end is closed. The total free volume of the pressure vessel including piping is 1.64 cm^3 (excludes gas accumulator). Two negative-temperature-coefficient thermistors attached to the top and bottom of the sample vessel measure temperature and communicate to a microcontroller-based electronic board (Arduino). The electronic board uses a proportional-integral-derivative algorithm to control two Peltier cooling assemblies for maintaining the target temperature in the sample vessel.

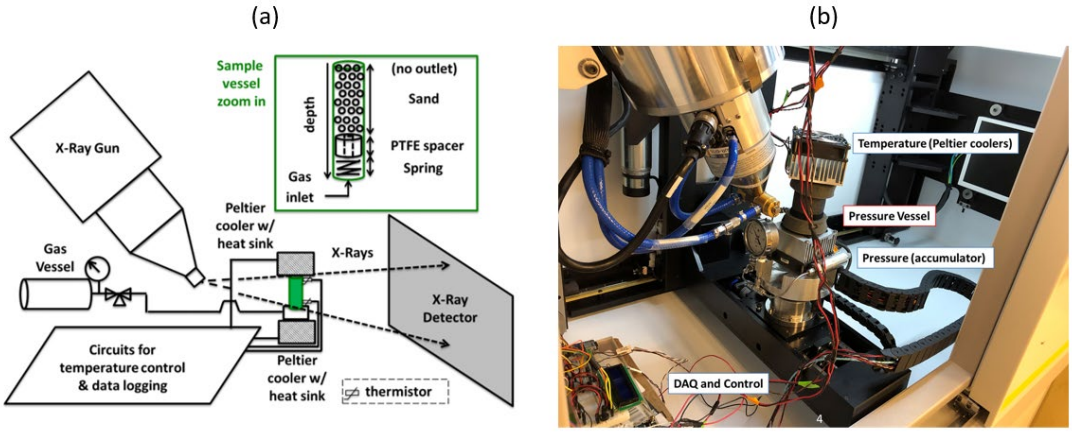

Figure 33. micro-consolidation device (a) Schematic of micro-consolidation device monitored by X-rays. (b) Actual device built in this project.

5.3 Hydrate Formation Method (Micro-CT)

We used NaBr brine and KI brine as the aqueous phase instead of using NaCl brine in methane hydrate experiments. X-ray contrast between methane hydrate and NaCl brine is low. We used both excess-gas and excess-water methods. We did excess-gas formation experiments by packing sand and brine at near residual water saturation and then pressurizing the system with methane gas and cooling it to take it to the hydrate stability zone (we also tried cooling first and then pressurization). Second, we did excess-water experiments by saturating the sandpack with methane gas at ~0.69 MPa (100 psi), pressurizing the pore space (and methane gas) by injecting brine at high pressure, and finally cooling the system to take it to the hydrate stability zone. Figure 34 shows a pressure-temperature paths for the KI-brine experiments conducted under excess-gas condition together with hydrate stability boundaries for different salinities. We conducted experiments with coarse Ottawa sand (median grain size d_{50} ≈ 700 µm) and medium sand (d=210-250 µm). Excess-gas for saline systems means that there is sufficient methane for all the available brine to form hydrate to the stable three-phase hydrate-brine-gas state. In contrast, excess-gas conditions for pure water means that all water converts to hydrate.

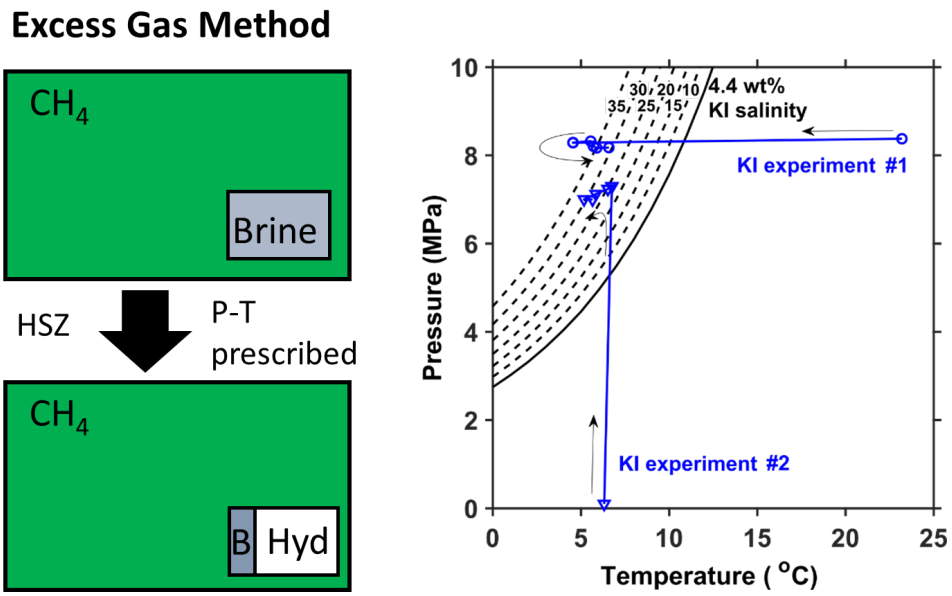

Figure 34. Experimental pressure-temperature path for two KI-brine experiments under excess CH_4 gas conditions.

5.4 X-ray Image Segmentation Procedure

We monitored hydrate experiments with a Nikon XTH-225 X-ray microtomograph. Each computed tomography (CT) scan completes in 25 minutes and is a reconstruction of 2,984 projections. The detector captures 16-bit grayscale CT numbers (0 to 65,535). The resolution of the experiments varies from 4 to 15 µm/voxel. Image analysis, segmentation, and calibration permit obtaining phase saturations brine salinity, and hydrate porosity from CT images. Most CT images in this study contain four phases which are bulk brine, sand grain, methane hydrate-rich phase and methane gas. The image analysis process consists of four steps.

First, all images are normalized to have mean CT numbers of sand and methane adjusted to constant values: CT_{sand} = 23,500 and CT_{gas} = 5,000. Second, we use ImageJ software to threshold images and divide the four phases into two groups. The high CT number group consists of the bulk brine phase and the sand grain phase. The low CT number group consists of the methane hydrate-rich phase and the methane gas phase. Third, we perform a second segmentation in each group. The process of segmentation and additional calculations result in: (a) sand phase used to calculate porosity φ, (b) bulk brine saturation S_w, (c) hydrate-rich phase saturation S_h^*, and (d) gas phase saturation S_g. Fourth, the variability of the CT number of bulk brine and the hydrate rich-phase is a function of volume fractions of salt and methane gas at sizes non-distinguishable at the scanning resolution.

5.5 Micro-Scale CT Observations and Analysis

5.5.1 Hydrate Formation in Coarse Sand

Figure 35 shows an excess-gas experiment that started at a water saturation of $S_{w,i}$ = 30.0% (measured through CT volume segmentation) by packing the sand at a target saturation. No extra brine is added after

this point. The CT images show a well-defined brine phase preferentially located near particle contacts at 0 day. An accumulator provides methane gas at near constant pressure. Methane comes from the bottom of the sample. Methane hydrate formation was substantial in the two experiments after 2 days within the hydrate stability zone. The hydrate-rich phase is identified by its lower X-ray attenuation relative to that of the initial brine. After 13 days, most hydrate accumulates on the top section of the sand pack with more than 50% of hydrate in the top third. The final bulk saturation of the hydrate-rich phase is S_h^* = 32.2 % (the symbol * indicates hydrate-rich phase including non-segmentable brine inclusions) and the final brine saturation is S_w = 2.9%. Surprisingly, hydrate saturation is far from being homogeneous and changes drastically over short distances.

Toward the end of the experiment, residual brine with X^S_w > 13 wt% KI remains near a number of grain contacts throughout the sandpack. The increase of brine salinity with respect to the initial condition is a result of conversion of water molecules to methane hydrate cages and ion exclusion. Brine salinity reaches a value up to X^S_w ~ 35 wt% KI with a mode at 14 wt% after 13 days.

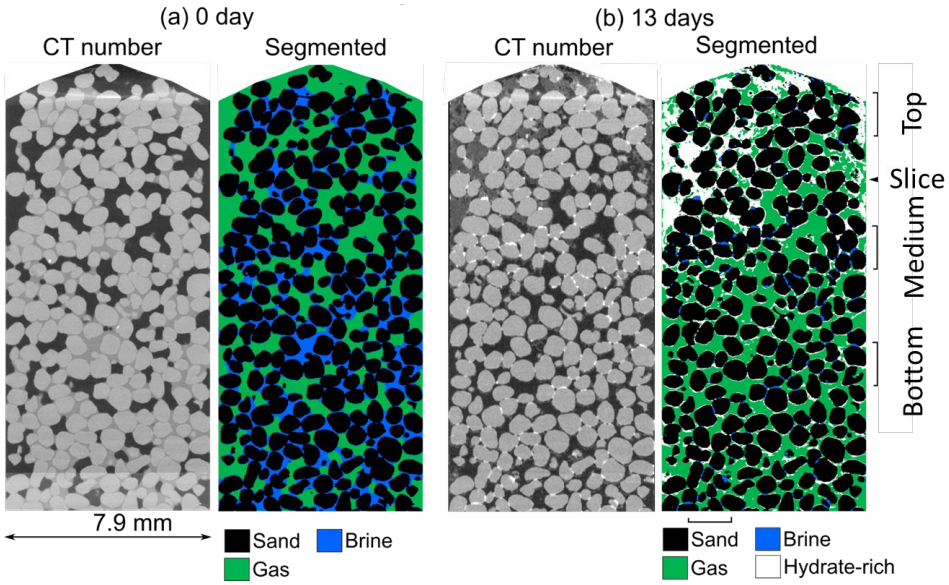

Figure 35. Axial CT slices of KI-brine experiment. (a) Images out of hydrate stability zone at 0 day. Sand is partially saturated with brine and methane. (b) Images at 13 days within stability zone. Hydrate-rich phase (pixels with bulk salinity < 6 wt%) accumulates at the top of the vessel leaving of high salinity residual brine (bulk salinity > 13 wt%).

The pore habit is pore-filling and pore-interconnecting (i.e., surrounding grains and percolating the pore structure) towards the top of the vessel, and dispersed and grain-attaching towards the bottom of the vessel (Figure 36). The 3D renders show that hydrate appears both where brine was originally present and where brine was absent (e.g., top-front corner), and that local hydrate saturation (after 13 days) can greatly exceed the initial bulk brine saturation in the aggregation zones.

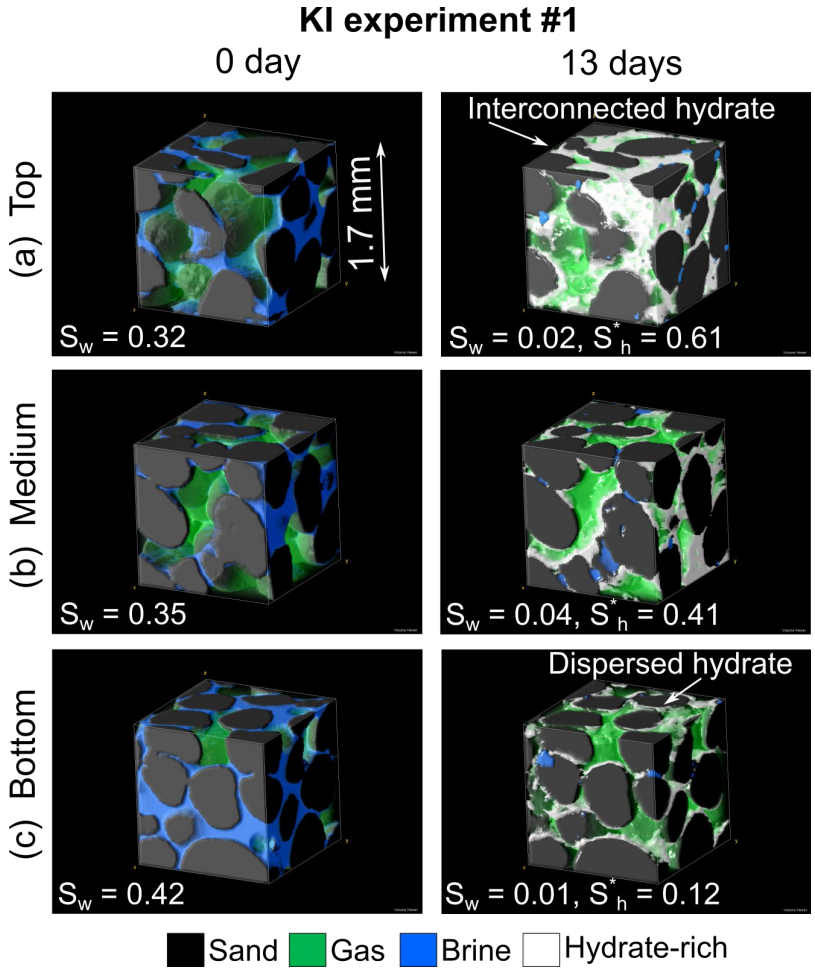

Figure 36. 3D renders of selected regions of the segmented volume for the KI experiment shown in Figure 37. Hydrate is interconnected towards the top of the vessel (a) and dispersed and grain-attaching in the lower half of the vessel (b). Concentrated brine is mostly at grain contacts (b, c). S_h^* is the saturation of the hydrate-rich phase including non-segmentable brine within porous hydrate. The gas phase (green) has a 10% opacity for illustration purposes.

5.5.2 Hydrate Formation in Sandy Silt from GOM^2

Sample preparation consists of: 1) mixing the GC 955 sediment sample with 4.37 wt% KI brine before packing, 2) packing the damp sediments in a micro-consolidation device (3.6 mm-diameter and 10 mm-long), and 3) taking the sample into the hydrate stability zone under excess gas conditions. The damp-sand packing method results in large pores unlikely to be present in natural sediments. The initial step consists in increasing methane gas pressure to 8.14 MPa at room temperature (23.0°C). Then, we decrease the temperature to 2.7°C, within the hydrate stability zone.

Figure 37 shows micro-CT slices of the sediment before and after 8 days into the hydrate stability zone. Outside the stability zone methane gas occupies pores (black) with different sizes in the image outside the stability zone. For instance, the large white box (400 µm) shows a large pore about 400 µm by 60 µm, and the small white box (150 µm) shows pores sized about 20 µm. These large pores are a result of the

damp-sand packing procedure. Smaller pores are saturated with brine. It is difficult to differentiate between brine and grains due to their similar CT numbers and the small grain size. The histograms of selected boxes show two distinct peaks for methane gas and the combination of sand and brine.

After 8 days within the hydrate stability zone: many of the previously gas-filled pores exhibit methane hydrate growth. For example, the CT numbers in the large pores within the selected boxes increase after 8 days within the stability zone. This change indicates the existence of methane hydrates within these large pores. Although we present evidence of hydrate formation in relatively large pores >20 µm. These pores are the result of the damp-sand packing method and unlikely to be present in natural sediments. The current apparatus and technique do not permit segmenting hydrate in the pore space of natural Sandy silt, previously called Lithofacies 2. As a result of this limitation and upon approval from the project manager, we stopped testing GC 955 sandy silt.

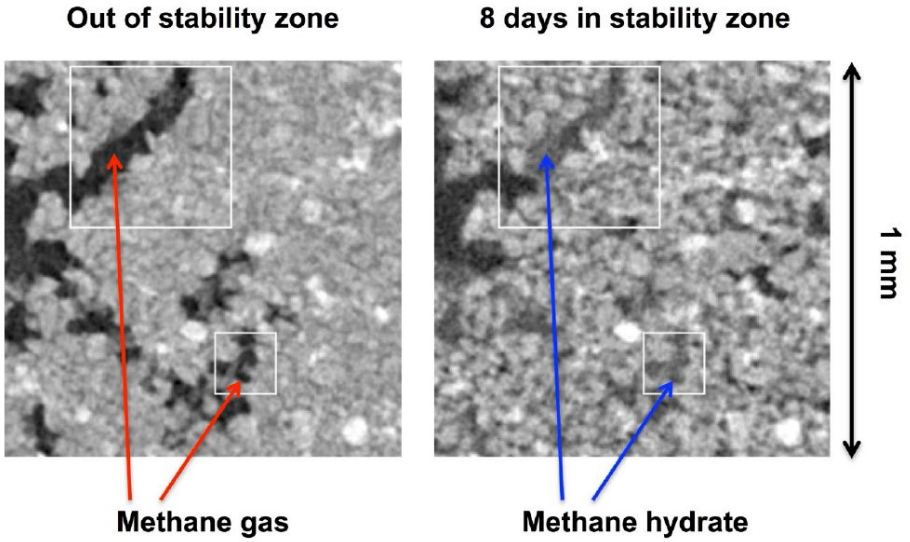

Figure 37. Micro-CT images of loosely packed UT-GOM2-1 GC 955 sediments out of the hydrate stability zone (left) and after 8 days within the CH_4 hydrate stability zone at a resolution of 4.5 µm. CT images identify hydrate only in large pores.

5.5.3 Hydrate Formation in Bimodal Sand Pack

Figure 38 shows an example of sand pack with bimodal distribution. The objective of this kind of experiments was to observe directly the implications of having two different types of pore sizes on hydrate formation, pore habit, and dissociation. The results show that hydrate forms preferentially at gas-brine interfaces. The gas phase "disappears" as gas is consumed and forms hydrate. Eventually, gas hydrate remains as nodules filling up the pore bodies of the sand pack. We do not observe consistent "grain-coating" or "grain attaching" hydrate, even at low hydrate saturations. All observed hydrate is “pore-filling”.

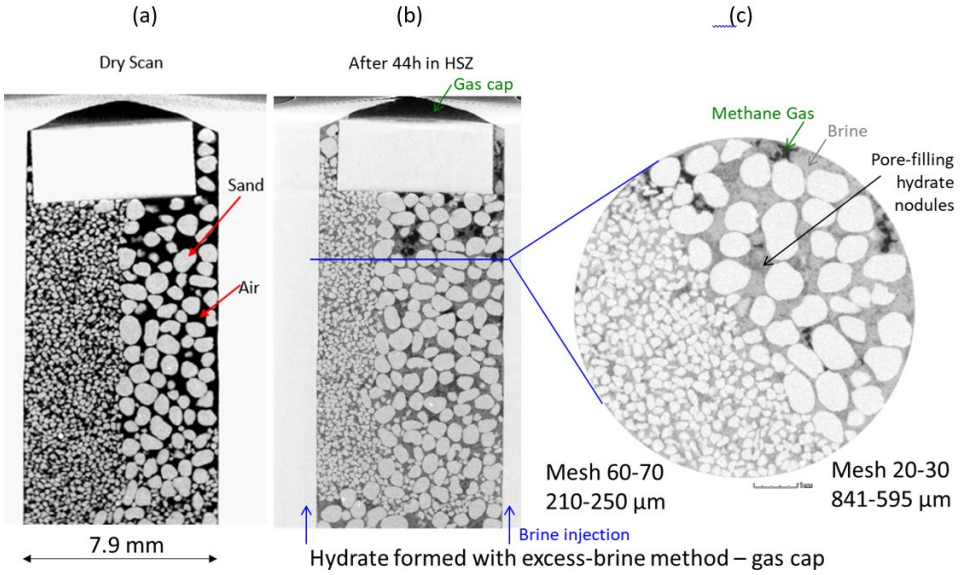

Figure 38. Example of hydrate formation under excess-water condition. (a) Dry scan of sandpack with bimodal grain size distribution. (b) Scan after 44 hours within the hydrate stability zone. Water is injected from the bottom and forms a gas cap on the top of the vessel. (c) Radial slice showing simultaneous presence of gas, brine, and CH_4 hydrate.

5.5.4 Hydrate Dissociation

Figure 39 shows an experiment that follows a slow depressurization pressure-temperature path from 8.2 MPa and 6.8°C gradually to 4.3 MPa and 6.2°C over 5 days. The difference between images at 0 and 1 days is negligible. Initially, CH_4 hydrate is stable and exhibits a pore-filling or pore-interconnected habit. Hydrate is porous with pores mostly filled by CH_4 gas. A few pores within hydrate and adjacent pore space is filled with high salinity brine. The increase of salinity is due to ion exclusion during hydrate formation. The dissociation of the section with low hydrate saturation is straightforward. Hydrate dissociates quickly leaving water at grain contacts and releasing gas into the pore space. The case with high hydrate saturation exhibits a different and more complex behavior during dissociation. Hydrate preferentially dissociates at the boundaries of hydrate lumps. Inner hydrate may remain stable in large hydrate lumps. Over 3 days of dissociation, we also observe new hydrate formed where it was not present at day 0. This new hydrate is likely the result of the endothermic reaction during dissociation and the availability of relatively fresh water from dissociated hydrate. The fraction of pore space available to gas flow is notably small.

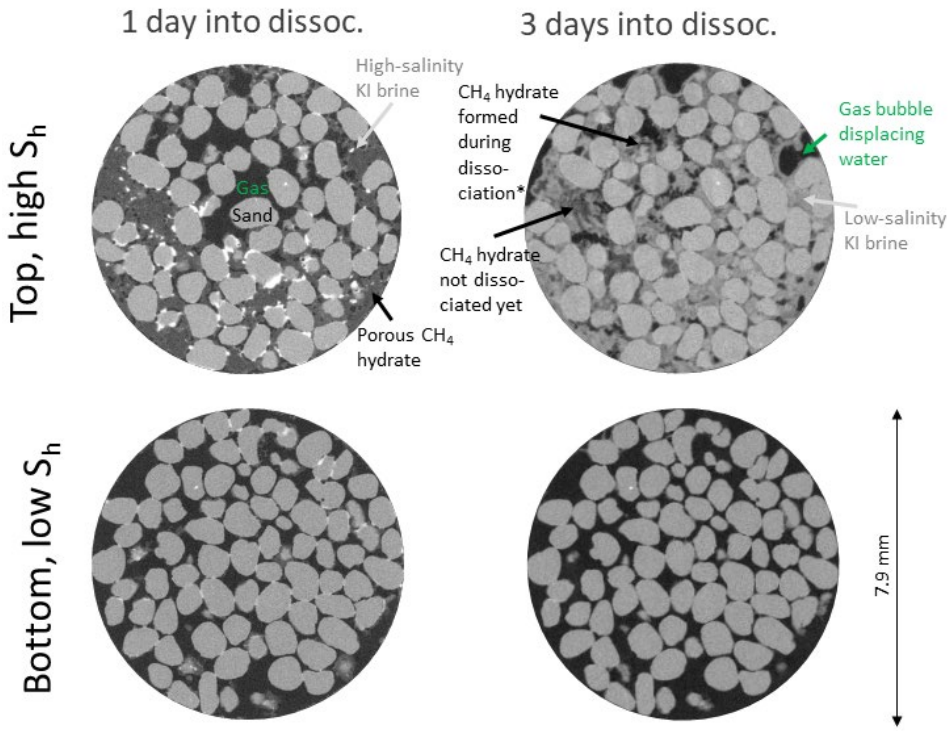

Figure 39. Radial slices of micro-consolidation vessel filled with sand during hydrate dissociation under excess gas conditions. The images show that radically different scenarios occur depending on hydrate saturation. High hydrate saturation leads to complex water-gas-hydrate interactions.

6.0 Micro-Scale: Raman Observation of Methane-Gas-Water Systems

6.1 Micro-Raman Summary

This section summarizes our achievement of building and integrating the high-pressure gas mixing chamber including the chamber design, data acquisition system, and testing of the device. It also summarizes our achievement of Micro-Raman analysis of synthetic complex methane hydrate during formation and dissociation in porous media of both glass beads and a mixed layer of natural GC 955 sandy silt and laboratory clay-free sand. We observed that the chemistry and the pore habit of methane hydrates change dramatically over the timescales of experiments (hours to weeks). It takes weeks to months for hydrates to evolve from a non-stoichiometric to stoichiometric compound with 3:1 large cage vs small cage occupancy and we documented hydrates forming initially in small clayey silt surfaces but gradually concentrated in large pores in sand-sized sediment. During dissociation, we observe at the pore scale that hydrate dissociation starts at the boundaries of hydrate clumps and proceeds inwards. This is similar to our observations with micro-CT. At a larger scale, we observe that hydrate starts to dissociate at a single point and then a hydrate dissociation front expands radially from this point.

6.2 Hydrate Formation (Micro-Raman)

6.2.1 Designing and Building a Micro-Raman compatible Pressure Vessel

A Raman chamber for hydrate formation and dissociation experiments was developed. The Raman chamber consists of two main parts: the sapphire window and the stainless steel seat. The optically clear sapphire window allows us to conduct *in situ* optical imaging and Raman spectroscopy during hydrate formation and dissociation experiments. The sapphire window and the seat screw together, sealed by an O-ring. Figure 40 shows the entire apparatus in action. The Raman chamber is placed under the Raman spectrometer. The chamber is connected to the syringe pump through a flexible tubing. Figure 41 right shows the schematic diagram of the Raman chamber, tubing, and the syringe pump.

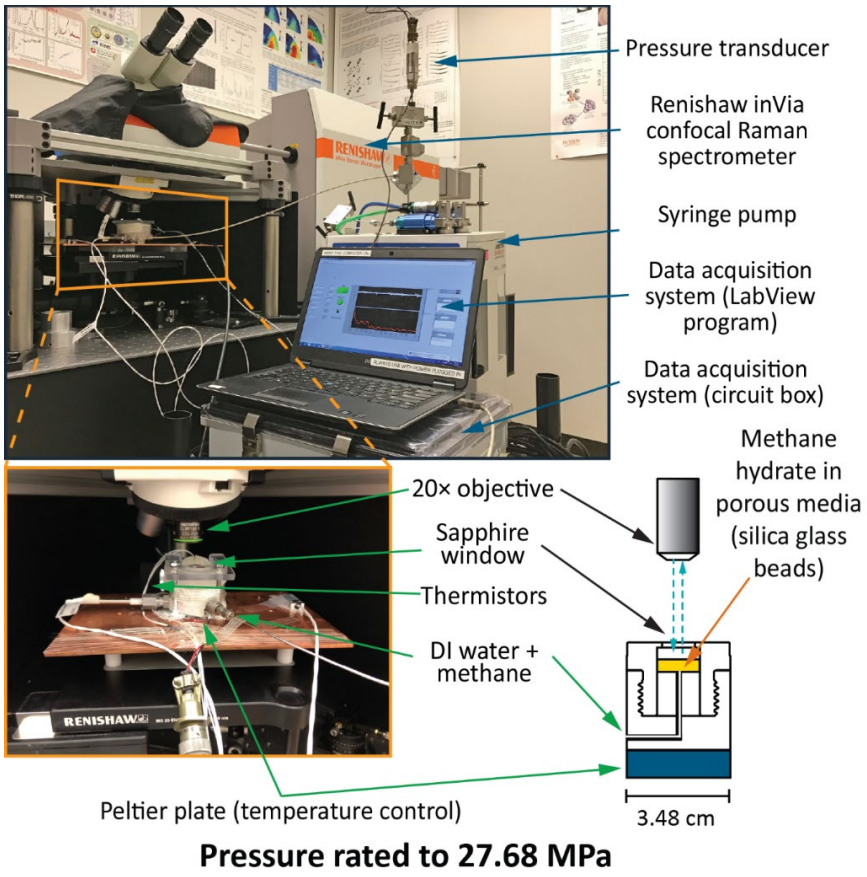

Figure 40. Raman chamber under the Raman spectrometer in the Mineral Physics Lab, UT-Austin. The chamber is pressure rated to 27.68 MPa.

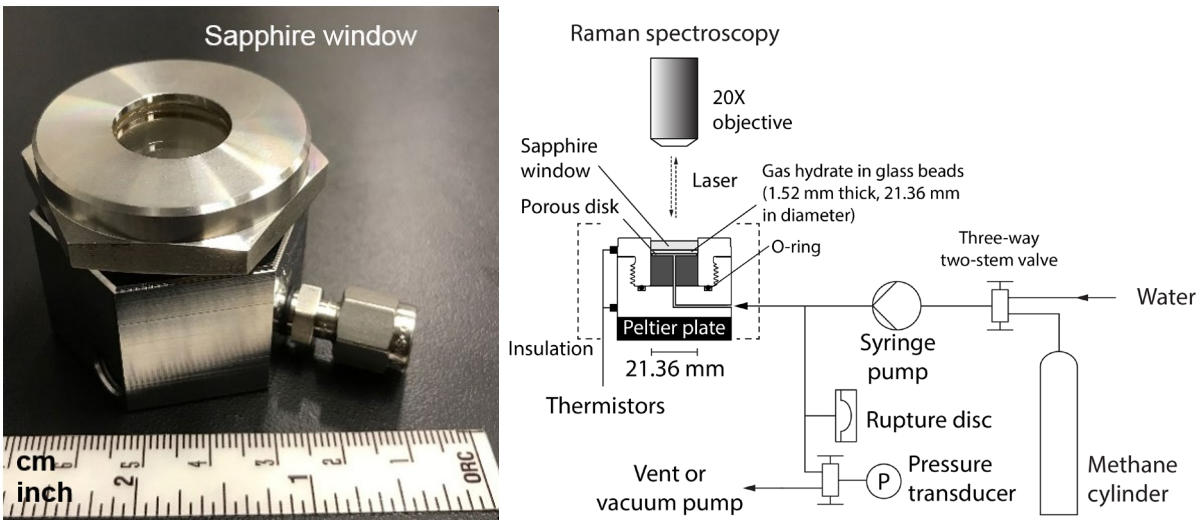

Figure 41. Micro-Raman chamber. Left image of the vessel. Right schematic diagram of the Raman setup.

We have also built a data acquisition system for pressure and temperature logging and Peltier plate control for cooling capacity. Figure 42 shows the schematic diagram of the electronic circuit and a photograph of the box that contains the data acquisition system.

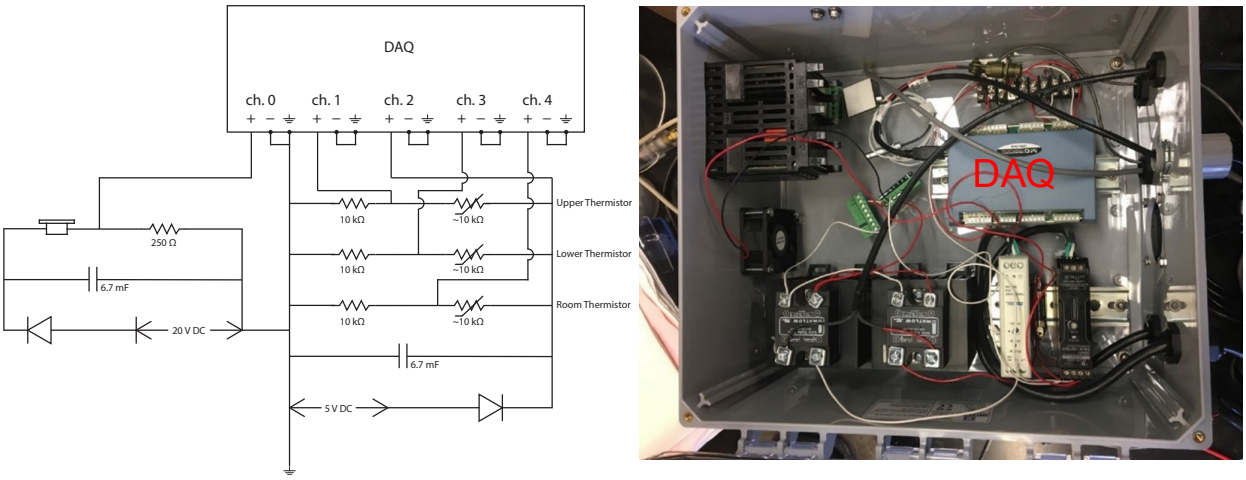

Figure 42. Schematic circuit diagram and photograph of micro-Raman data acquisition system. The system records one pressure sensor and three temperature sensors.

The Raman Chamber has been successfully pressure tested with water and CH_4 up to 24.24 MPa (3500 psig) and down to 1 °C. We use a syringe pump and a Peltier plate to control pressure and temperature, respectively. We have conducted experiments at conditions of 3.45 -24.13 MPa (500 psig – 3500 psig), 1 °C to 22 °C to simulate natural hydrate reservoir conditions. More information about the design, testing and data acquisition can be found in Milestone 1.G Report in the Phase 1 report, Appendix F.

Data from the Raman system was using to create 2D maps with resolution of 25 µm (meaning each Raman data acquisition location was 25 µm apart, unless indicated as otherwise, in both X and Y directions). Thus, over a 2 mm by 2 mm area, we acquired 6561 (81 by 81) acquisition points for each map.

6.2.2 Hydrate Formation Method 1. Glass Beads (Micro-Raman)

Methane hydrate was synthesized using an “excess water” technique. The glass beads were initially filled with methane vapor. Water was then supplied to compress the methane vapor and elevate the pressure to hydrate stability zone (15 MPa and 3 °C). We monitored the hydrate formation with optical imaging and micro-Raman spectroscopy. In addition to hydrate formation, we dissociated the methane hydrate by slowly decreasing the pressure.

We characterized the formation and dissociation stages of hydrate using micro-Raman spectroscopy and optical imaging. Initial experiments were conducted with 210-290 µm diameter beads and repeated with 160 – 210 µm diameter beads. We utilized the advantages of high spatial and spectral resolution of the Renishaw inVia Raman spectrometer in the Mineral Physics Lab at the University of Texas at Austin. The spatial resolution of the Raman spectrometer is below 1 µm on a dry sample. However, in our Raman Chamber, the spatial resolution was limited to 3 – 5 µm, as the sample contained liquid water and was probed through a sapphire viewing window of 4 mm in thickness.

6.2.3 Hydrate Formation Method 2. Layers of Natural GC 955 sandy silt and clay-free laboratory sand (Micro-Raman)

Two kinds of sediments were loaded in our Raman chamber at the same time: natural GC 955 sandy silt and clay-free quartz laboratory sand. The sandy silt (previously called Lithofacies 2) sample was from dissociated core GC955-H005-06FB-2 at a depth of 429.46 - 429.56 meter below sea floor. The laboratory quartz sand is substantially coarser than sandy silt, with diameters ranging from 210 -297 µm. We first loaded dry sediments in the chamber using a filter paper to separate two kinds of sediment and limit clay migrations from sandy silt to sand (Figure 43). The filter paper was then removed. We then loaded vapor methane followed by 3.5 wt% NaCl aqueous solution to bring the system up to pressure. The temperature was lowered into the hydrate stability zone to synthesize methane hydrate and CH_4 hydrates formed at ~ 15.5 MPa and 280 K. Dissociation was later induced by controlled depressurization at constant temperature.

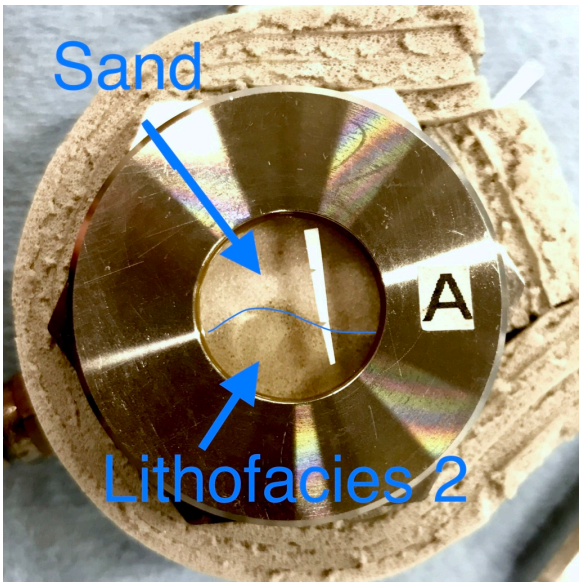

Figure 43. Photo of 2 kinds of dry sediments loaded in the Raman chamber prior to hydrate formation: natural sandy silt from core GC955-H005-06FB-2 (Lithofacies 2) and quartz sand. The mass medium diameter of Sandy silt is 40 µm). The sand diameter ranged from 210-297 µm.

6.3 Micro-Raman Observations and Analysis of Hydrate Formation

6.3.1 Observations during Hydrate Formation in glass beads

Based on thermodynamic calculations, methane hydrate is only known to form structure I (sI) hydrate as the thermodynamically stable phase, under pressure and temperature conditions relevant to natural reservoirs (< 50 MPa and T < 310 K). However, previous experiments in bulk phase without porous media have observed the coexistence of stable structure I and metastable structure II (sII) methane hydrate (Schicks and Ripmeester, 2004). As a metastable phase, sII hydrate is less stable than sI hydrate. Schicks and Ripmeester (2004) observed the structural transformation of sII hydrate recrystallizing into sI hydrate.

The coexistence of sI and sII hydrate in porous media was observed in our experiments, after forming methane hydrate in glass beads (Figure 44). Figure 45 shows the observation from a single pore where structural transformation initiated on the glass bead surfaces and progressed into the pore center over hundreds of hours. The sII hydrate converted to sI hydrate at the consumption of sII hydrate. Figure 46 shows the fractions of sI and sII hydrate over time.

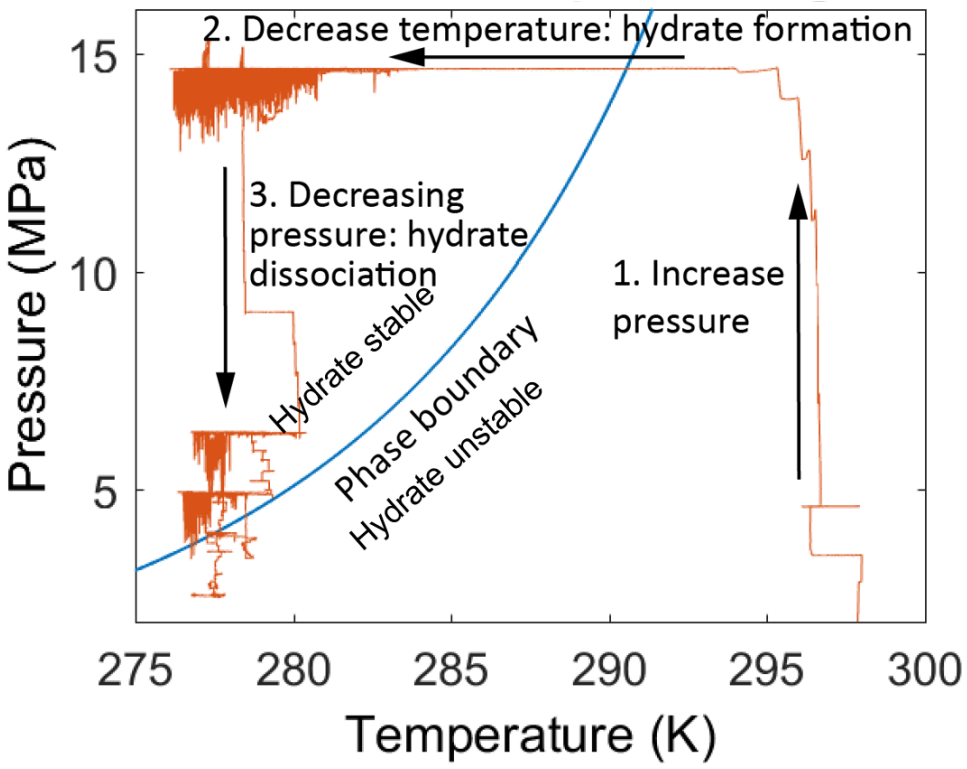

Figure 44. Pressure and temperature evolution of a hydrate formation and dissociation experiment.

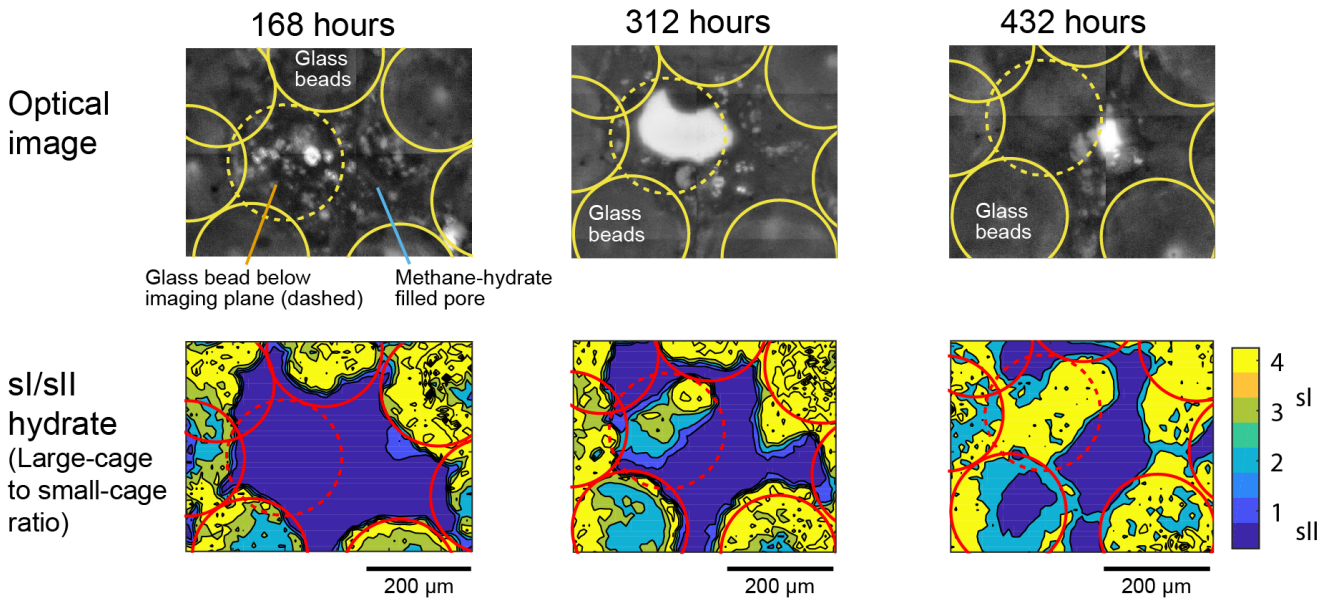

Figure 45. Annotated optical images and Raman peak intensity ratios of large to small cages (intensity of Raman peak at 2902 cm-1 to peak at 2912 cm-1). The circles outline glass beads. Upon hydrate formation, we observed the coexistence of stable sI (yellow) and metastable sII (blue) hydrate. Metastable sII to stable sI transformation initiated on grain surfaces and then progressed into the pore center. Stable sI hydrate grew into the pore space at the consumption of sII hydrate.

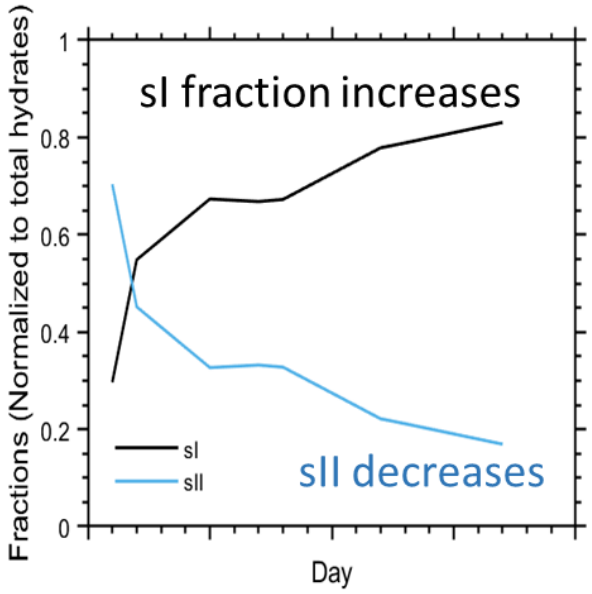

Figure 46. Fractions of structure I (sI) and structure II (sII) hydrates during hydrate formation. Since sII hydrate is metastable under the experimental conditions, sII hydrate converted to sI hydrate at the consumption of sII hydrate.

Figure 47 top shows 2D Raman maps at three representative times showing the spatial and temporal distributions of hydrate structure type, derived from the Raman spectrum at each acquisition point. Structure-I (sI) hydrate (shown as an orangey-red color) is the thermodynamically stable hydrate at the experimental condition. Figure 47 bottom, shows the ratio of large to small cages for each acquisition point and over the same time scale. sI hydrate is characterized by the slope of 3, as its quantity of large cages is three times the quantity of small cages. However, sI hydrate did not form immediately after the initial hydrate formation (1.93 hours). Over time, the hydrates gradually converted to sI hydrate, indicate by Raman peak areas along the slope of 3.48 (Figure 47, lower right).

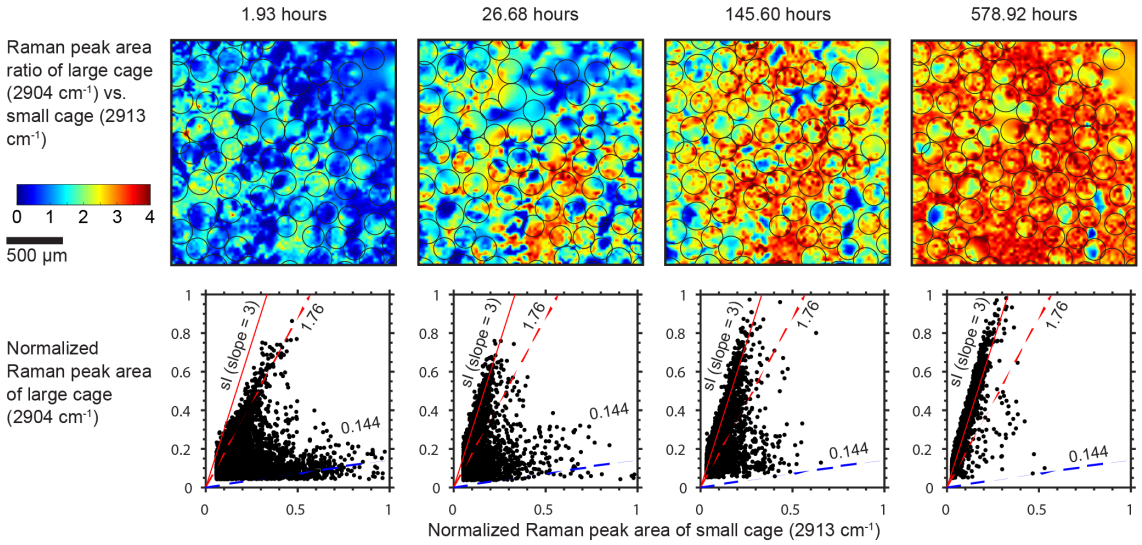

Figure 47. Pseudocolor maps and plots derived from Raman mapping data at three representative timestamps (1.93 hours, 26.68 hours, 145.60 hours, and 578.92 hours). A total of 6561 Raman measurement points (81 by 81 array) were acquired in each map, over an area of 2 mm by 2 mm at 25 μm step spacing. ***Top:*** *The Raman peak area ratios of large cages (2914 cm^{-1}) to small cages (2904 cm^{-1}) imply hydrate structure types. A ratio of 3.0 indicates structure-I (sI) hydrate (yellow color). Black circles outline the positions of the glass beads (porous medium).* ***Bottom:*** *Raman peak areas of large vs. small cages of 6561 Raman measurements (less bad or meaningless data points). The slope of 3 indicates sI hydrate.*

We repeated the previous methane hydrate formation experiment (RH009) using smaller glass beads (160 – 210 μm, RH011) mapping over a 3000 μm by 3000 μm area to (1) capture detailed Raman mapping data within 48 hours following the initial methane hydrate formation, and (2) to repeat the experiment and test reproducibility. The results are similar to those of the previous experiment (RH009) where the thermodynamically stable phase sI methane hydrate does not immediately form. Neither does the kinetically preferred sII hydrate. Instead, a mixture of sI methane hydrate and nonstoichiometric methane hydrate forms. Raman mappings reveals that the stoichiometry of methane hydrate is heterogeneous in space. Two hours after the initial methane hydrate formation, the

stoichiometry of methane hydrate is concentrated at 0.3 (shown as the darkest blue) and 1.75 (show as a greenish blue). Since the sI methane hydrate has a large-to-small-cage stoichiometry of 3 and the sII methane hydrate has that of 0.5, the average stoichiometry of an equal mixture of sI and sII methane hydrates is 1.75, which may explain 1.75 stoichiometry. However, the mixture of sI and sII hydrate cannot explain the low large-to-small-cage ratio of 0.3 in other areas. There is no know methane hydrate structure with a large-to-small-cage ratio lower than 0.5. This may suggest a new methane hydrate structure that is thermodynamically unstable but kinetically preferred at the experimental condition. The low large-to-small-cage stoichiometry may also be explained by abundant small cages that are yet to be incorporated into well-defined methane hydrate crystals. The initially formed methane hydrate may be in a chaotic configuration of large and small cages without well-defined crystalline structures. 14 hours after the initial hydrate formation, a concentrated sI methane is seen, indicated by data points along the slope of 3 (Figure 48, 14 hours). Over a long time, the thermodynamics eventually drives the methane hydrate to its thermodynamic equilibrium, that is, sI methane hydrate. At 912 hours, almost all methane hydrate confirms to the sI methane hydrate structure with a large- to small-cage ratio of 3 (Figure 48, lower right, 912 hours). Figure 49 shows the rate of conversion to sI hydrate with its large-to-small cage ratio of 3 in glass beads.

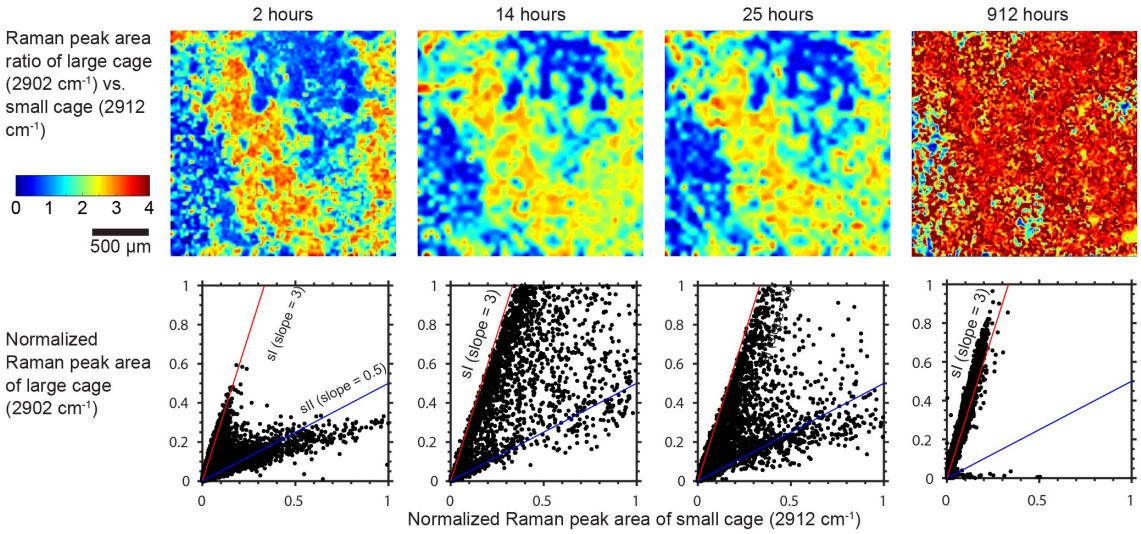

Figure 48. Raman 2D mapping and scatter plots of spatial and temporal distributions of methane hydrate large-peak to small-peak area ratios. Timestamps are zeroed at the initial methane hydrate formation. 2 hours after the initial methane hydrate formation, most of the methane hydrate formed is nonstoichiometric, meaning that it does not have a large- to small-cage ratio of 3. Over time, the methane hydrate system converges to its thermodynamic equilibrium, represented by sI methane hydrate with a large-to small- peak ratio of 3 at 912 hours.

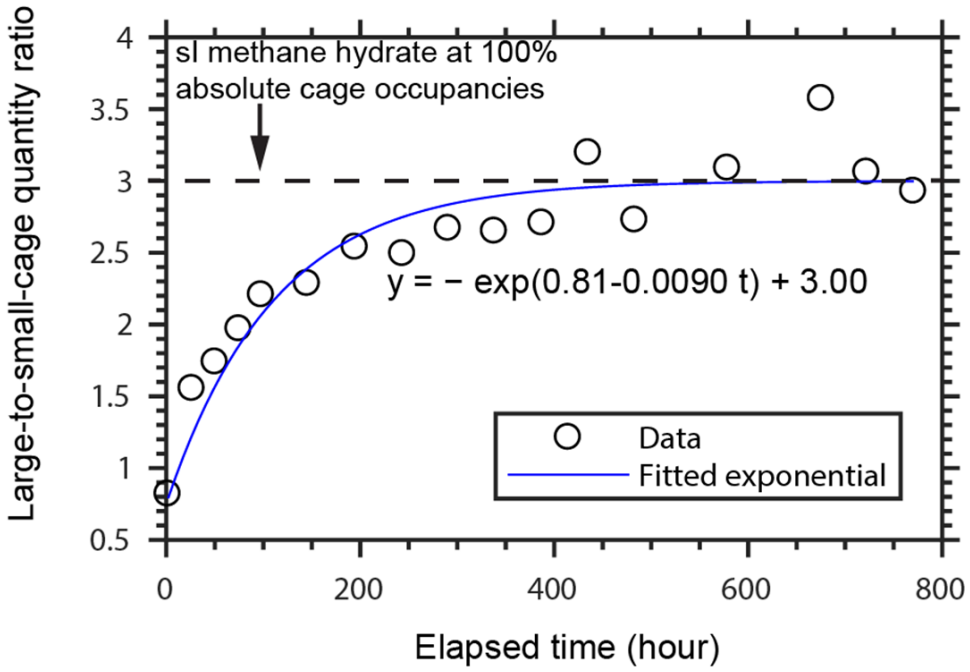

Figure 49. Rate of conversion to sI hydrate large-to-small cage ratio of 3 in glass beads.

6.3.2 Observation during Hydrate formation in mixed sand layers of different grain size distribution, experiment RH010

Observations of hydrate formation were made in in GC 955 sandy silt sediment and laboratory quartz sand. As hydrate forms we see optically the disappearance of CH_4 vapor (Figure 50 a to b), accompanied by ~ 1 MPa drop in pressure, and the appearance of the hydrate large and small cage peaks at Raman shifts of 2902 and 2912 cm^{-1}. Representative Raman spectra of the sI hydrate in the sand (blue) and the GC 955 sediment with a strong fluorescent background from the clay minerals (red) are shown in Figure 51.

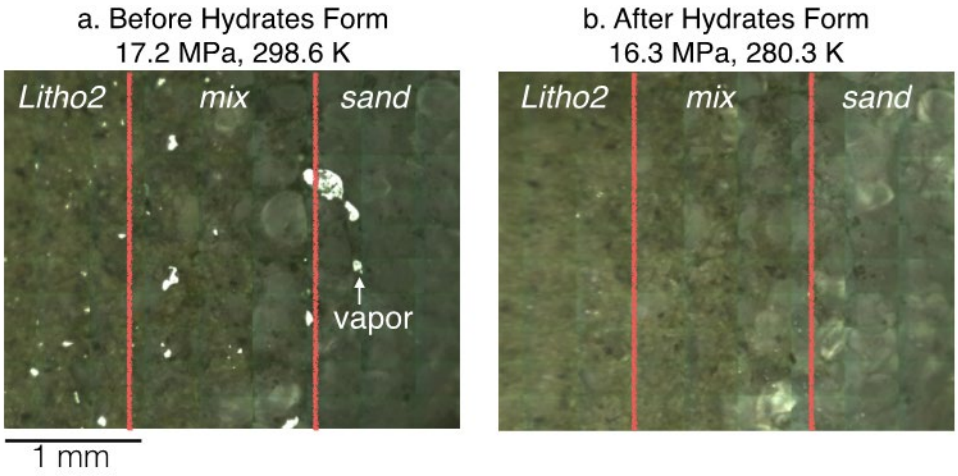

Figure 50. Optical images of the sample chamber before (a) and after (b) hydrate formation. The obvious signature of hydrate formation is the disappearance of vapor phase. The red vertical lines divide the sample chamber into three parts: Sandy silt (Lithofacies 2) in the left; a mixture of sandy silt and sand in the middle and sand in the right.

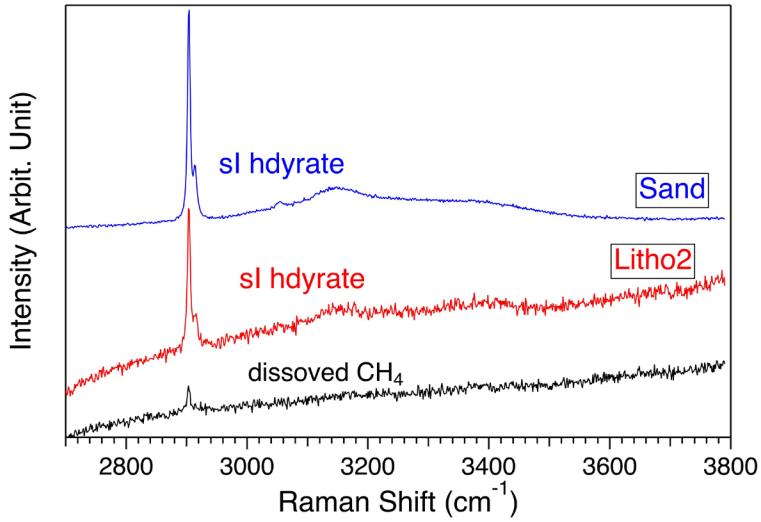

Figure 51. Representative Raman spectra of structure I (sI) methane hydrate in natural GC 955 sandy silt (Litho 2) and Quartz sand. The sandy silt is shown in red, quartz sand sample is shown in blue, and the dissolved methane vapor spectra in black. The strong fluorescence from clay minerals make the background of the red spectrum tilted.

2D mapping showing the time and spatial dependences of methane hydrates was conducted over an area of 6500 µm by 2800 µm, covering the section solely of GC 955 sandy silt, the section solely of quartz sand, and the mixed section in between (Figure 52). Each Raman data acquisition point is 50 µm apart in both X and Y directions. Thus, we acquired 7467 Raman spectra (131x 57) in each 2D mapping. During the initial stage of hydrate formation, hydrates crystallized in all three sections (Figure 52a) with the highest amount forming the mix of sandy silt and sand. Hydrates crystallizing in the GC 955 sandy silt

and mixed section had a higher large to small cage (LC/SC) ratio compared with hydrates in the courser sand (Figure 52b). Over time, less hydrate appears in the GC 955 sediment (Figure 52c and Figure 52e) and more appears in the sand (Figure 53). And, the LC/SC ratios of hydrates in the segments of mixture and sand increase and approaching the ideal LC/SC ratio of sI hydrate (Figure 52d and Figure 52f).

We interpret that this evolution of hydrate concentration and position is driven by both nucleation behavior and methane solubility. Initially, methane hydrates formation is aided by nucleation favoring the smaller clay particles present in the silty sand and mixture and the lower solubility of methane in the mixed and sand sections. Over time, the effect of methane solubility, methane being more soluble in the smaller sandy silt pores, is more pronounced. As a result, hydrates in the small pores dissolve as a dissolved methane concentration gradient forms as methane is being used up to form hydrate in the large pores of the clean sand until equilibrium is reached.

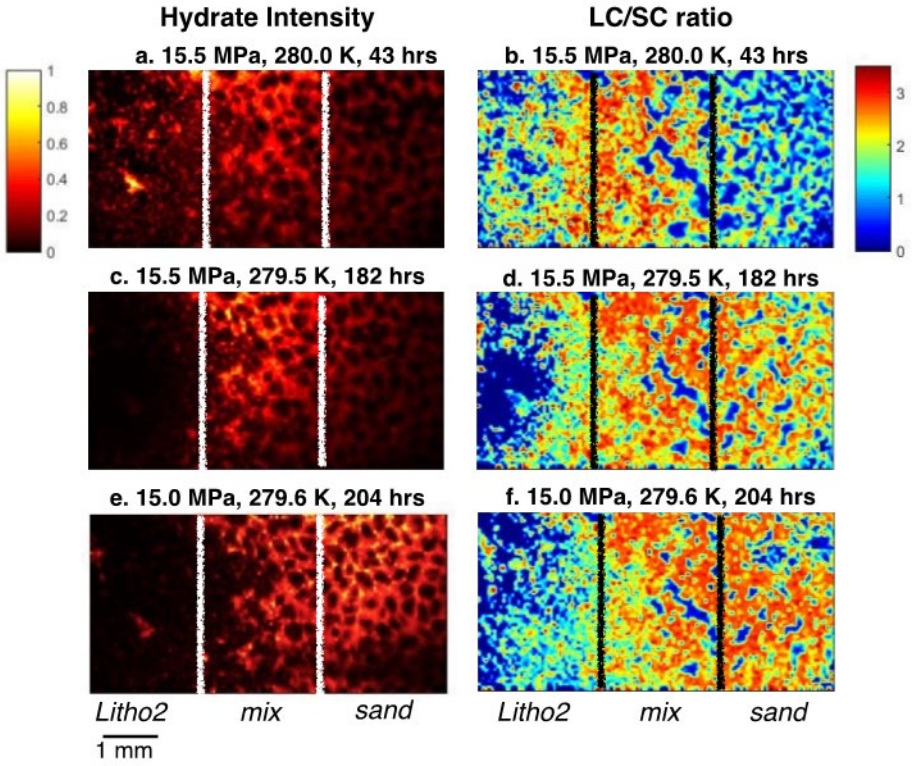

Figure 52. The spatial heterogeneity of hydrate contents and structures from 2-D Raman mappings in GC955 sandy silt and laboratory quartz sand. The two columns are Raman intensities of CH_4 peaks in hydrates and the corresponding large cage/ small cage (LC/SC) ratios. The three rows are data collected at different time. In each mapping, the sandy silt sample is on the left and quartz sand sample is on the right, while the middle part is a mixture of sandy silt and quartz sand samples.

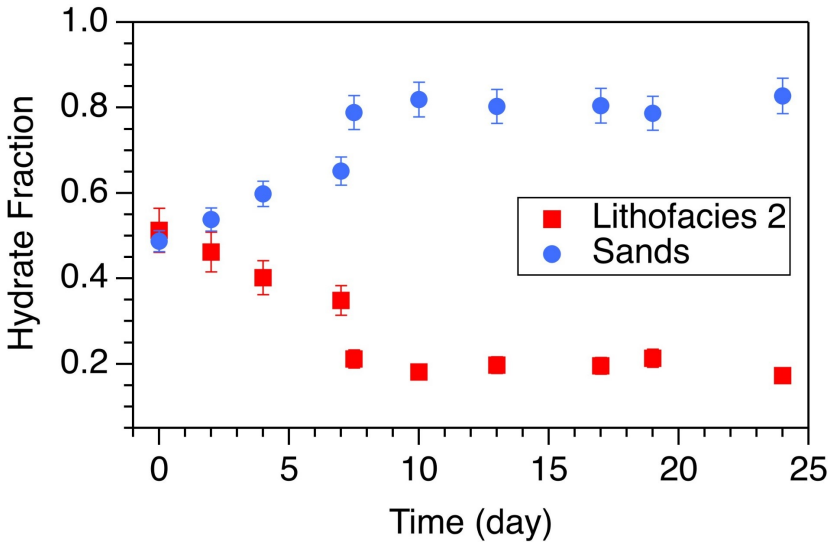

Figure 53. The temporal evolution of hydrate fractions in adjacent GC 955 sediment sandy silt (Lithofacies 2) and quartz sand layers.

6.4 Micro-Raman Observations and Analysis of Hydrate Dissociation

6.4.1 Observations during Hydrate dissociation in glass beads

We dissociated methane hydrates by depressurization at constant temperature in the Raman Chamber over 1 hour (Figure 54). We acquired Raman 2D mapping and optical images of the samples in glass beads. In the pore network (Figure 55), methane hydrate dissociated into gaseous methane and liquid water. The gaseous methane expanded radially in the pore network. At the pore scale, as shown in Figure 56, dissociation started around the glass beads. Gradually, hydrate dissociation propagated into the pore space. Methane hydrate dissociation is an endothermic reaction. We interpret that the silica glass beads provide heat to the hydrate dissociation due to their high heat capacities. We interpret that the hydrate dissociation along grains creates a connected fluid network on grain surfaces and pore networks. This connected fluid flow path may be crucial to gas hydrate reservoir permeability evolution during production. More information about the experiments can be found in the Milestone 1.H report in Appendix G.

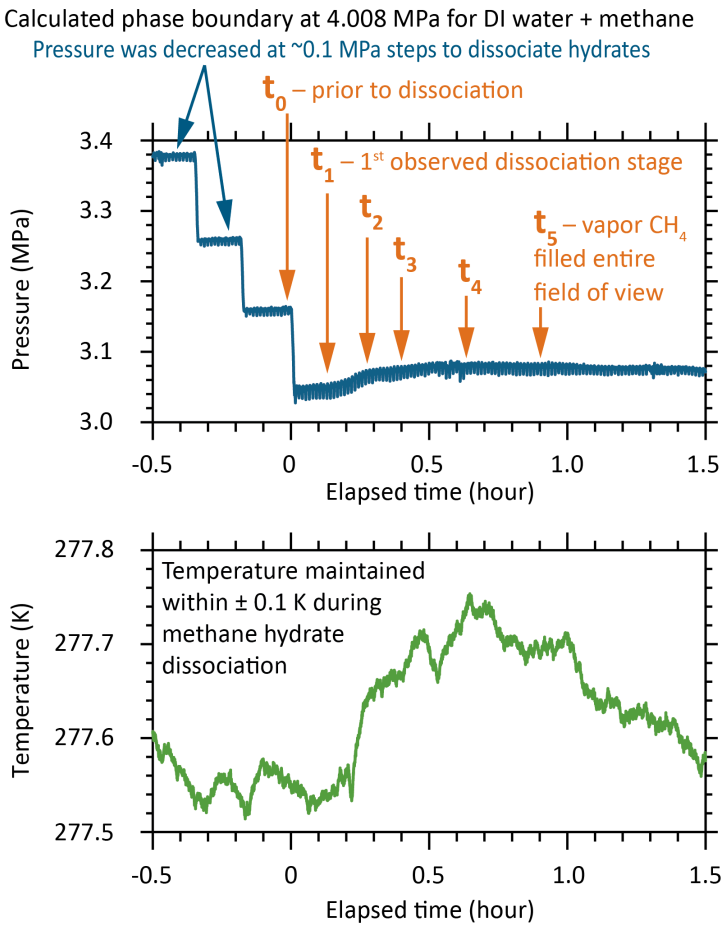

Figure 54. Pressure and temperature evolution during dissociation. Time zero (t0) is aligned to the start of the hydrate dissociation. The pressure was decreased in 0.1 MPa steps at constant temperature. Due to the small size of the sample, all hydrate dissociated after about an hour.

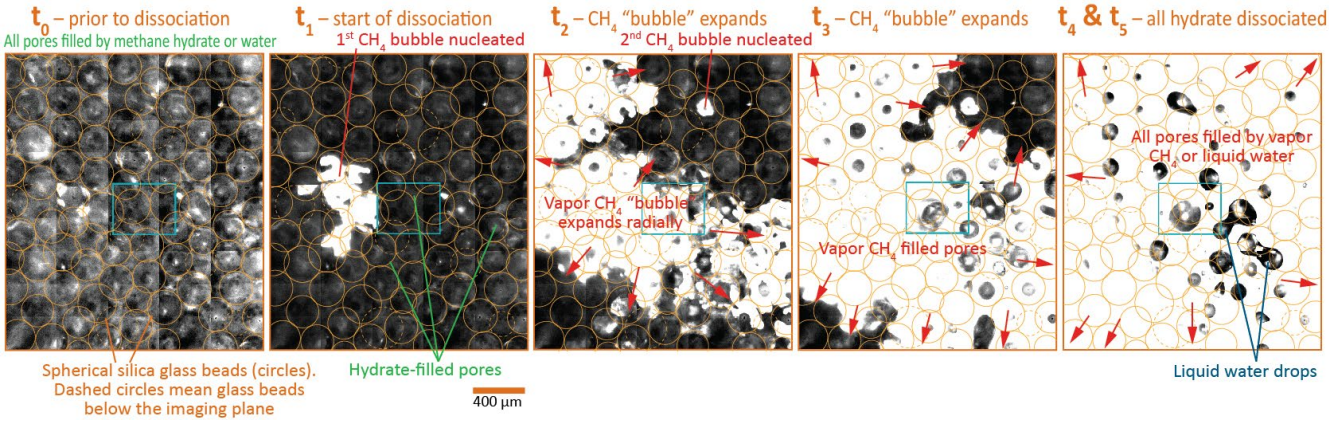

Figure 55. Radial expansion of gaseous methane in the pore network and further hydrate dissociation during depressurization. At t0, all pores were filled by methane hydrate and water. From t1 to t5, the dark regions indicated methane hydrated and water filled pores; the bright regions indicated vapor methane filled pores.

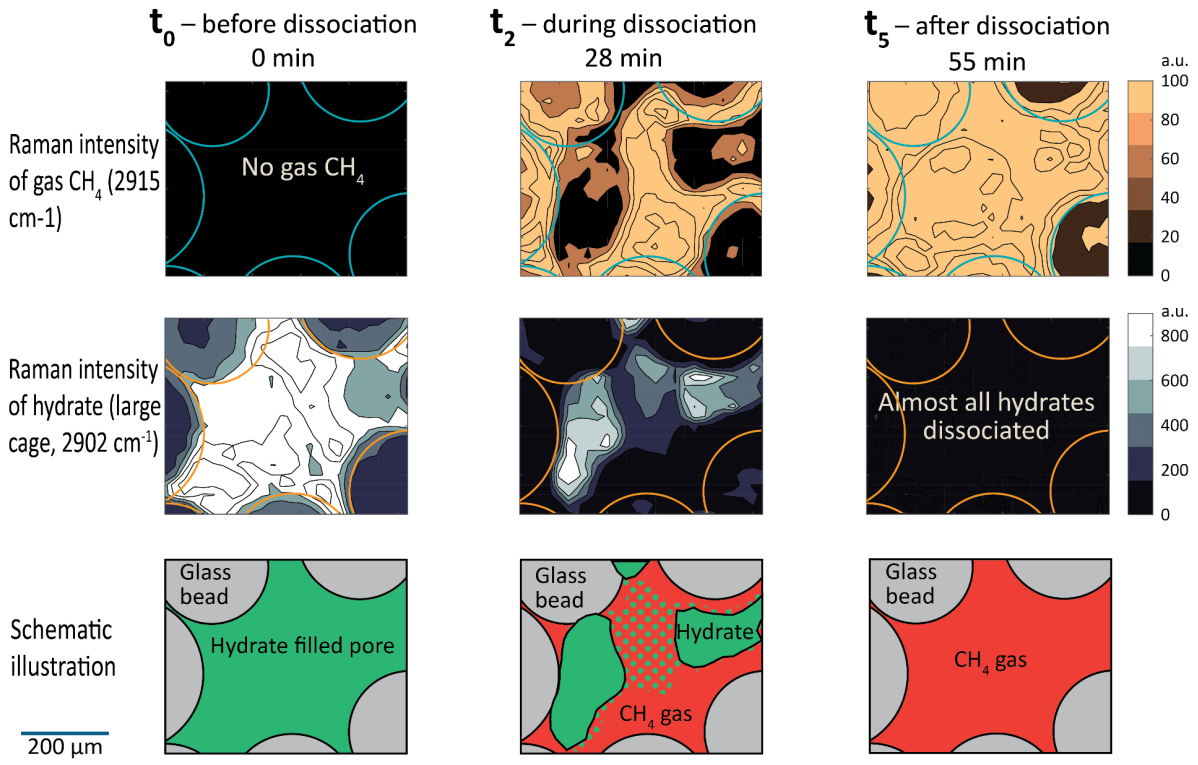

Figure 56. Raman maps and schematic illustrations of methane hydrate dissociation by controlled depressurization. At t0, prior to dissociation, we observed no CH4 gas. Gradually, at t2 (after 28 minutes), indicated by 2D Raman mapping in the pore space, methane hydrate dissociation started along the porous medium grains (silica glass beads) and propagated into the pore space center. The methane released from hydrate phase transitioned into vapor phase.

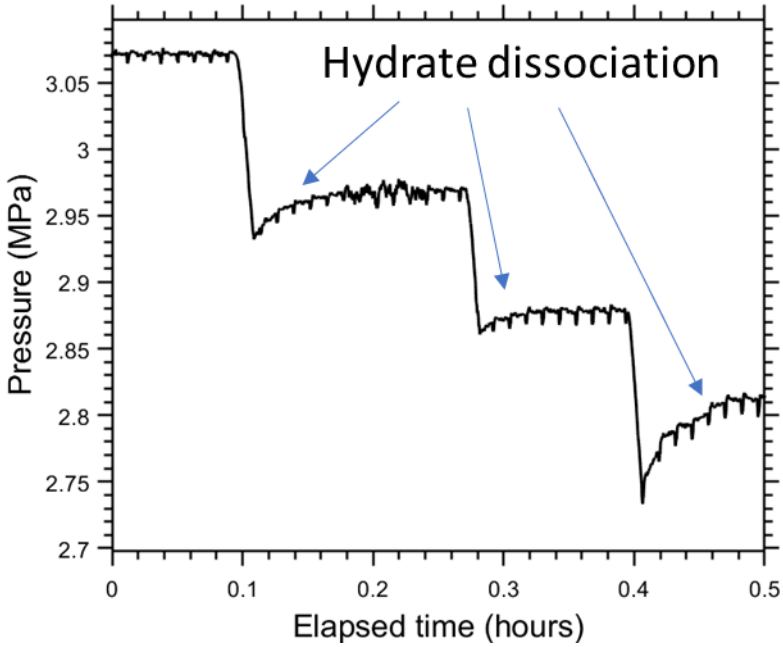

Figure 57. Pressure rebounds during depressurization of hydrate between glass beads similar to core scale depressurization (Task 7.).

6.4.2 Observation during Hydrate dissociation in Natural GC 955 sandy silt and clay-free laboratory sand (Micro-Raman), experiment RH010

During depressurization of the methane hydrate formed in the layered system of GC 955 sediment and quartz sand, the Raman intensity of methane hydrate decreased as an indication of hydrate dissociation (Figure 58 comparing top row, 10.5 hours, and middle row, 32.2 hours) and methane vapor appeared in the sand (Figure 59). Dissociation is first recorded in the finest grained sediment (LF2, Figure 59) even though hydrate concentration is much higher in the coarser grained material (Figure 58). Dissociation then proceeds to the coarser grained material.

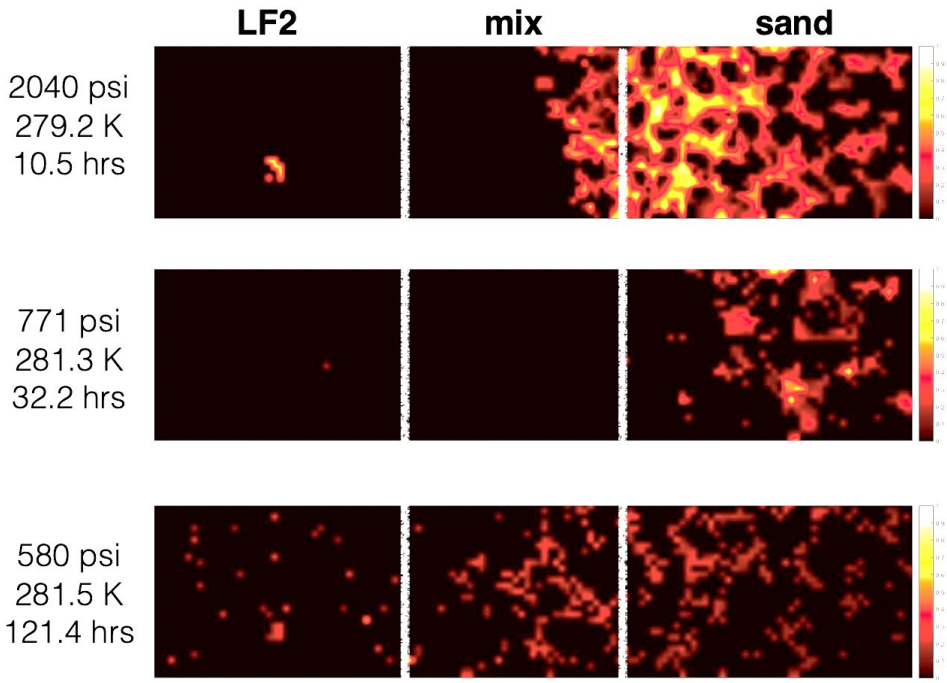

Figure 58. Methane hydrate Raman 2D mapping during methane hydrate dissociation in experiment RH010. The mapping was conducted near the boundary of the GC 955 sandy silt (Litho 2, LF2) and laboratory quartz sand. Materials and fluids can flow freely across the GC 955 sediment, the mixture (mix), and sand layers. Higher intensity (yellow-white color) indicates higher methane hydrate concentration in pore spaces.

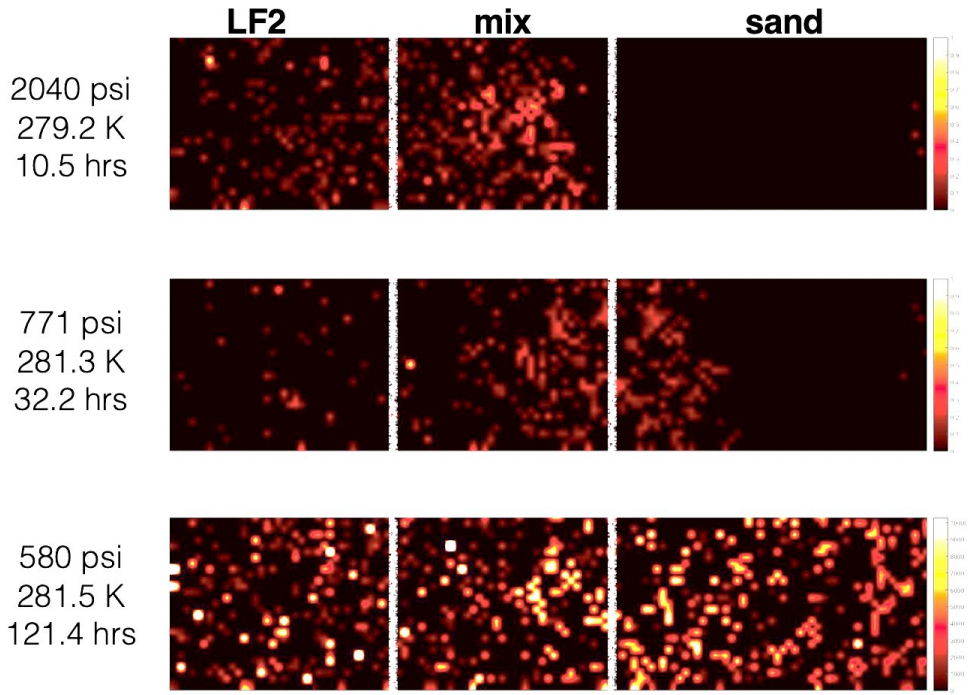

Figure 59. Methane vapor Raman 2D mapping during methane hydrate dissociation in experiment RH010. The mapping was acquired at the same position as Figure 58. Higher intensity (yellow-white color) indicates higher methane vapor presence in the pore spaces.

Conclusions

We explored the relative permeability and dissipation behavior of hydrate-bearing coarse-grained sediment at the core scale and we observed the formation and dissociation of these materials at the pore scale with micro-CT and Raman experiments. The 3-year project results inform reservoir simulation efforts, critical to determining the viability of the coarse-grained hydrate reservoir as an energy resource.

We performed the first 3 phase relative permeability experiments in a hydrate-bearing medium using the steady state method (gas and water flow in the presence of hydrate). Results support a model where water is the most wetting phase, hydrate is the intermediate wetting phase, and gas is the least wetting phase. This model can be used to predict relative permeability of gas and water in the presence of hydrate.

We showed that when hydrate dissociates, it does so at a pressure and temperature predicted for fresh water (no salinity) conditions. At the scale of a grid block, reservoir simulation models should assume that hydrate dissociates at the freshwater phase boundary.

We observed that the chemistry and the pore habit of methane hydrates change dramatically over the timescales of experiments (hours to weeks). It takes weeks to months for hydrates to evolve from a non-stoichiometric to stoichiometric compound with 3:1 large cage vs small cage occupancy. We documented hydrates forming initially in small clayey silt surfaces but gradually concentrated in large pores in sand-sized sediment.

References

Brooks, R.H., Corey, A.T., 1964. Hydraulic properties of porous media. Hydrology Papers 3. Colorado State University, Fort Collins.

Chen, X., Kianinejad, A., and DiCarlo D.A., 2017, Measurements of CO2-brine relative permeability in Berea sandstone using pressure taps and a long core: Greenhouse Gases Science and Technology, v.7, p. 370-382. https://doi.org/10.1002/ghg.1650

Clennell, M. B., Hovland, M., Booth, J.S., Henry, P., and Winters, W.J., 1999, Formation of natural gas hydrates in marine sediments 1. Conceptual model of gas hydrate growth conditioned by host sediment properties: Journal of Geophysical Research, v. 104, P. 22985-23003.

Flemings, P.B., Phillips, S.C, Collett, T., Cook, A., Boswell, R., and the UT-GOM2-1 Expedition Scientists, 2018. UT-GOM2-1 Hydrate Pressure Coring Expedition Summary. In Flemings, P.B., Phillips, S.C, Collett, T., Cook, A., Boswell, R., and the UT-GOM2-1 Expedition Scientists, UT-GOM2-1 Hydrate Pressure Coring Expedition Report: Austin, TX (University of Texas Institute for Geophysics, TX). https://ig.utexas.edu/energy/genesis-of-methane-hydrate-in-coarse-grained-systems/expedition-ut-gom2-1/reports/

Kleinberg, R. L., Flaum, C., Griffin, D. D., Brewer, P. G., Malby, G. E., Peltzer, E. T., & Yesinowski, J. P. (2003). Deep sea NMR: Methane hydrate growth habit in porous media and its relationship to hydraulic permeability, deposit accumulation, and submarine slope stability. Journal of Geophysical Research -- Solid Earth, 108(B10), 2508. https://doi.org//10.1029/2003JB002389

Meazell, K., Flemings, P., and Santra, M., in review, Silt-rich channel-levee hydrate reservoirs 1of Green Canyon 955: American Association of Petroleum Geologist Bulletin.

Meyer, D. W., Flemings, P. B., DiCarlo, D., You, K. H., Phillips, S. C., and Kneafsey, T. J., 2018, Experimental Investigation of Gas Flow and Hydrate Formation Within the Hydrate Stability Zone: Journal of Geophysical Research-Solid Earth, v. 123, no. 7, p. 5350-5371.

Murphy, Z. W. (2018). Three-Phase Relative Permeability of Hydrate-Bearing Sediments. Master's Thesis. Hildebrand Department of Petroleum and Geosystems Engineering, University of Texas-Austin.

Phillips, S. C., Flemings, P. B., Holland, M. E., Schulthiss, P. J., Waite, W. F., Jang, J., Petrou, E. G., and H., H., accepted, High concentration methane hydrate in a deepwater silt reservoir from the northern Gulf of Mexico: American Association of Petroleum Geologist Bulletin.

Phillips, S. C., Flemings, P. B., You, K., Meyer, D. W., and Dong, T., 2019, Investigation of in situ salinity and methane hydrate dissociation in coarse-grained sediments by slow, stepwise depressurization: Marine and Petroleum Geology, v. 109, p. 128-144.

Schicks, J. M., & Ripmeester, J. A. (2004). The coexistence of two different methane hydrate phases under moderate pressure and temperature conditions: Kinetic versus thermodynamic products. Angewandte Chemie International Edition, 43(25), 3310-3313.

You, K., Kneafsey, T.J., Flemings, P.B., Polito, P., and Bryant, S.L., 2015, Salinity-buffered methane hydrate formation and dissociation in gas-rich systems: Journal of Geophysical Research: Solid Earth, v. 120, p. 643-661.

Acronyms

Table 4. List of Acronyms

A	Area (m^2)
BPR	Back pressure regulator
CT	Computed Tomography
DI	Deionized water
DOE	US Department of Energy
FB	Face bit configuration of the pressure coring tool with ball valve
GC 955	Gulf of Mexico, Green Canyon Block 955
H+L	Hydrate + Liquid
HDT	Hydrate Depressurization Test
HSZ	Methane hydrate stability zone
ISCO	Teledyne ISCO, Teledyne purchase of part of the Irrigation Supply Co.
k_{abs}	Absolute permeability
k_{eff}	Effective permeability
KI	Potassium iodide
k_r	Relative permeability , the ratio of the effective permeability to the absolute permeability
L	Length (m)
LC/SC	Methane hydrate large cage to small cage occupancy ratio
LF2	GC 955 Sandy silt, previously referred to as lithofacies 2
Litho	Lithofacies
μ	Viscosity (Pa-s), or micro, per context
Macro-	Meter scale
M_{CH4}	Molar mass of methane (16 g/mol)
M_H	Molar mass of sI hydrate (119.5 g/mol)

Micro-	Micrometer scale
M_w	Molar mass of water
NaBr	Sodium Bromide
NaCl	Sodium Chloride
NETL	National Energy Technology Laboratory of the US Department of Energy
ΔP	Pressure drop (Pa)
ρ_{CH4}	Density of methane gas at experimental conditions (0.07225 g/cm^3)
PCATS	Pressure Core Analysis and Transfer System
PTFE	Polytetrafluoroethylene
PT, or P-T	Pressure-Temperature
Q	Flow rate (m^3/s)
R	Conversion rate
Raman	Raman spectroscopy
ρ_H	Density of sI hydrate (0.925 g/cm^3)
ρ_w	Density of water, and
sI	Methane Hydrate chemical structure 1
sII	Methane Hydrate chemical structure 2
S_b	Brine saturation
S_n	Non-wetting phase saturation
S_w	Wetting phase saturation
STP	Standard Temperature and Pressure
UT	University of Texas
UT-GOM2-1	University of Texas Hydrate Pressure Coring Expedition
V+L	Vapor + Liquid
V_p	Pore volume
V_{CH4}	Volume of methane
V_W	Volume of water
V_{eff}	Effective (fluid-filled) pore volume
V_{pore}	Total pore volume

Appendix A

DOE Award No.: DE-FE-0028967

Revised Milestone Report

Milestone 2.A: - Measurement of relative permeability in sand-pack cores

SUMMARY

This milestone report summarizes our achievement of measuring relative permeability in sand-pack cores. This Millstone is specific to Subtask 6.1 *Steady-State Relative Permeability Measurements of Sand-Pack Hydrate Samples*. The following sections summarize the conception, testing, experimental procedure, and results. The PIs in charge of this task are H. Daigle and D DiCarlo. Z. Murphy executed design, followed device construction, and performed experiments with assistance from Peter Polito and Joshua O'Connell.

A. Introduction

As part of the overall project goal of understanding the macro- and microscale fluid flow properties of coarse-grained hydrate reservoirs, we measured the relative permeability for (1) two-phase flow of either gas and brine or brine in the presence of hydrate, and (2) simultaneous flow of gas and brine in the presence of hydrate. These experiments were performed in sandpacks and Berea sandstone. Berea was selected as its intrinsic permeability (220 mD) is comparable to that of coarse-grained marine sediments that are of interest to the hydrate community. We successfully performed 11 measurements of gas-brine relative permeability, 4 measurements of brine relative permeability in the presence of hydrate at hydrate saturations ranging from 12% to 60%, and 5 measurements of simultaneous flow of gas and brine in the presence of hydrate at a hydrate saturation of 25%.

B. Methods

The methods of relative permeability measurement are outlined in the Year 2 Quarter 4 quarterly report (https://www.netl.doe.gov/sites/default/files/2018-11/FE0028967-qpr-jul-sep-2018%5B1%5D.pdf).

C. Results

Before hydrates were formed, the complete drainage gas-water relative permeability curve was measured, a key step that no other hydrate relative permeability experiments have conducted. Gas-water relative permeability for Berea Sandstone has been well studied and provides a good database to confirm and compare results. Using Darcy's Law (2.A.1) and the Darcy-Buckingham equation (2.A.2), the relative permeability was measured for a two-phase system (gas and water) (Fig. 2.A.1).

$$k_{abs} = \frac{Q\mu}{A}\frac{L}{\Delta P}, \quad (2.A.1)$$

$$k_{r,i} = \frac{Q_i\mu_i}{Ak_{abs}}\frac{L}{\Delta P_i}, \quad (2.A.2)$$

where k_{abs} is the absolute (intrinsic) permeability, Q is the flow rate, A is the cross-sectional area of the core, L is the length of the core, and ΔP is the pressure drop. The subscripts in 2.A.2 refer to the i^{th} phase; $k_{r,i}$ is the relative permeability of the i^{th} phase.

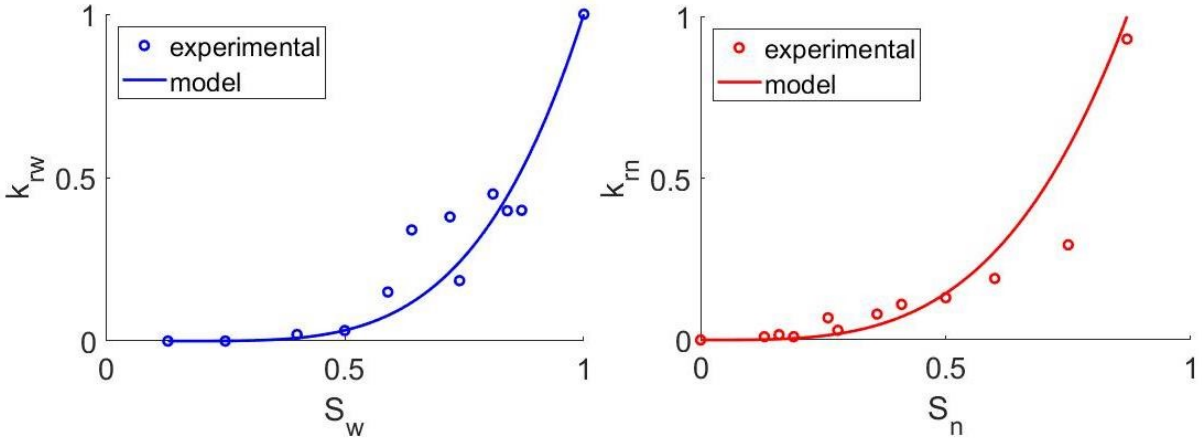

Figure 2.A.1. Two-phase (gas/water) relative permeability for a Berea Sandstone core.

Hydrates were formed in a pressure vessel and an estimated hydrate saturation of 25% was achieved (Murphy, 2018; Appendix A). Water was flowed through the sample until only water and hydrate remained. Once steady-state was achieved, the pressure drop was measured. The resulting relative permeabilities are shown in Fig. 2.A.2.

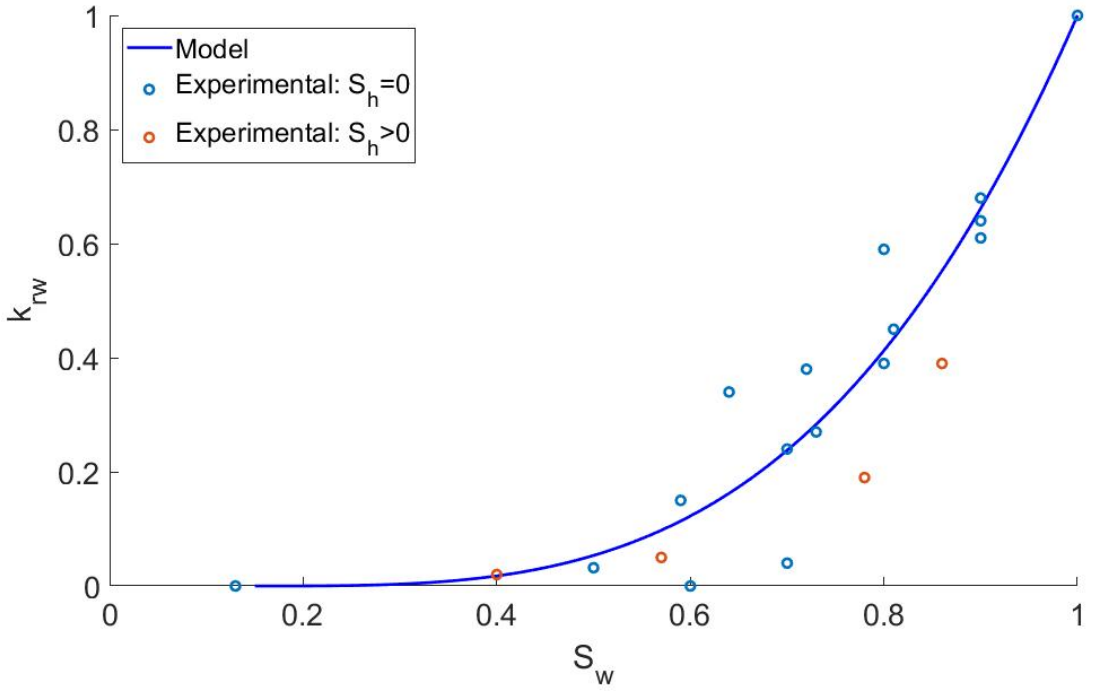

Figure 2.A.2. Water relative permeability for a Berea Sandstone without (blue) and with (red) hydrate. For the hydrate experiments, there was no free gas present in the sample, meaning it is at two-phase conditions.

Our proposed approach for modeling three-phase (hydrate, gas, and water) relative permeability is to use the Saturation Weighted Interpolation (SWI) method. For the intermediate phase, the SWI method uses the two endmember relative permeability curves and weights them depending on the other two-phase saturations (e.g. brine and hydrate).

For example, if S_h = 0.25, then $k_{r,w} \approx 0.13$. A scaled Brooks-Corey model (Brooks and Corey, 1964) can be determined by combining the two-phase Brooks-Corey equation with the pore-filling hydrate relative permeability model of Kleinberg et al. (2003):

$$k_{r,w} = \left(\frac{S_w - S_{r,w}}{1 - S_{r,w}}\right)^{n_w} \left(k_{abs}\left[1 - S_h^2 + \frac{2\left(1 - S_h^2\right)^2}{\log S_h}\right]\right), \quad (2.A.3)$$

$$k_{r,g} = \left(\frac{S_g - S_{r,g}}{1 - S_{r,g}}\right)^{n_g} \left(k_{abs}\left[1 - S_h^2 + \frac{2\left(1 - S_h^2\right)^2}{\log S_h}\right]\right), \quad (2.A.4)$$

where S_w is water saturation, $S_{r,w}$ is the residual water saturation, n_w is the water exponent, S_h is hydrate saturation, S_g is gas saturation, $S_{r,g}$ is the residual gas saturation, and n_g is the gas exponent. Figure 2.A.3 shows some example relative permeability predictions with Eqs. 2.A.3 and 2.A.4.

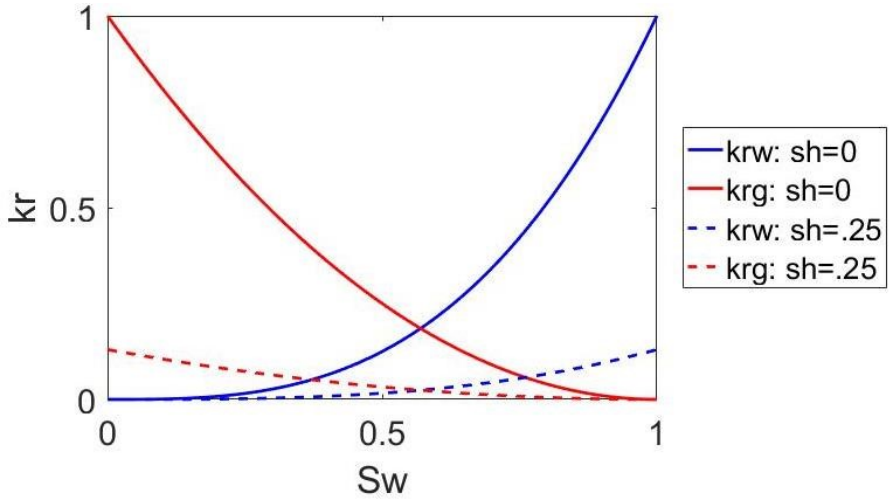

Figure 2.A.3. Brooks-Corey relative permeability model without hydrate, and scaled for 25% hydrate saturation. The hydrate-free Brooks-Corey model is scaled with $k_{r,w}$ = 0.13.

Relative permeability is traditionally plotted as a function of water saturation. However, due to equipment limitations and difficulty in measuring three-phase saturation, the relative permeability data is plotted against the fraction flow rate of water f_w:

$$f_w = \frac{Q_w}{Q_w + Q_g}, \quad (2.A.5)$$

where Q_w is the water volumetric flow rate and Q_g is the gas volumetric flow rate. For experimental data, the flow rates are set throughout the experiment. Therefore, f_w is an experimental parameter that is known at all points during each experiment. However, flow rate is not a parameter in modeled relative permeability. S_w must be converted into f_w by assuming plug flow and assuming that:

$$V_{eff} = V_{pore}(1 - S_h), \quad (2.A.6)$$

$$f_w = \frac{S_w}{V_{eff}} \quad (2.A.7)$$

where V_{eff} is the effective (fluid-filled) pore volume and V_{pore} is the total pore volume. Since the experimental data will be plotted against f_w, all models must be converted in order to be directly compared. If the plug flow assumption is not valid, f_w can also be solved for using the Darcy-Buckingham equation (2.A.2). Combining equation (2.A.2) and (2.A.5):

$$f_w = \frac{\frac{k_{r,w}}{\mu_w}}{\frac{k_{r,w}}{\mu_w}+\frac{k_{r,g}}{\mu_g}}. \qquad (2.A.8)$$

The viscosities and relative permeabilities are known. Therefore, the fraction flow of water (f_w) can be solved for each model. This conversion allows comparison of preliminary experimental results, but saturations must still be determined.

Experimentally measured three-phase relative permeability data was collected using the method described in Murphy (2018). Before hydrate formation, a two-phase (gas/water) drainage relative permeability curve was measured for the sample (Fig. 2.A.3). Hydrates were then formed using the excess gas method. The hydrate saturation was estimated to be 25%. Initially, only brine was flowed through the core. The resulting values are simply endpoint relative permeability points (f_w = 1). Gas is then co-injected into the core to decrease the f_w value. Steady-state ($\partial P/\partial t = 0$) is reached at each value of f_w. The gas and water relative permeability values are measured at each f_w until f_w = 0 (Fig. 2.A.4).

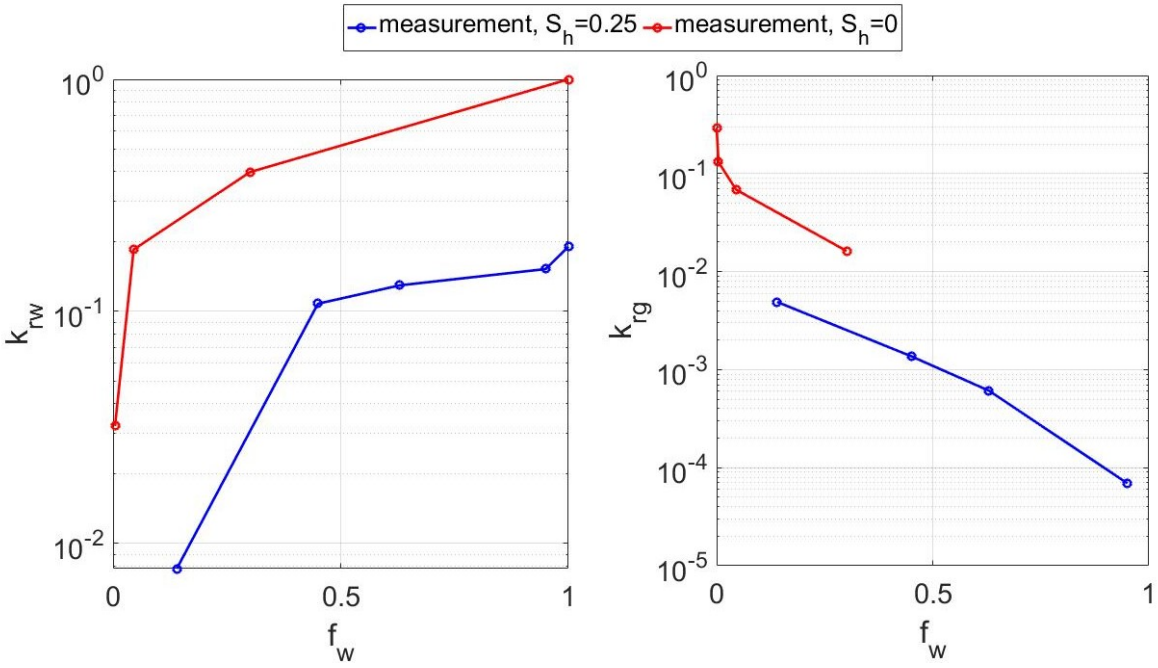

Figure 2.A.4. Experimentally measured gas and water relative permeability in the presence of hydrate (S_h = 0.25).

The experimentally derived relative permeability curves can be used to compare to the models discussed previously. Using the Kleinberg et al. (2003) scaling approach for $S_h = 0.25$ and $k_{r,w} = 0.13$. The experimentally measured relative permeability with no hydrate is then scaled by 0.13 (Fig. 2.A.4).

D. References

Brooks, R.H., Corey, A.T., 1964. Hydraulic properties of porous media. Hydrology Papers 3. Colorado State University, Fort Collins.

Kleinberg, R. L., Flaum, C., Griffin, D. D., Brewer, P. G., Malby, G. E., Peltzer, E. T., & Yesinowski, J. P. (2003). Deep sea NMR: Methane hydrate growth habit in porous media and its relationship to hydraulic permeability, deposit accumulation, and submarine slope stability. Journal of Geophysical Research -- Solid Earth, 108(B10), 2508. https://doi.org//10.1029/2003JB002389

Murphy, Z. W. (2018). Three-Phase Relative Permeability of Hydrate-Bearing Sediments. Master's Thesis. Hildebrand Department of Petroleum and Geosystems Engineering, University of Texas-Austin.

Appendix B

DOE Award No.: DE-FE-0028967

Milestone Report

Milestone 2.B: Measurement of relative permeability in intact pressure cores

SUMMARY

This milestone report summarizes our achievement of measuring relative permeability in intact pressure cores. The following sections summarize the conception, testing, experimental procedure, and results for permeability measurements of intact pressure cores from UT-GOM2-1. The PIs in charge of this task are P. Flemings, H. Daigle and D DiCarlo. Yi Fang performed experiments with assistance from Joshua O'Connell.

A. Introduction

To compare our laboratory results with measurements on real material, we measured the relative permeability of brine in the presence of hydrates in intact pressure cores from Green Canyon 955 in the Gulf of Mexico. Two samples of hydrate-bearing sandy silt were selected based on x-ray images, bulk density measurements, and acoustic velocity measurements made with the Geotek pressure core analysis and transfer system (PCATS). The two samples had hydrate saturations of 83% and 90%.

B. Methods

The pressure cores were first subsampled and transferred to the permeameter chamber using the Geotek mini-PCATS, Figure B.1. The cores were maintained at a pressure of 25 MPa and a temperature of 6-7°C throughout the process.

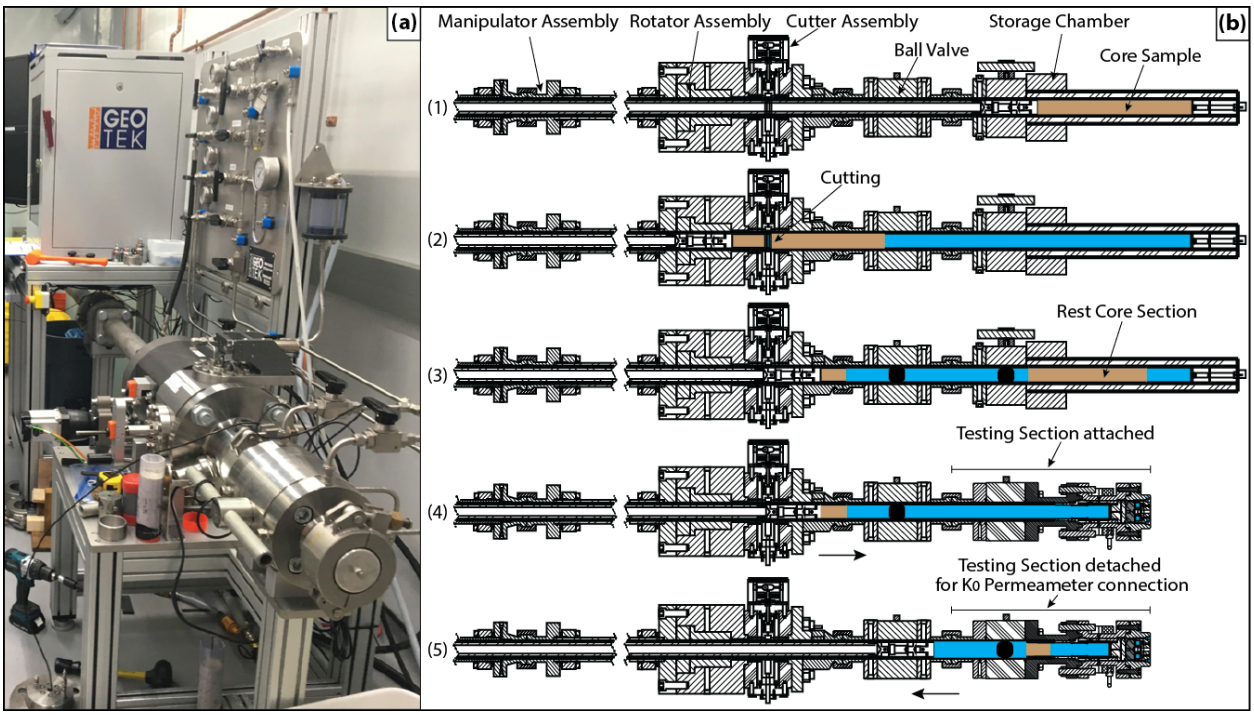

Figure B.1. Mini-PCATS cutting and transfer (a) Photograph of mini-PCATS in use. (b) Cutting and transfer process to place intact pressure core material in the permeameter.

In the cutting and transfer process, the main storage chamber is connected to the cutter assembly with a ball valve (Figure B.1, 1). The sample is then pulled into the cutter using the manipulator and the desired section is cut (Figure B.1, 2). The remaining portion of the original core is then pushed back into the storage chamber (Figure B.1, 3). The storage chamber is removed and the permeameter is then connected to the ball valve (Figure B.1, 4). Once the permeameter is connected, the cut sample is pushed into the permeameter (Figure B.1, 5). The permeameter can then be disconnected and moved to the analysis room.

Once in the permeameter cell, the sample is reconsolidated to the estimated in situ effective stresses. During this process, several measurements of effective permeability were made. These measurements were done using steady-state flow of brine through the core.

To obtain a better estimate of the intrinsic permeability, the samples were dried and resedimented to the in situ vertical effective stress in a consolidation cell. The resedimentation process allowed us to remove the effects of fines migration and any fabric disturbance that would have occurred as a result of degassing.

C. Results

Effective permeability results are shown in Figure B.2a. Once the target effective stresses were reached and the effective permeability measured, the sample was degassed at constant horizontal effective stress. After degassing, the sample was vacuumed and re-saturated with brine to measure the intrinsic permeability, which was assumed to be the permeability of the sediment in the absence of hydrate. As Figure B.2b shows, for some samples the intrinsic permeability was lower than the effective

permeability with hydrate in the pore space, which is counterintuitive. This phenomenon was attributed to the migration of fine particles during the test.

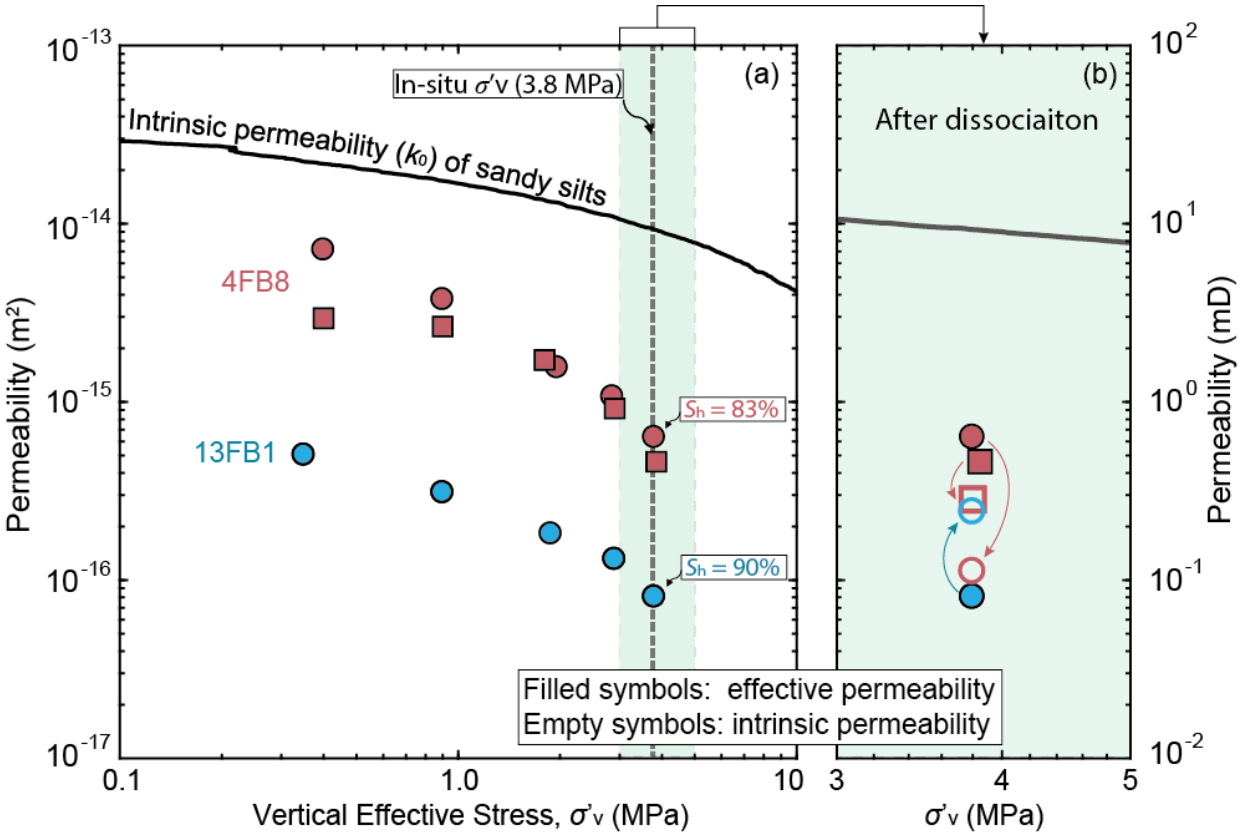

Figure B.2. GC 955 sandy silt effective and intrinsic permeability (a) Effective permeabilities measured during reconsolidation to in situ conditions. (b) Change in permeability after degassing. Note that sample 4FB8 experienced a decrease in permeability after degassing, which was unexpected.

The resedimented permeability was then measured during a consolidation test. Using the resulting intrinsic permeability values, we were able to determine the in situ relative permeabilities of the samples. The resulting values fit with the trend of the synthetic samples and help define the portion of the data at high hydrate saturations that we did not achieve in the laboratory. The results are shown in Figure B.3.

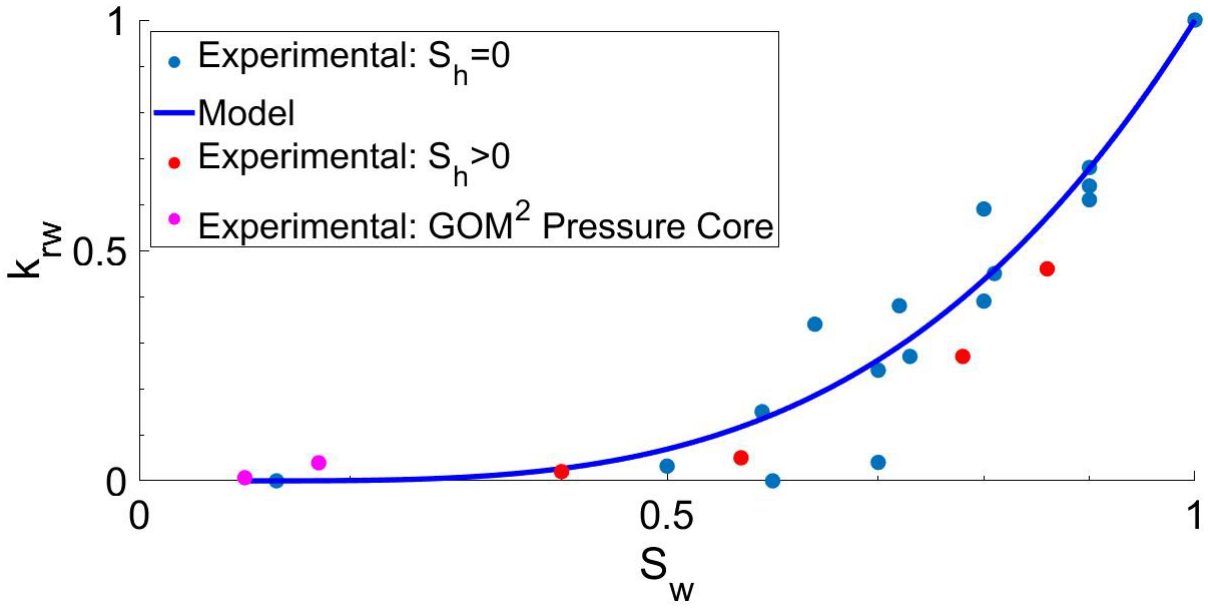

Figure B.3. Wetting-phase relative permeability values for all samples tested. Blue dots: water-phase relative permeability in the presence of methane gas in synthetic samples. Red dots: water-phase relative permeability in the presence of hydrate (no gas) in synthetic samples. Magenta dots: water-phase relative permeability in the presence of hydrate (no gas) in intact pressure core samples.

Appendix C

DOE Award No.: DE-FE-0028967

Milestone Report

Milestone 2.C: Depressurization of intact hydrate samples and documentation of thermodynamic behavior

SUMMARY

This milestone report summarizes our achievement of Depressurization of intact hydrate samples and documentation of thermodynamic behavior. This Milestone is specific to Task 7. *Macro-Scale: Depressurization of Methane Hydrate Sand Packs and Intact Pressure Core Samples*. The following sections summarize the experimental setup, results, and achievement of the milestone. The PI in charge of this task is P.B. Flemings. S.C. Phillips designed and performed the experiments.

A. Introduction

We depressurized methane hydrate-bearing samples from the northern Gulf of Mexico to document their thermodynamic behavior (temperature, pressure, salinity). These samples provide an opportunity to better understand the thermodynamic state of a real hydrate reservoir and its response to depressurization. The hydrate saturation of the coarse-grained samples is higher (> 80% of the pore space) than any of the synthetic hydrates in sand packs (< 32%).

B. Methods

The methods of depressurization of intact hydrate samples are outlined in detail within (Flemings et al., 2018a) and (Phillips et al., accepted). The goal of these experiments was to depressurize natural hydrate-bearing sediments while quantifying the total amount and composition of gas released from the hydrate. We also measured the pressure and temperature immediately adjacent to the sample using data storage tags. Using these pressure and temperature measurements we estimate the in situ salinity of the sample at the onset of dissociation based on the phase boundary of methane hydrate. We then use salinity estimates along with the hydrate saturation and porosity to calculate how the salinity and phase boundary pressure should decrease during hydrate saturation using an approach similar to (Phillips et al., 2019).

C. Results

We show that we can estimate the in situ salinity of a sample based on pressure and temperature within the sample at the onset of dissociation. We then document that the observed pressure during dissociation is lower than that predicted by a bulk equilibrium model (Figure C.1). By observing pressure rebounds during periods of sample shut-in (Figure C.2) we suggest that the dissociation is controlled by a local equilibrium where locally-freshened pore waters surround dissociating hydrate. Over the course of a pressure rebound and continued dissociation, the sample cools for several hours followed by warming (Figure C.3). The increase in pressure during the intervals of warming suggests that the sample salinity is increasing over hours to days. During pressure rebounds while the sample is shut-in, the pressure of the sample increases as the salinity increases and hence the local phase boundary pressure rises.

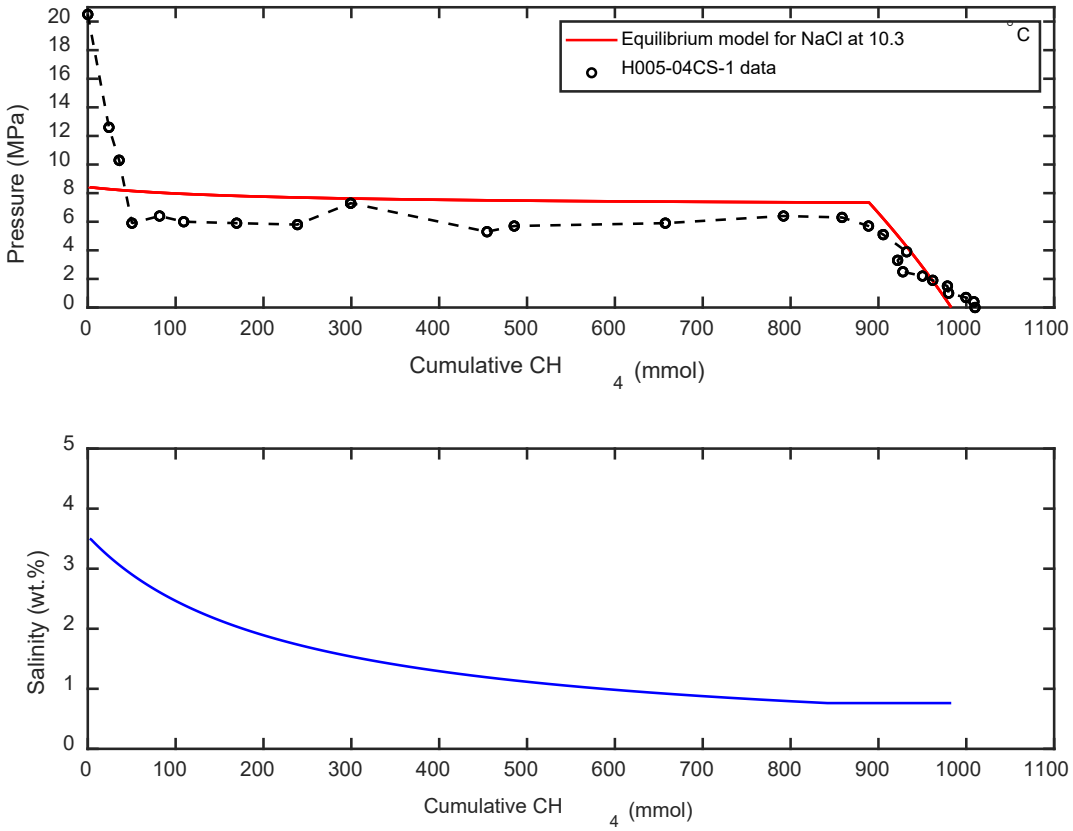

Figure C.1 Top: pressure versus cumulative methane for sample H002-04CS-1 compared to the pressure decline predicted for bulk equilibrium conditions. Bottom: Predicted salinity decline during hydrate dissociation.

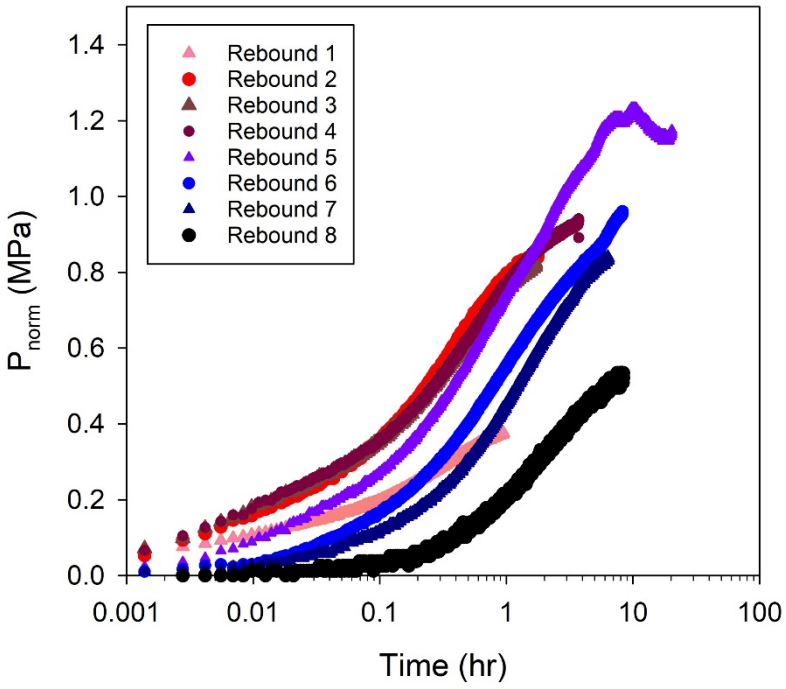

Figure C.2. Pressure rebounds during hydrate dissociation in sample H002-04CS-1.

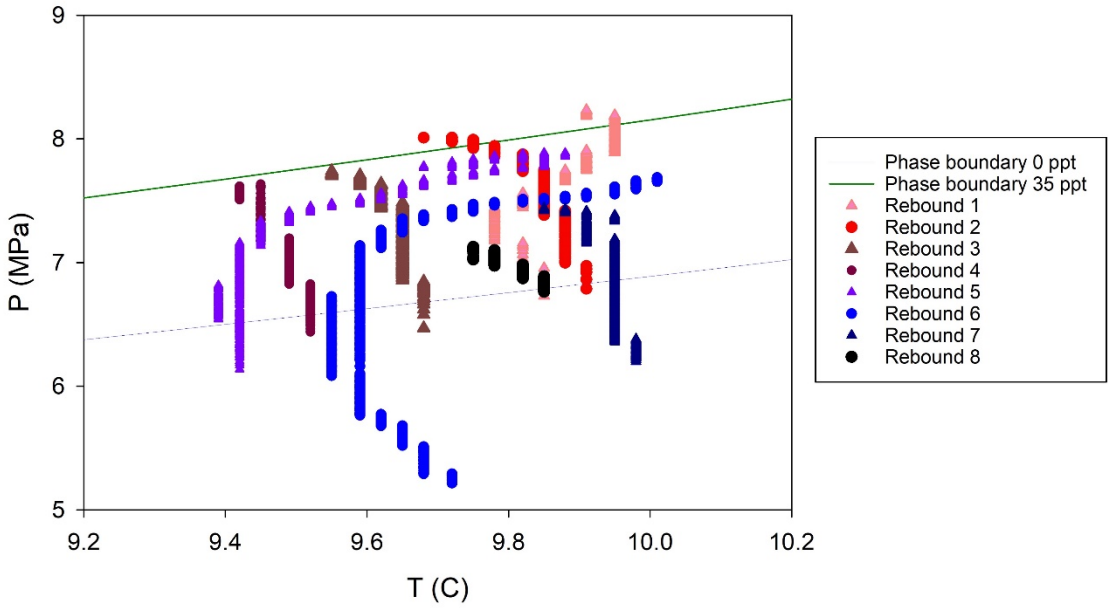

Figure C.3 Pressure rebounds plotted as pressure versus temperature for sample H005-04CS-1.

Appendix D

DOE Award No.: DE-FE-0028967

Revised Milestone Report

Milestone 2.D: Achieved gas production from GOM^2 samples monitored by micro-CT

SUMMARY

This milestone report summarizes our achievement of monitoring gas production from sediment samples that were observed with micro-computed X-ray tomography (micro-CT). The grains of UT-GOM2-1 GC 955 natural samples were too small to observe the pore space and monitor produced gas. Our available technology is insufficient to clearly distinguish hydrate and brine and observe hydrate pore habit in the largest grain size lithofacies (Sandy silt lithofacies, initially identified a lithofacies 2) recovered during UT-GOM2-1. With such small pore sizes (<1 μm), it would be extremely difficult to segment pore space and hydrate even by performing scans with high-resolution X-ray micro-tomography. For this reason, upon approval to make the change, we concentrated our micro-CT efforts for the remainder of the project on coarser sediments in which we can distinguish CH_4 hydrate clearly. We imaged pore habit of methane hydrate and analyzed its effect on relative permeability as planned in subtasks 8.1 and 8.2. The results show that hydrate preferentially dissociates at the boundaries of hydrate lumps. Inner hydrate may remain stable in large hydrate lumps. Over three days of dissociation in one example, we also observe new hydrate forming where hydrate was not present at day zero. This new hydrate is likely the result of the endothermic reaction during dissociation and the availability of relatively fresh water from dissociated hydrate. The fraction of interconnected pore space available to gas flow is notably small.

A. Introduction

The following sections summarize the results of hydrate formation and dissociation in sands with two characteristic grain sizes (mean diameters d_{coarse} = 700 μm and d_{medium} = 210 μm). The experiments are monitored through X-ray time-lapse tomography, and are a continuation of excess-gas experiments conducted during Phase 1.

B. Methods

The experimental procedure consists on the following:

(1) preparation of a dry sand pack;

(2) injection of methane gas to a target pressure (0.69 to 1.39 MPa, 100 to 200 psi, in our experiments);

(3) pressurization with KI brine under excess-water conditions (7 to 10 MPa in our experiments);

(4) cooling after pressurization to target temperature (2 to 5°C in our experiments);

(5) time-lapse X-ray tomography before and after the system enters the hydrate stability zone.

Such procedure results in a "water table" that pressurizes a "gas cap". Cycles of depressurization and pressurization help distribute methane in the sandpack to avert a clear water table. The brine used in these experiments was a solution of Potassium Iodine with a volumetric concentration of 4.4%. Brine was injected at a controlled pressure through a high-pressure syringe pump.

The experiments were monitored with a Nikon micro-tomograph model XTH 225. The pressure vessel and temperature control have been already described in previous milestone reports.

C. Results

Hydrate formation in sandpack with bimodal pore size distribution under excess-water condition

Figure D.1 shows an example of sand pack with bimodal distribution. The objective of this kind of experiments was to observe directly the implications of having two different types of pore sizes on hydrate formation, pore habit, and dissociation. The results show that hydrate forms preferentially at gas-brine interfaces. The gas phase "disappears" as gas is consumed and forms hydrate. Eventually, gas hydrate remains as nodules filling up the pore bodies of the sand pack. We do not observe consistent "grain-coating" or "grain attaching" hydrate, even at low hydrate saturations.

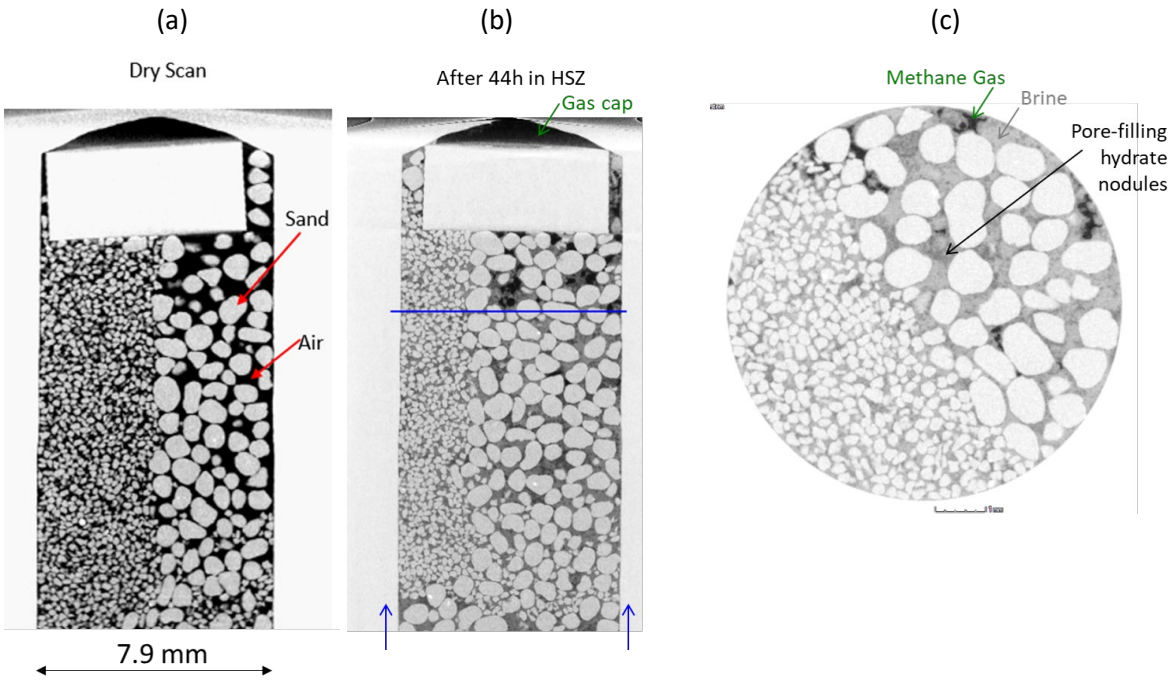

Figure D.1. *Example of hydrate formation under excess-water condition. (a) Dry scan of sandpack with bimodal grain size distribution. (b) Scan after 44 hours within the hydrate stability zone. Water is injected from the bottom and forms a gas cap on the top of the vessel. (c) Radial slice showing simultaneous presence of gas, brine, and CH_4 hydrate.*

Gas production monitored by micro-CT

Figure D.2 shows an example of methane hydrate dissociation in sand. Initially, CH_4 hydrate is stable and exhibits a pore-filling or pore-interconnected habit. Hydrate is porous with pores mostly filled by CH_4 gas. A few pores within hydrate and adjacent pore space is filled with high salinity brine. The increase of salinity in brine over the period of hydrate growth is due to ion exclusion during hydrate formation. Figure D.2 (left) shows the state after 1 day into slow dissociation but this image is very similar to the initial condition .

The experiment follows a slow depressurization pressure-temperature path from 8.2 MPa and 6.8°C gradually to 4.3 MPa and 6.2°C over five days of dissociation. Figure D.2 shows examples of images captured during the dissociation process after 1 and 3 days into the dissociation process.

- The dissociation of the section with low hydrate saturation is straightforward (Figure D.2 bottom). Hydrate dissociates quickly leaving water at grain contacts and releasing gas into the pore space. The relative gas permeability is expected to be relatively high because original gas saturation is high.
- The case with initial hydrate saturation over 50% exhibits a different and more complex behavior during dissociation. Hydrate preferentially dissociates at the boundaries of hydrate lumps. Inner hydrate may remain stable in large hydrate lumps. Over 3 days of dissociation, we also observe new hydrate formed where it was not present at day zero. This new hydrate is likely the result of the endothermic reaction during dissociation and the availability of relatively fresh water from dissociated hydrate. The fraction of interconnected pore space available to gas flow is notably small.

The observation of hydrate dissociation in sections with initial high hydrate saturation suggests that gas relative permeability is expected to be significantly low at initial stages of dissociation in hydrate systems fully saturated by brine. The reason is lack of gas phase connectivity. Furthermore, hydrate re-formation due endothermic effects and presence of fresh water further blocks pores with methane gas.

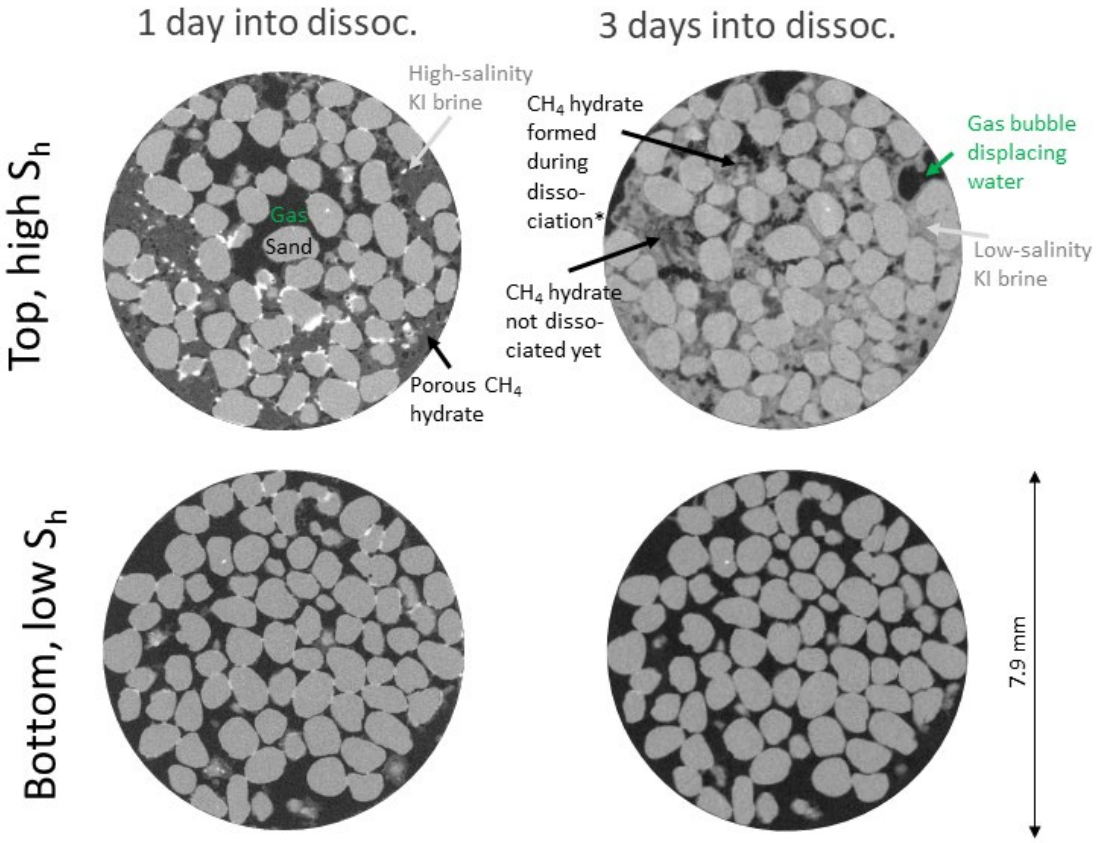

Figure D.2. *Radial slices of micro-consolidation vessel filled with sand during hydrate dissociation under excess gas conditions. The images show that radically different scenarios occur depending on initial hydrate saturation. High initial hydrate saturation leads to complex water-gas-hydrate interactions.*

D. References

None

Appendix E

DOE Award No.: DE-FE-0028967

Milestone Report

Milestone 2.E: Building a chamber to prepare natural samples for 2D-3D micro-Raman analysis

SUMMARY

This milestone report summarizes our achievement of Building a chamber to prepare natural samples for 2D-3D micro-Raman analysis. This Milestone report is specific to Tasks 9 *Micro-Scale: Raman Observation on hydrate-bearing sand packs*. The following sections summarize the chamber design, data acquisition system, and testing of the device. The PI in charge of this task is Jung-fu Lin. Lab Director Peter Polito, and Research Engineer Joshua O'Connell executed high-pressure chamber design, construction, and testing.

A. Introduction

Two systems were envisioned for the Micro-Raman observation of hydrate behavior in natural sediment. One was designed to observe hydrate formation and depressurization with flow in natural UT-GOM2-1 sediment from GC 955. The other was designed to observe the state of naturally formed intact hydrate and depressurization of intact hydrate-bearing sediment from GC 955.

B. Methods

B.1 Flow through cell for natural sediment

A Micro-Raman Flow-Through Chamber for Pore-Scale Methane Hydrate Dissociation and Gas Diffusion was developed. The chamber was intended to observe hydrate formation and depressurization with flow using natural depressurized sediments from Gulf of Mexico as the porous medium. The chamber included a long sapphire fused window.

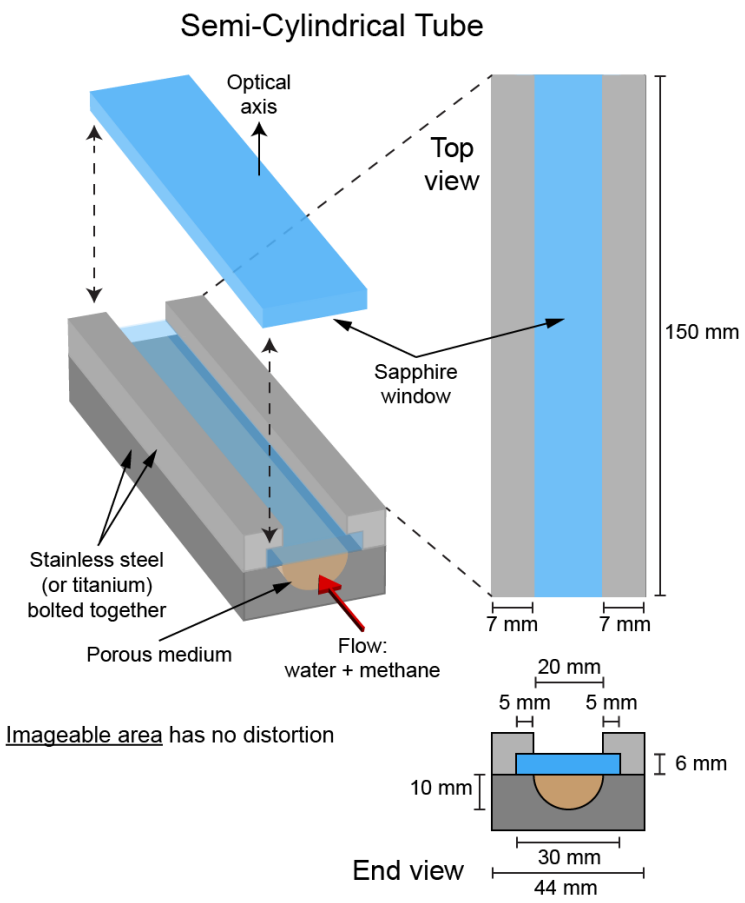

Figure E.1 Conceptual design of a flow through cell for Raman observation of hydrate behavior with flow.

B.2 Micro-Raman cell for intact hydrate natural sediment

Text (might have to acknowledge Geotek's contribution here)

C. Results

The micro-Raman flow-through cell design was sent to Rayotek Scientific Inc. for revision and manufacturing. Rayotek and UT iterated the design back and forth until both parties agreed on the feasibility. Rayotek was able to manufacture the custom sapphire window but was unable to maintain pressure during the testing phase. Each design iteration resulted in premature fracture of the sapphire window. The cell design and manufacturing were ultimately abandoned due to these manufacturing challenges.

The Micro-Raman cell for observation of intact samples (Figure E.3, left) was successfully manufactured by M&H Machining (pressure vessel) and Rayotek Scientific Inc. (sapphire viewing window). The chamber was shipped to the UT Pressure Core Center, and tested. Once tested, a compromised sample

from UT-GOM2-1 expedition was loaded into UT's Mini-PCATS and cut. The storage chamber was then removed, the Micro-Raman chamber attached, and the cut sample pushed into the chamber. Figure E.3 (right) shows a photo of the chamber with the pressurized sample inside as seen through the sapphire window. The Photo was taken before the fine sediment in the PCATS confining water had settled, having been stirred up by the movement of the sample from mini-PCATS into the chamber. Experiments will be conducted with the Horiba Raman fiber probe (Figure E.4) through the sapphire window in the future.

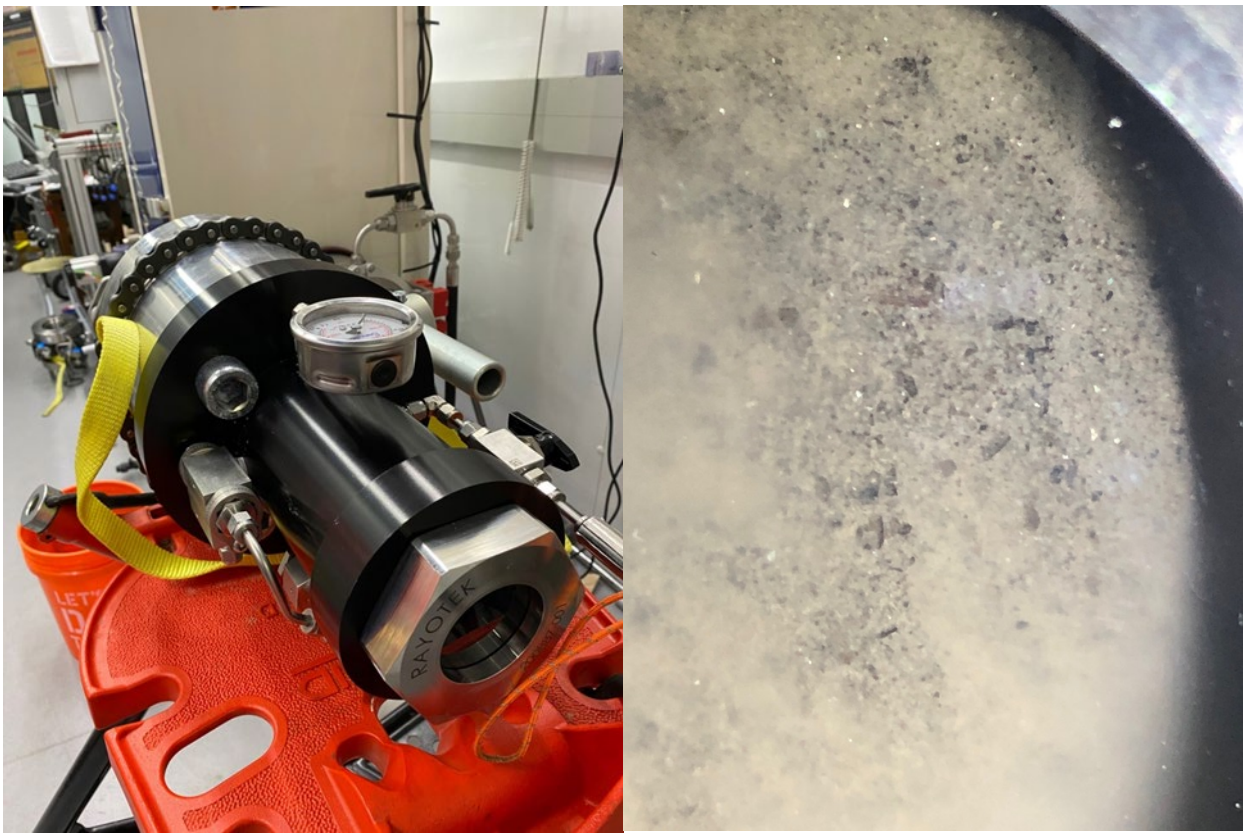

Figure E.3. Left micro-Raman core chamber for natural intact hydrate samples. Right photo of UT-GOM2-1 GC 955 material through the core chamber sapphire window where fine grain material is still unsettled.

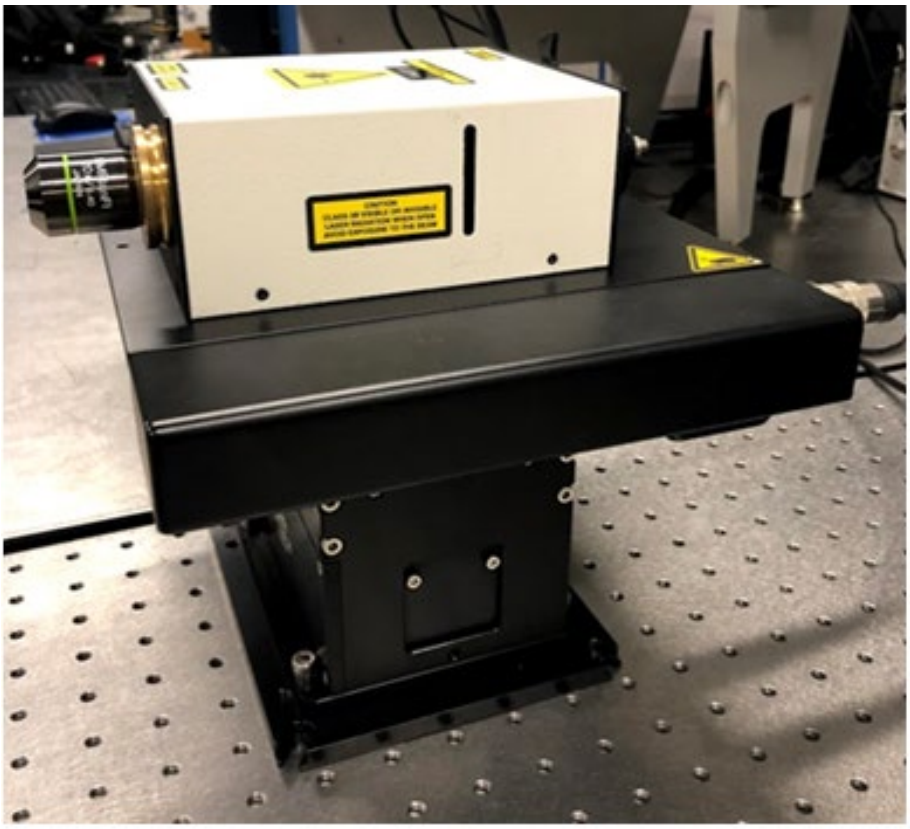

Figure E.4. Horiba Raman fiber probe on a stage for remote measurement

D. Acknowledgements

This work was partially funded by ExxonMobil.

Appendix F

DOE Award No.: DE-FE-0028967

Milestone Progress Report

Milestone 2.F: 2D micro-Raman analysis of natural methane hydrate samples at depressurization

SUMMARY

This milestone report summarizes our progress of analyzing sand and natural methane hydrate samples using 2D micro-Raman during depressurization. This Milestone report is specific to Tasks 9. We have successfully observed hydrate reformation and dissociation in GC 955 sediment where the naturally formed hydrate has been previously dissociated. The P.I. in charge of this task is Jung-fu Lin.

A. Introduction

B. Methods

Two kinds of sediments were loaded in our Raman chamber at the same time: natural GC 955 sandy silt and clay-free quartz laboratory sand. The sandy silt (previously identified as Lithofacies 2) sample was from dissociated core GC955-H005-06FB-2 at a depth of 429.46 - 429.56 meter below sea floor. The laboratory quartz sand is substantially coarser than sandy silt, with diameters ranging from 210 -297 μm. We first loaded dry sediments in the chamber using a filter paper to separate two kinds of sediment and limit clay migrations from GC 955 Sandy silt to sand (Figure F.1). The filter paper was then removed. We then loaded vapor methane followed by 3.5 wt% NaCl aqueous solution to bring the system up to pressure. The temperature was lowered into the hydrate stability zone to synthesize methane hydrate and CH_4 hydrates formed at ~ 15.5 MPa and 280 K. Dissociation was later induced by controlled depressurization at constant temperature.

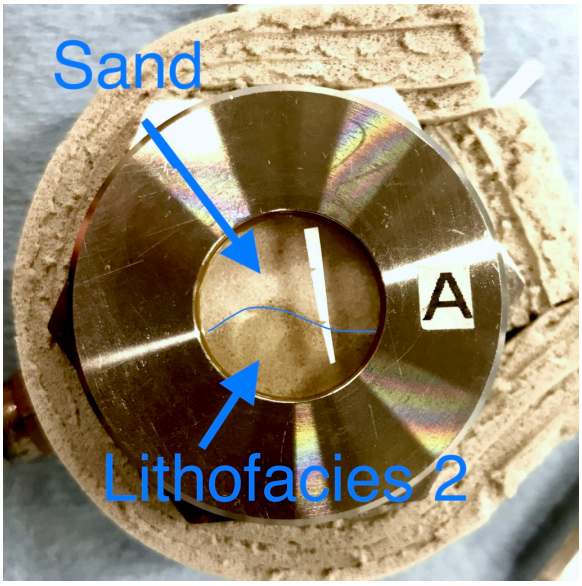

Figure F.1 *Photo of 2 kinds of dry sediments loaded in the Raman chamber prior to hydrate formation: natural sandy silt from core GC955-H005-06FB-2 (Lithofacies 2) and quartz sand. The mass medium diameter of sandy silt is 40 µm). The sand diameter ranged from 210-297 µm*.

Observations of hydrate formation were made in in GC 955 sandy silt sediment and laboratory quartz sand. As hydrate forms we see optically the disappearance of CH_4 vapor (Figure F.2 a to b), accompanied by ~ 1 MPa drop in pressure, and the appearance of the hydrate large and small cage peaks at Raman shifts of 2902 and 2912 cm^{-1}. Representative Raman spectra of the sI hydrate in the sand (blue) and the GC 955 sediment with a strong fluorescent background from the clay minerals (red) are shown in Figure F.3.

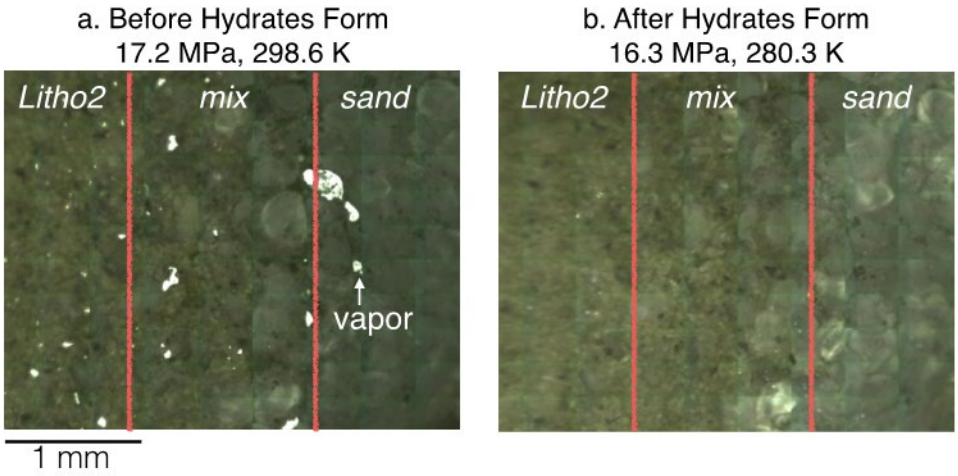

Figure F.2 Optical images of the sample chamber before (a) and after (b) hydrate formation. The obvious signature of hydrate formation is the disappearance of vapor phase. The red vertical lines divide the

sample chamber into three parts: Sandy silt (Lithofacies 2) in the left; a mixture of sandy silt and sand in the middle and sand in the right.

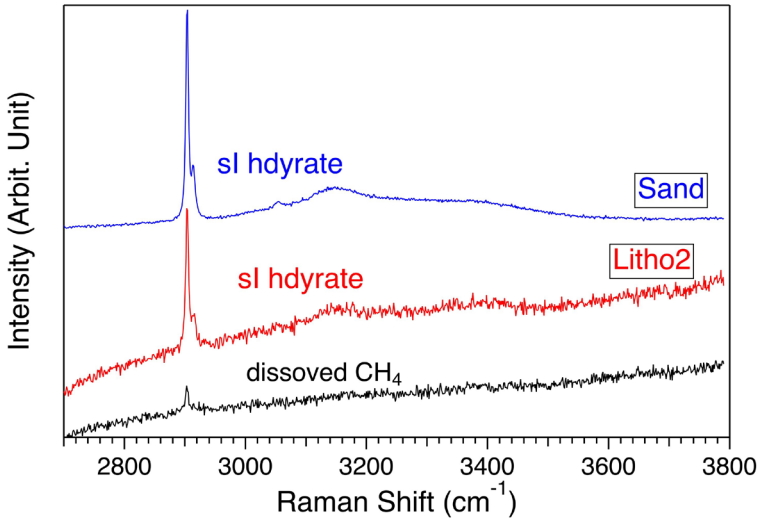

Figure F.3 Representative Raman spectra of structure I (sI) methane hydrate in natural GC 955 sandy silt (Litho 2) and Quartz sand. The sandy silt is shown in red, quartz sand sample is shown in blue, and the dissolved methane vapor spectra in black. The strong fluorescence from clay minerals make the background of the red spectrum tilted.

C. Results

2D mapping was conducted during depressurization of the methane hydrate formed in the layered system of GC 955 sediment and quartz sand, the Raman intensity of methane hydrate decreased as an indication of hydrate dissociation (Figure 57 comparing top row, 10.5 hours, and middle row, 32.2 hours) and methane vapor appeared in the sand (Figure 58).

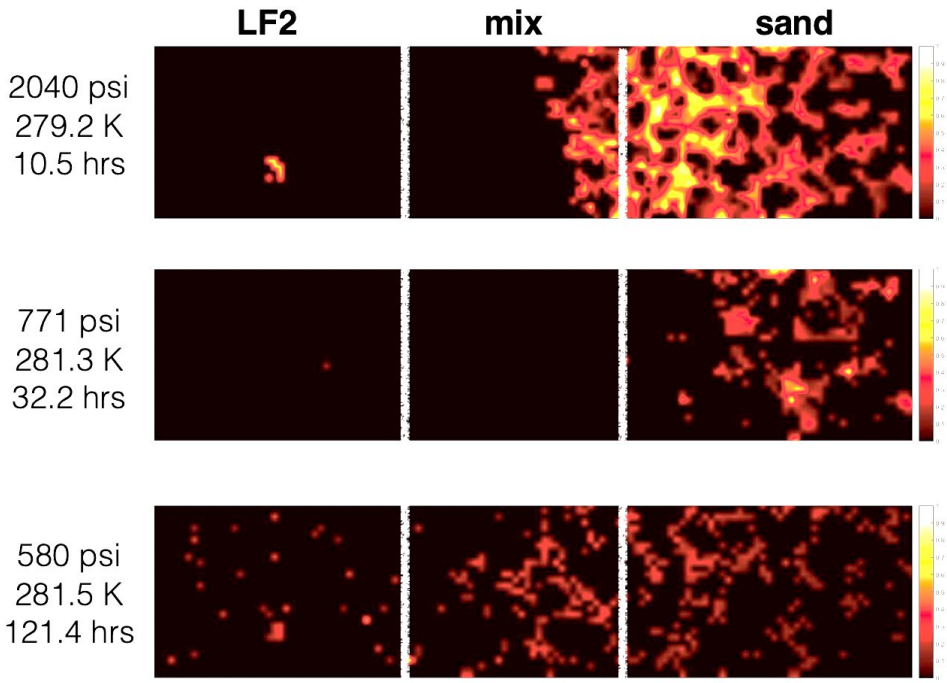

Figure F.4 Methane hydrate Raman 2D mapping during methane hydrate dissociation in experiment RH010. The mapping was conducted near the boundary of the GC 955 sandy silt (Litho 2, LF2) and laboratory quartz sand. Materials and fluids can flow freely across the GC 955 sediment, the mixture (mix), and sand layers. Higher intensity (yellow-white color) indicates higher methane hydrate concentration in pore spaces.

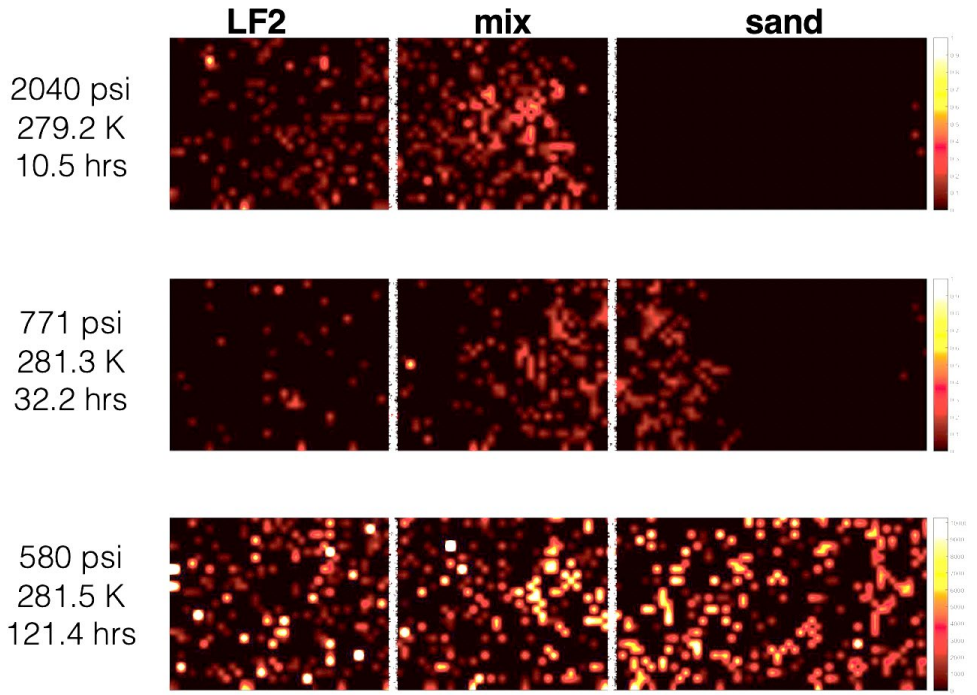

Figure F.5. Methane vapor Raman 2D mapping during methane hydrate dissociation in experiment RH010. The mapping was acquired at the same position as Figure 56. Higher intensity (yellow-white color) indicates higher methane vapor presence in the pore spaces.

National Energy Technology Laboratory

626 Cochrans Mill Road
P.O. Box 10940
Pittsburgh, PA 15236-0940

3610 Collins Ferry Road
P.O. Box 880
Morgantown, WV 26507-0880

1011 Highway 6 S. Suite 309
Houston, TX 77077

1450 Queen Avenue SW
Albany, OR 97321-2198

Arctic Energy Office
420 L Street, Suite 305
Anchorage, AK 99501

Visit the NETL website at:
www.netl.doe.gov

Customer Service Line:
1-800-553-7681

NATIONAL ENERGY TECHNOLOGY LABORATORY

U.S. DEPARTMENT OF ENERGY | NATIONAL ENERGY TECHNOLOGY LABORATORY